SR BEHAVIOUR DURING HYDROTHERMAL ALTERATION OF OCEANIC GABBROS EXPOSED AT HESS DEEP – IMPLICATIONS FOR $^{87}SR/^{86}SR$ COMPOSITIONS AS A PROXY FOR FLUID-ROCK INTERACTION

by

Timo Kirchner
B.Sc., Albert-Ludwigs-Universität Freiburg, 2008

A Thesis Submitted in Partial Fulfillment
of the Requirements for the Degree of

Master of Science

in the School of Earth and Ocean Sciences

Supervisory Committee

SR BEHAVIOUR DURING HYDROTHERMAL ALTERATION OF OCEANIC GABBROS EXPOSED AT HESS DEEP – IMPLICATIONS FOR $^{87}SR/^{86}SR$ COMPOSITIONS AS A PROXY FOR FLUID-ROCK INTERACTION

by

Timo Kirchner
B.Sc., Albert-Ludwigs Universität Freiburg, 2008

Supervisory Committee

Dr. Kathryn Gillis (School of Earth and Ocean Sciences)
Supervisor

Dr. Laurence Coogan (School of Earth and Ocean Sciences)
Committee Member

Dr. Dante Canil (School of Earth and Ocean Sciences)
Committee Member

Supervisory Committee

Dr. Kathryn Gillis (School of Earth and Ocean Sciences)
Supervisor

Dr. Laurence Coogan (School of Earth and Ocean Sciences)
Committee Member

Dr. Dante Canil (School of Earth and Ocean Sciences)
Committee Member

ABSTRACT

Mid-ocean ridge hydrothermal systems are known to extend to deep levels of the oceanic crust, including the plutonic section, but little is known about the timing and nature of fluid-rock interactions at these levels. To investigate the temporal and spatial characteristics of hydrothermal alteration in the lower crust, this study investigates a suite of hydrothermally altered (<5 to >20% hydrous alteration) gabbroic rocks recovered from the Hess Deep Rift, where 1.2 Ma fast-spreading East Pacific Rise crust is well-exposed. These samples were altered to amphibole-dominated assemblages with chlorite-rich samples occurring in a restricted region of the field area. Hornfels, indicative of reheated, previously altered rocks, are clustered in the central part of the field area. The entire sample suite has elevated $^{87}Sr/^{86}Sr$ (mean: 0.70257±0.00007 (2σ), n=16) with respect to fresh rock (0.7024). Bulk rock $^{87}Sr/^{86}Sr$ is strongly correlated with percentage of hydrous alteration and weakly correlated with bulk rock Sr content. The distribution of Sr in igneous and metamorphic minerals suggests that greenshist-facies alteration assemblages (chlorite, actinolitic amphibole, albitic plagioclase) lose Sr to the fluid while amphibolite-facies secondary assemblages (secondary hornblende, anorthitic plagioclase) take up Sr.

The temperature-dependent mobilization of Sr in hydrothermal systems has implications for the $^{87}Sr/^{86}Sr$ and ultimately fluid/rock ratio calculations based on the assessed $^{87}Sr/^{86}Sr$ systematics. Considering Sr behaviour, minimum fluid/rock ratios of ~1 were calculated for the plutonic section. Due to the large uncertainty regarding fluid Sr composition at depth and the sensitivity of fluid/rock ratio calculations on this parameter, a model combining the sheeted dike complex and the plutonic section to one hydrothermal system is introduced, yielding a fluid/rock ratio of 0.5. This value may be more realistic since the fluid composition entering and exiting the sheeted dike complex is better constrained.

The regional distribution of hornfelsed material with elevated $^{87}Sr/^{86}Sr$ suggests that fluid ingress into the upper plutonics at Hess Deep occurred on-axis in a dynamic interface of a vertically migrating axial magma chamber (AMC) and the base of the hydrothermal system.

Table of Contents

List of Tables

List of Figures

Acknowledgements

I would like to thank Kathy Gillis for giving me this research opportunity and her guidance and help throughout my Master's degree. I would also like to thank Laurence Coogan for ideas regarding geochemical modelling and Jody Spence for his help with analytical procedures and data reduction. I appreciate the uncomplicated cooperation with researchers from UBC and thank Mati Raudsepp, Edith Czech and Greg Dipple for letting me use their analytical instruments. Lastly, I am very grateful for the support I received from my family and friends in Germany and Canada.

Chapter 1

INTRODUCTION

At mid-ocean ridges (MORs), cold seawater penetrates young, permeable oceanic crust to become part of a thermally-driven hydrothermal system that controls elemental fluxes between the earth's interior and the oceans, and the cooling of the lithosphere. The discrepancy between measured and modelled conductive heat flow in young oceanic lithosphere suggests that almost 30% of the global oceanic heat flux is accommodated by hydrothermal circulation. Additionally, an estimated ~30% of lithospheric heat removed by convection occurs on-axis within ~1 Ma (Stein and Stein, 1992). Spatially, MORs represent only ~2% of the area affected by convective heat transfer, highlighting the importance of axial hydrothermal systems in the heat budget of the oceanic lithosphere. These systems are dependent on the presence and geometry of a heat supplying source and the structure of the overlying crust.

Our understanding of chemical exchange between the oceans and oceanic lithosphere, and its implications for the broader earth system is still in the early stages. For example, hydrothermal vent fields are known to be the habitat for a variety of organisms that are adapted to the extreme conditions on the seafloor. These chemotropic organisms feed from the metal-laden fluids exiting the vents (e.g., Tunnicliffe, 1991). Another implication of high-temperature hydrothermal systems that will likely grow in importance over the coming decades is the economic potential found in hydrothermal systems. Metals such as Zn, Cu and Mn can be highly mobile under certain hydrothermal

conditions leading to leaching of these elements from the crust followed by precipitation as sulphides in shallower levels of the hydrothermal system (Seyfried and Janecky, 1985). In some hydrothermal systems, precipitation of ores is abundant enough to produce volcanogenic massive sulphide deposits (VMS), making mid-ocean ridge hydrothermal systems a field of interest for the mining industry (e.g., Rona, 1988).

Due to the magma-starved nature of slow-spreading ridges, the lithologic sequences at these settings may not have a simple layered stratigraphy and extrusive lithologies can be highly variable in thickness or are missing completely (e.g., Dick, 1989). At slow-spreading ridges, magma chambers are likely intermittent features that occur at variable depths below the seafloor (e.g., Toomey et al., 1988). In contrast, a well-defined lithologic sequence is found at intermediate- to fast-spreading ridges and includes a volcanic section, sheeted dike complex and a plutonic section with increasing depth (e.g., Karson et al., 2002). In these settings, a relatively continuous, thin melt lens has been detected seismically at a depth of <1 to 2 km below the seafloor (e.g., Detrick et al., 1987; Hooft et al., 1997). Even though it was found that average depth and depth variability of magma chambers decreases with increasing spreading rate (e.g., Purdy et al., 1992), depth variation of ~400 m can occur within 2 km along axis at fast-spreading ridges (Babcock et al., 1998).

Hydrothermal systems are thermally driven and thus, the temporal and spatial characteristics of the heat source will be directly linked to the nature of on-axis fluid flow. Heat source properties are markedly different between fast- and slow-spreading

ridges. Since the heat source at slow-spreading ridges is commonly deeper-seated, the hydrothermal system will likely also extent to greater depths, increasing the length of the fluid-rock reaction path. This in turn leads to increasingly rock-dominated fluid chemistry at the end of the path at slow- versus fast-spreading ridges (Bach and Humphris, 1999).

Due to the restricted accessibility of the lower oceanic crust, especially at intermediate- and fast-spreading ridges, important findings with respect to igneous and hydrothermal systems in these settings have been inferred from ophiolites, which are the best on-land equivalents to mid-ocean ridges (e.g., Nicolas et al., 1988; Quick and Denlinger, 1993; Kelemen et al., 1997; Bickle and Teagle, 1992). However, more and more evidence suggests that some, if not most ophiolites in supra-subduction zones rather than at MORs (e.g., Miyashiro, 1973). A different geochemical signature in igneous rocks from ophiolites (Miyashiro, 1973), along with the observation that the Sr isotopic ratio of seawater is variable over time (Hess et al., 1986), fluid-rock interaction and the use of $^{87}Sr/^{86}Sr$ as a geochemical proxy may have different implications for hydrothermally altered rocks from modern MORs versus ophiolites. Improvement of drilling technology and seismic techniques as well as more comprehensive exploration of the ocean floor in recent years has allowed for more detailed in-situ investigations on mid- and lower-levels of fast-spread crust (e.g., Hess Deep, Pito Deep, Hole 504B), making the study of these lithologies less dependent on observations from ophiolites.

1.1 Background on magmatic and hydrothermal processes at mid-ocean ridges

1.1.1 Magmatic accretion models

Hydrothermal circulation at the ridge axis controls the removal of lithospheric heat so that the location and depth of fluid penetration into the plutonic section are directly related to the accretion of the lower oceanic crust. To date, for intermediate- to fast-spreading ridges, two end-member models predict the style of accretion of the lower oceanic crust. First, in a model referred to as the gabbro glacier model, all crystallization occurs in a small, shallow magma lens followed by crystals subsiding in a mush zone that extends to the base of the crust (e.g., Nicolas et al., 1988; Quick and Denlinger, 1993) (Figure 1.1a). In this scenario, the base of the hydrothermal system is expected to be located near the base of the sheeted dike complex with the latent heat of crystallization being removed by hydrothermal fluids at relatively shallow levels. Second, the sheeted sill model proposes that crystallization of gabbroic rocks occurs in multiple sills located at different depths between the Moho and the base of the sheeted dike complex (e.g., Kelemen et al., 1997) (Figure 1.1b). This model requires the penetration of hydrothermal fluids to considerable depths close to the ridge axis in order to remove the latent heat of crystallization. Thus, in order to better understand the accretion of the lower oceanic crust, it is crucial to understand the geometry and timing of hydrothermal fluid penetration, as well as the associated fluid and heat fluxes.

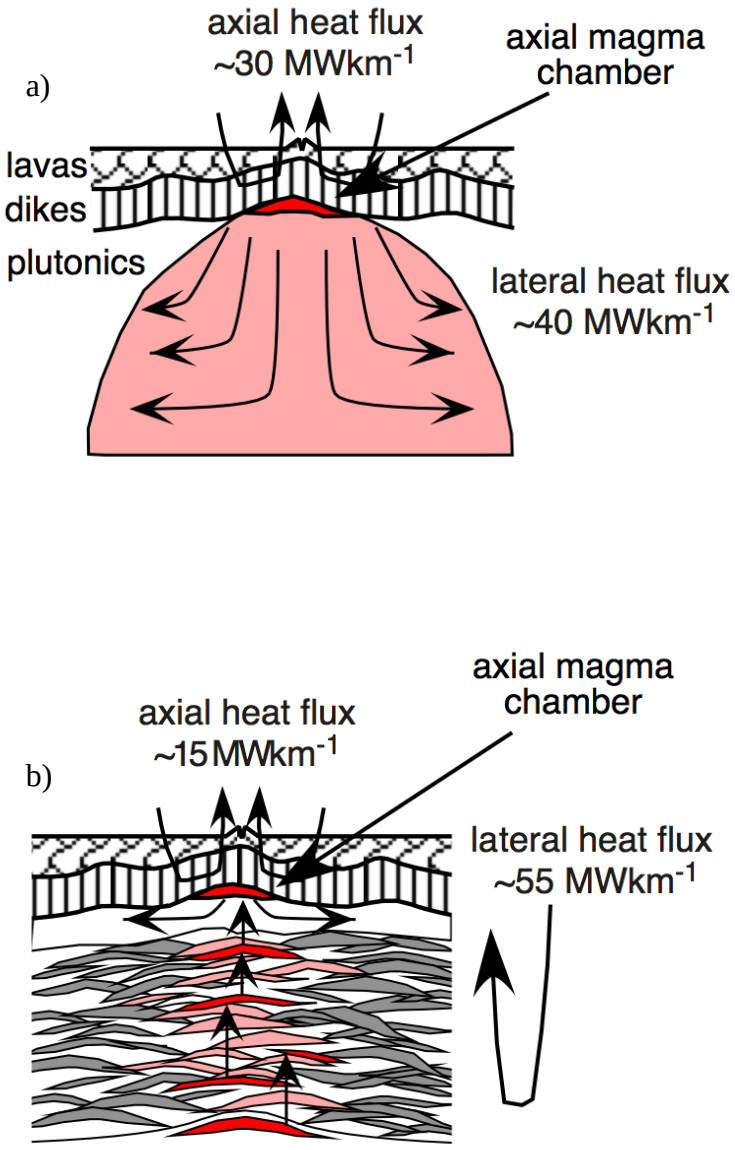

Figure 1.1: End-member models predicting the accretion of the lower oceanic crust at intermediate- to fast-spreading ridges. a) The *gabbro glacier model* (e.g., Quick and Denlinger, 1993) with hydrothermal cooling from the top; b) The *sheeted sill model* (e.g., Kelemen et al., 1997), requiring deeper penetration of hydrothermal fluids along the margin of the crystal mush zone. Figures from Coogan (2007).

1.2 Axial hydrothermal systems

Since the discovery of a high-temperature submarine hydrothermal vent field in 1977, mid-ocean ridge hydrothermal systems have been a constantly growing subject of study. To date, the number of combined confirmed and inferred vent fields at mid-ocean ridges exceeds 550. They are found at MORs at all spreading rates exiting the seafloor at temperatures ranging from ~60 to ~460ºC (http://www.interridge.org/irvents).

While the nature of certain geochemical modifications of fluid and crust is relatively well constrained, the location and timing of these reactions is not well understood. Spatial characteristics of the hydrothermal convection cell have been investigated in various field, theoretical and experimental studies leading to the development of contrasting models for hydrothermal systems (e.g., Alt, 1995; Coogan, 2008; Gillis, 1995; Mottl, 1983; Seewald and Seyfried, 1990). Most of these models subdivide the hydrothermal system into a recharge zone, the base of the hydrothermal system ("reaction zone"), and a discharge zone. However, models differ with respect to timing and nature of reactions occurring as the fluid passes the different zones. In a conventional model (e.g., Alt, 1995; Mottl, 1983), seawater enters the permeable volcanic section, circulating along 3-dimensional pathways and undergoes minimal low-temperature reactions (Figure 1.2a). Modified seawater then enters the sheeted dike complex within a recharge zone, where fluid conduits are inferred to be more 2-dimensional and the fluid is heated up dramatically. The fluid loses its seawater character increasingly during this stage by reacting with the rocks through which it is passing. At the base of the hydrothermal system, which is commonly inferred to be the base of the sheeted dike complex, fluids

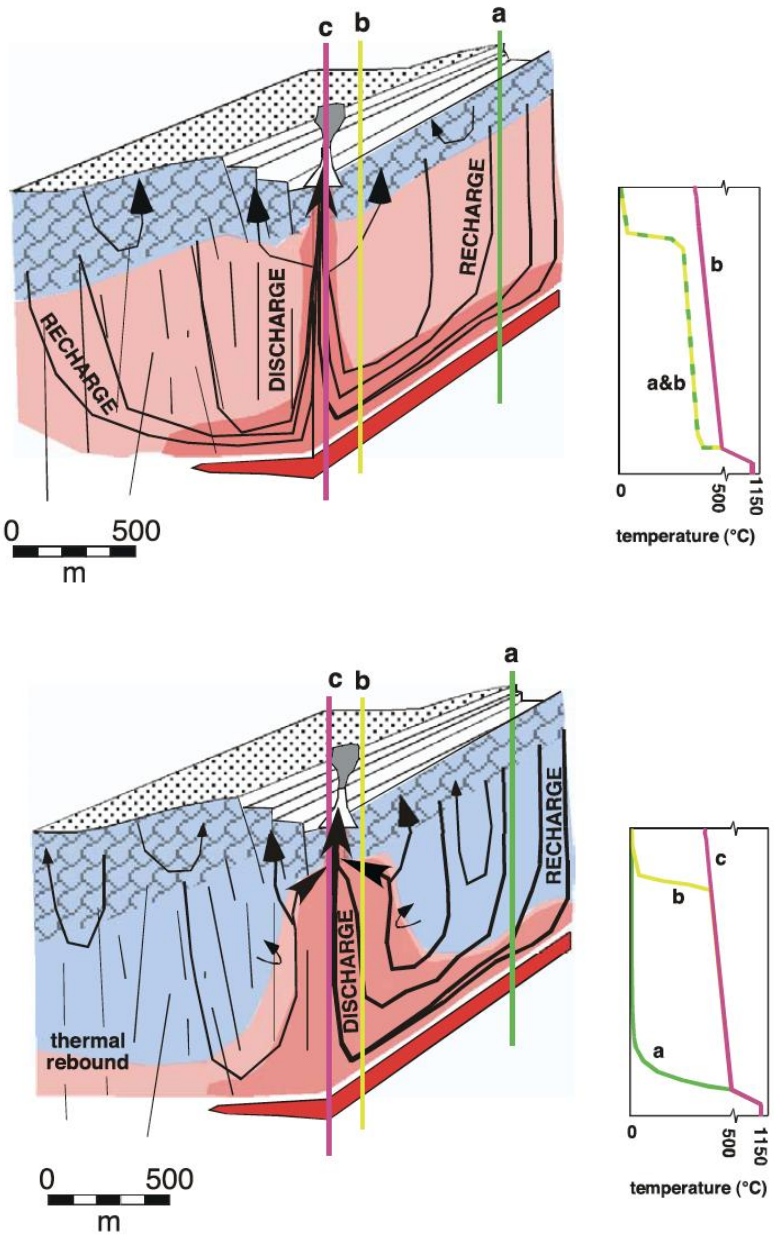

Figure 1.2: Hydrothermal models predicting the geometry and reaction paths of on-axis hydrothermal circulation at intermediate- to fast-spreading ridges. a) A conventional model (e.g., Alt, 1995) assumes fluids are heated during recharge and rise adiabatically during discharge. b) An alternative model (e.g., Coogan, 2008) predicts a cool recharge zone with enhanced water-rock reactions occurring in the lower third of the sheeted dike complex and in a hot and relatively broad discharge zone. Thermal profiles in each model illustrate temperature distributions in different parts of the hydrothermal system. Figures from Coogan (2008).

enter a reaction zone where maximum temperatures cause extensive fluid-rock alteration. Lastly, high-temperature fluids undergo rapid and near-adiabatic upwelling through focused discharge zones with little or no change in chemistry. Thus, in this model, crustal alteration patterns and vent fluid chemistry are largely fixed in the recharge zone and at the base of the hydrothermal system, respectively.

High temperatures in the upper sheeted dike complex, as well as a sharp temperature increase at the volcanic-dike transition are recorded in hydrothermally altered, extrusive rocks (<50 to >180ºC) (Gillis, 1995). This was found to be inconsistent with conventional reaction path models assuming significant heating of fluids during recharge, as the upper crust is cooled too efficiently in recharge zones to allow for such high temperatures in the shallow sheeted dike complex (e.g., Sleep, 1991; Coogan, 2008). Based on these findings, as well as geochemical and mineralogical characteristics within sheeted dike complexes, an alternative model was proposed suggesting that recharge is relatively cool and significant heating does not occur until the fluid enters the lower sheeted dike complex, and most of the high-temperature fluid-rock alteration occurs within discharge zones, that are much broader than previously assumed (Coogan, 2008) (Figure 1.2b).

The deepest level of fluid penetration in both models is generally assumed to be at the base of the sheeted dike complex, underlain by a thermal boundary layer that separates a magma chamber from the overlying hydrothermal system. However, temporal fluctuations in the depth of axial magma chambers were predicted by seismic studies and geologic relationships suggesting that the base of the hydrothermal system may extend to

deeper levels into the gabbroic section at the ridge axis (Babcock et al., 1998; Gillis, 2008; Coogan et al., 2003).

As axial magma chambers cool and plutonic rocks solidify further off-axis, the hydrothermal system could expand to greater depths beyond the outer margins of the melt lens as soon as the rocks are brittle enough to allow for microcracking (e.g., Wilcock and Delaney, 1996). Secondary mineral assemblages found at the Hess Deep Rift and ophiolites show that fluids penetrate relatively deep into the lower oceanic crust, although the timing is not well constrained (e.g., Manning et al., 2000; Coogan et al., 2002c). The earliest mineralogical evidence of this hydrothermal flow is amphibole-filled microfractures, which record temperatures of 690-750ºC (e.g., Manning et al., 1996; Coogan et al., 2007), consistent with the estimated brittle-ductile transition of 700-800ºC at mid-ocean ridges (e.g., Phipps Morgan and Chen, 1993). At these temperatures, the hydrothermal fluid is in a supercritical state and shows physical properties that are drastically different to seawater (Bischoff and Rosenbauer, 1985). For example, viscosity is strongly decreased, allowing the fluid to penetrate rocks with lower permeability. Furthermore, heat capacity under these conditions is strongly increased suggesting that heat removal is highly efficient at the base of the hydrothermal system. Therefore, if high-temperature influx of a hydrothermal fluid occurs lateral to the melt lens, then the slope of the brittle-ductile transition controls the depth to which the fluid is able to penetrate. A steep slope would allow for relatively deep water influx close to the ridge axis, whereas a gentle slope would inhibit fluid flow deep into lower crustal levels until

the rocks are further off-axis (e.g., Coogan et al., 2002b; Cherkaoui et al., 2003; Phipps Morgan and Chen, 1993).

Comparison of vent fluid and seawater chemistry contributed significantly to the understanding of water-rock reactions occurring in the oceanic crust and general elemental fluxes were found to be consistent with the primary and secondary mineralogy of altered basaltic and gabbroic rocks. The following geochemical trends were observed: alkalis (other than Na), Ca, and silica are variably enriched in vent fluids with respect to seawater. Na and Sr contents are linearly correlated to the Cl content of the fluid and are likely buffered by reactions involving plagioclase (e.g., Von Damm, 1990; Berndt et al., 1988). These species may be variably enriched or depleted in vent fluids with respect to seawater. Extreme Cl depletion or enrichment in vent fluids is likely caused by phase separation of the fluid at depth (e.g., Palmer, 1992). Transition metals like Fe, Mn, Cu and Zn are significantly enriched in vent fluids with respect to seawater. These metals are inferred to be leached under high temperatures ($\geq$400ºC) and reducing conditions (Seewald and Seyfried, 1990). Mg and sulphate, in contrast, are removed from seawater quantitatively under relatively low to intermediate temperatures mostly due to the precipitation of clay minerals, chlorite and anhydrite. Furthermore, vent fluids are reduced and much more acidic than seawater (e.g., Von Damm, 1990).

1.3 Using Sr isotopic ratios as a tracer for fluid-rock interaction.

Different geochemical tracers have been used as proxies for fluid-rock interaction at mid-ocean ridges. Among these tracers, $^{87}Sr/^{86}Sr$ has been found to be effective due to the distinctive $^{87}Sr/^{86}Sr$ of fresh rock and seawater. The Sr isotopic composition of seawater over time is relatively well constrained (e.g., Burke et al., 1982) and if the $^{87}Sr/^{86}Sr$ of the fresh rock in question is known, the $^{87}Sr/^{86}Sr$ of altered rock can be used to quantify the amount of water that reacted with the oceanic crust (e.g., Albarède, 1981; Bickle and Teagle, 1992; Gillis et al., 2005; Barker et al., 2008). A challenge in using Sr to trace fluid/rock interaction is that the behaviour of Sr in hydrothermal systems is not well known and likely is not constant under changing conditions within the hydrothermal system.

Fluid fluxes at fast-spreading ridges have been calculated for the sheeted dike complexes from the Hess Deep Rift, Pito Deep and ODP Hole 504B using a linear-kinetic approach to model Sr isotopic transport (Gillis et al., 2005; Barker et al., 2008; Teagle et al., 2003). Minimum time-integrated fluid fluxes at the three locations were calculated to range from 1.5-2.6 x 10^6 kg/m^2, suggesting that fluid flow in modern intermediate- to fast-spreading settings is relatively consistent (Barker et al., 2008). However, these values are much lower than those derived from the sheeted dike complex of ophiolites (e.g., >2.9 x 10^7; Bickle and Teagle, 1992). This was attributed to different Sr isotopic compositions of ancient oceans and protoliths (Gillis et al., 2005).

The Sr isotopic composition of hydrothermally altered plutonic crust is less well known. $^{87}Sr/^{86}Sr$ data for plutonic rocks recovered from the floor of the Hess Deep Rift

indicate low fluid/rock ratios (<1), but no fluid fluxes for this section were calculated (Lécuyer and Gruau, 1996).

1.5 Geological setting of the Hess Deep Rift and previous work

Samples studied in this thesis come from a ~4-km-wide and ~1-km-deep section within the northern escarpment wall at the Hess Deep Rift exposing the base of the sheeted dike complex and the upper plutonic section. This field area provides a unique opportunity to study the temporal (60,000 years) and spatial characteristics of magmatic and hydrothermal processes in the lower oceanic crust of a fast-spreading ridge setting and gives complementary information to findings from plutonic rocks recovered during the Ocean Drilling Program (ODP) Leg 147 (Lécuyer and Gruau, 1996). Compared to the plutonic section, the overlying sheeted dike complex and lava section at the Hess Deep Rift have been studied more extensively with respect to igneous and metamorphic petrology, contributing to the knowledge of magmatic and hydrothermal processes in fast-spreading ridge settings (e.g., Gillis et al., 1995, 2001, 2005).

1.5.1 Geologic background

The Hess Deep Rift is an east-west oriented, submarine rift valley located in the equatorial Pacific at the western tip of the Cocos-Nazca ridge (Figure 1.3). The Cocos-Nazca spreading center propagates westward into East Pacific Rise (EPR) crust at a rate of about 65 mm/year and is the driving force for the tectonic rifting that created the Hess Deep Rift Valley (Lonsdale, 1988). This special tectonic situation exposes young (~1

Ma) crust formed at the fast-spreading (~135 mm/year) EPR. These rocks crop out along escarpment walls forming the southern and northern margins of the rift valley, a horst block within the rift valley called the intra-rift ridge, and the rift valley floor. The exposed lithological units are a disrupted but nearly complete section of EPR crust including volcanics, sheeted dike complex, and plutonic section (Francheteau et al., 1990). Hence, this cross-section through a young EPR ridge flank, exposed nearly perpendicular to the spreading axis, provides a unique tectonic window that makes it possible to study spatial and temporal relationships in MOR-settings.

The geology of the Hess Deep Rift was explored during three submersible cruises, the first along the rift valley floor (Francheteau et al., 1990), followed by two that largely focused on the northern escarpment (Karson et al., 2002). During ODP Leg 147, Holes 894F and 894G penetrated and cored the upper plutonics that were tectonically exposed at the crest of the intra-rift ridge (Gillis et al., 1993).

The field area for this study is located along the northern escarpment of the Hess Deep Rift (Figure 1.3) where ~1 Ma crust is exposed. Samples were recovered by the submersible Alvin during cruises *R/V Atlantis II* 125-6 and *R/V Atlantis* 32-3 in 1990 and 1999, respectively (Figure 1.4), within a 4-km-wide area that represents a time span of 60,000 years (assuming a spreading rate of 135 mm/year). The volcanic sequence and the sheeted dike complex range in thickness from 200 to 800 m and 200 to 1000 m, respectively. Lava flows are increasingly deformed with increasing depth and dip towards the EPR (20°-70º). The dikes from the sheeted dike complex (>90% basaltic dikes) are rotated and dip east away from the EPR at an angle of ~60º. Intense rotation and

fracturing of the upper oceanic crust were interpreted to be a result of subaxial subsidence accommodating the mass of erupted material (Karson et al., 2002). Up to 1000 m of the plutonic sequence is exposed along the northern scarp of the Hess Deep Rift and is less affected by structural deformation. The transitions between the different units are gradual with dikes intruding into both the volcanic and plutonic sections (Karson et al., 2002). The plutonic section is made up of a variety of rock types including gabbros, Fe-Ti oxide gabbros, hornblende gabbros, gabbronorites and Fe-Ti oxide gabbronorites.

1.5.2 Previous work

Attempts to unravel the magmatic history of EPR-derived crust have been made in studies investigating the petrology and geochemistry of both the basaltic and gabbroic rocks from the Hess Deep Rift (e.g., Hékinian et al., 1993; Pedersen et al., 1996; Natland and Dick, 1996, 2009; Coogan et al., 2002a). Volcanic rocks from the northern escarpment generally have a geochemistry characteristic of N-MORB. However, lavas and dikes show variations in major and trace element contents (e.g., elevated CaO and Al_2O_3 in lavas) and probably represent distinct parental magmas that are juxtaposed in the two units (Stewart et al., 2002). Magmatic fractionation lead to density differences of melts forming dikes versus lavas affecting their eruptibility and therefore explaining their stratigraphic position within the upper crust (Stewart et al., 2002).

The upper 1 km of the plutonic section is exposed at the northern escarpment of the Hess Deep Rift and plutonic rocks are mostly made up of cumulates that have reacted with variable amounts of interstitial melt. Some authors suggest that these reactions are

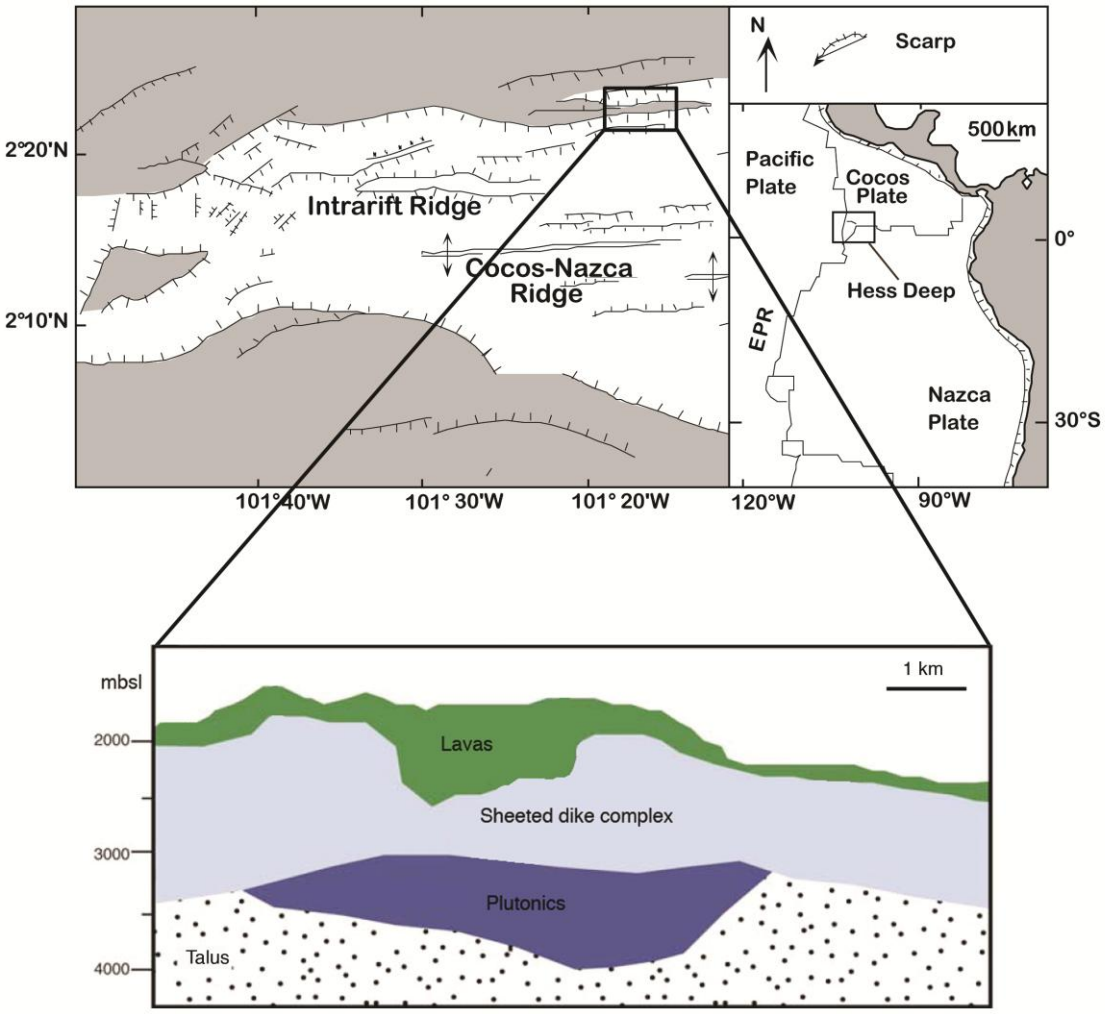

Figure 1.3: (Top) Location and schematic tectonic map of the Hess Deep Rift (after Lonsdale, 1988). The solid box identifies the field area for this study. (Bottom) Cross-sectional profile show the excellent exposure of young (~1 Ma) oceanic crust (Karson et al., 2002).

minimal and extraction of trapped melt is highly efficient leading to mixing and freezing of highly fractionated melts in a shallow magma body (Natland and Dick, 1996). Other authors argue that due to the observed decoupling of compatible and incompatible

elements, reaction with interstitial melt must be significant and explains the unusually high amount of incompatible elements in some lower plutonics (Pedersen et al., 1996; Coogan et al, 2002a). Furthermore, mineral chemistry and the presence of orthopyroxene in the plutonics suggest that melts reacted with the shallow mantle before injection into a melt lens (Hékinian et al., 1993; Coogan et al., 2002a). Due to the thickness of the horizon of varitextured gabbros and melt-rock density relations, the lower oceanic exposed at the Hess Deep Rift is inferred to have accreted in two or more magma bodies that are emplaced at different depths (Hanna, 2004; Natland and Dick, 2009).

Varitextured gabbros from the Hess Deep Rift follow two distinct liquid lines of descent potentially caused by different oxygen fugacities during crystallization. This was explained to be the result of assimilation of oxidized material affecting one group of rocks more than another. The distribution of these groups (lateral trend rather than depth trend) suggests a temporal rather than a spatial relationship with respect to differences in assimilation (Hanna, 2004).

Hydrothermal fluid ingress is evident in the crustal rocks at the Hess Deep Rift. High temperatures of alteration are recorded throughout the sheeted dike complex, although temperature conditions and degrees of alteration are spatially variable, ranging from subgreenshist to amphibolite facies conditions (100-800ºC) (Gillis, 1995; Gillis et al., 2001; Gillis et al., 2005). Fluid fluxes in the sheeted dike complex of the Hess Deep Rift

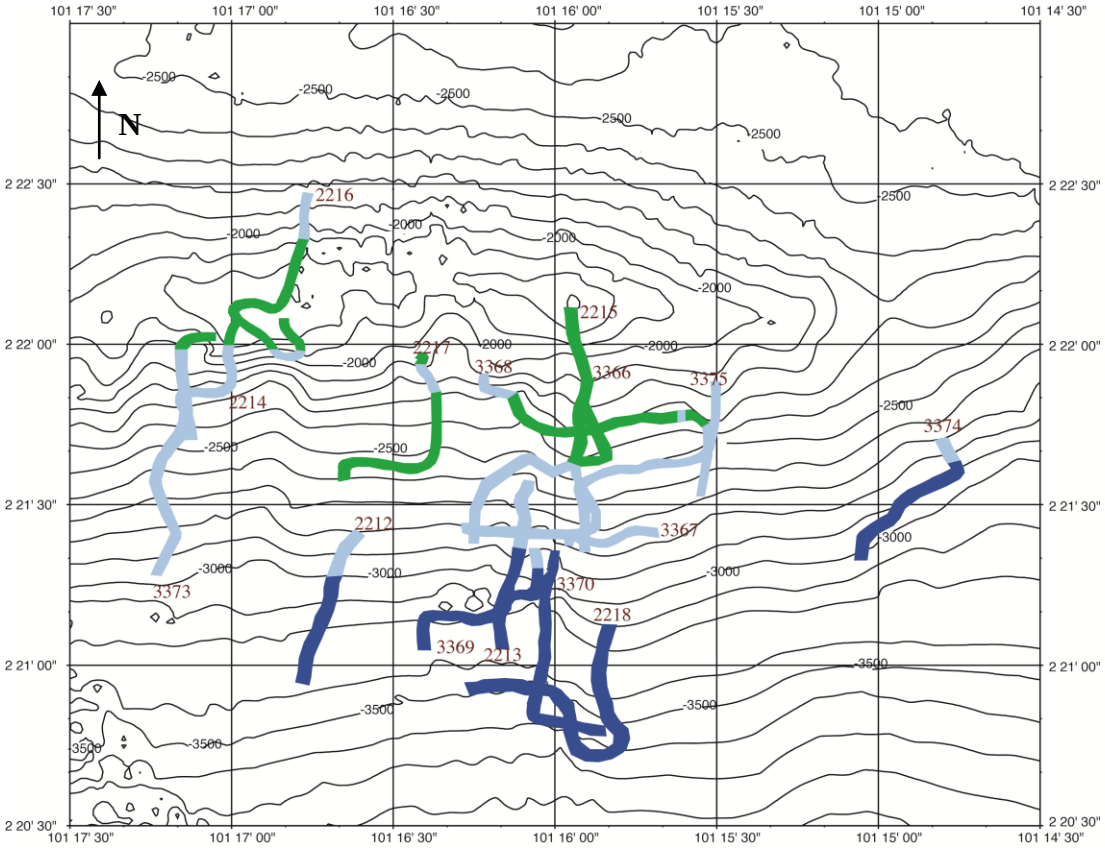

Figure 1.4: Bathymetric map of the field area showing dive tracks of the two Alvin dive programs in 1990 and 1999. Colours along the dive tracks symbolize different lithologic units: green = volcanic section; light blue = sheeted dike complex; dark blue = plutonic section. The numbers starting with 22xx and 33xx are Alvin dive numbers. Contour interval: 100 m.

were calculated to be 3.2 x 10^6 kg/m^2 (Gillis et al., 2005) and later revised to a value of 1.5 x 10^6 kg/m^2 using $^{87}Sr/^{86}Sr$. Especially in epidote-bearing samples, it was found that Sr content and Sr exchange during hydrothermal alteration is mineralogicallly controlled, affecting $^{87}Sr/^{86}Sr$ (Gillis et al., 2005).

Plutonic rocks generally record higher temperatures and lower degrees of alteration than the overlying sheeted dike complex (Gillis, 1995). Studies of microscopic veins suggest that incipient fluid penetration close to the ridge axis is likely short-lived and occurs by pervasive fluid flow along microfractures and grain boundaries at temperatures >700ºC (e.g., Manning et al., 1996). Anhydrous, hornfelsic assemblages are locally present in the plutonic section and indicate metamorphism in proximity to a heat source at temperatures >800ºC. Gillis (2008) interpreted these features to represent formerly altered rocks that were reheated due to the vertical migration of a melt lens. Localized fault zones within the sheeted dike complex and, less commonly, in the plutonic section lead to channelized fluid flow characterized by assemblages containing chlorite, actinolite, epidote and quartz (Hayman and Karson, 2007). As the system moved away from the ridge-axis, retrograde alteration assemblages indicative of metamorphism down to zeolite facies conditions overprint high-temperature assemblages; this is most prevalent in samples from the rift valley floor where alteration occurred in multiple stages, leading to complex alteration histories with time (Früh-Green et al., 1996).

1.4 Thesis goals

The goal of this study is to better understand the extent, timing and chemical fluxes of fluid-rock interaction altering the plutonic section at fast-spreading ridges. This will be approached by investigating the geochemistry, mineralogy and regional distribution of hydrothermally altered plutonics from the Hess Deep Rift. $^{87}Sr/^{86}Sr$ will be used as a geochemical tracer to assess the relative amount of fluid penetrating these crustal levels. In order to evaluate the limitations of this tracer, a special focus will be given to Sr behaviour under high-temperature hydrothermal conditions. Key questions addressed in this thesis include:

- Are there spatial and/or temporal trends with respect to alteration characteristics?
    - Do hydrothermal mineral assemblages and abundance of secondary minerals vary with depth or laterally?
    - Which elements are exchanged between fluids and rock, and where?
- How does Sr behave in high-temperature hydrothermal systems?
    - Is Sr enriched or depleted in the plutonic crust during hydrothermal alteration under the high-temperature conditions?
    - In which igneous and hydrothermal minerals does Sr reside and is there a link between alteration conditions and Sr exchange?
- What are the fluid/rock ratios in the plutonic section on- and near-axis?
    - What parameters need to be taken into account when quantifying fluid-rock interaction using the $^{87}Sr/^{86}Sr$ of altered rocks?

- How does the fluid/rock ratio in the plutonic section compare to the sheeted dike complex at the Hess Deep Rift?
- How are hydrothermal and magmatic systems related?

Chapter 2

SR BEHAVIOUR DURING HYDROTHERMAL ALTERATION OF OCEANIC GABBROS EXPOSED AT HESS DEEP – IMPLICATIONS FOR $^{87}SR/^{86}SR$ COMPOSITIONS AS A PROXY FOR FLUID-ROCK INTERACTION

2.1. Introduction

At mid-ocean ridges, cold seawater penetrates young, permeable oceanic crust to become part of a thermally-driven hydrothermal system that controls elemental fluxes between the earth's interior and the oceans, and the cooling of the lithosphere. The discrepancy between modelled and measured conductive heat flow in young oceanic lithosphere suggests that almost 50% of the heat transfer at MORs is accommodated by hydrothermal circulation. Furthermore, an estimated 30% of lithospheric heat removed by convection occurs within ~1 Ma of crustal accretion even though MORs represent only ~2% of the area affected by advective heat transfer (Stein and Stein, 1992).

The nature of lower crustal accretion is directly linked to the geometry of the hydrothermal system controlling the removal of the latent heat of crystallization (e.g., Phipps Morgan and Chen, 1993; Henstock et al., 1993; Coogan, 2008). At intermediate- to fast-spreading ridges, two end-member models predict the style of accretion of the lower oceanic crust. First, in the gabbro glacier model, all crystallization occurs in a small, shallow magma lens followed by crystals subsiding in a mush zone that extends to the base of the crust (e.g., Nicolas et al., 1988; Quick and Denlinger, 1993). In this

scenario, the base of the hydrothermal system is expected to be located near the base of the sheeted dike complex with the heat being removed by hydrothermal fluids at relatively shallow levels. Second, the sheeted sill model proposes that crystallization of gabbroic rocks occurs in multiple sills located at different depths between the Moho and the base of the sheeted dike complex (e.g., Kelemen et al. 1997). This model requires the penetration of hydrothermal fluids to considerable depths close to the ridge axis in order to remove the latent heat of crystallization.

To gain insight into the amount and spatial characteristics of hydrothermal heat transfer, fluid and chemical fluxes at and near the ridge axis need to be understood. Based on vent fluid chemistry, which integrates the reaction path of a given fluid at a specific time, experimental studies and the investigation of hydrothermally altered rocks from modern mid-ocean ridge settings and ophiolites, efforts have been made to constrain these fluxes (e.g., Mottl, 1983; Von Damm, 1990; Berndt and Seyfried, 1988; Alt, 1995; Bickle and Teagle, 1992; Gillis et al., 2005).

$^{87}Sr/^{86}Sr$ has been found to be a useful geochemical tracer to quantify fluid-rock interaction due to contrasting characteristic $^{87}Sr/^{86}Sr$ of fresh rock and seawater (e.g., Bickle and Teagle, 1992). If the $^{87}Sr/^{86}Sr$ of the fresh rock in question is known, then the $^{87}Sr/^{86}Sr$ of altered rock can be used to quantify the amount of fluid that reacted with the oceanic crust (e.g., Albarède, 1981; Bickle and Teagle, 1992; Gillis et al., 2005; Barker et al., 2008). This approach was applied for hydrothermally altered rocks from sheeted dike complexes from three intermediate-to fast-spreading settings (Teagle et al., 2003; Gillis

et al., 2005; Barker et al., 2008), but quantification of fluid-rock interaction in underlying plutonic sections is scarce (e.g., Lécuyer and Gruau, 1996).

A challenge in using Sr isotopic ratios to trace fluid-rock interaction is that the behaviour of Sr in hydrothermal systems is not well known and likely is not constant under changing conditions within the hydrothermal system. Controls on Sr exchange have been investigated for hydrothermal conditions in sheeted dike complexes (Gillis et al., 2005; Barker et al., 2008), but has so far been neglected with respect to the plutonic sections. The goal of this study is to close this gap and examine the mineralogically-controlled Sr behaviour in gabbroic rocks under a range of hydrothermal conditions. To do this, hydrothermally altered plutonic rocks that formed at the fast-spreading EPR and were recovered during two Alvin dives along the northern wall of Hess Deep, are studied. The metamorphic characteristics and bulk rock and mineral compositions are used to evaluate what controls Sr isotopic exchange and calculate fluid/rock ratios for the plutonic section.

2.1.1. Geologic background

The Hess Deep Rift is an east-west oriented, submarine rift valley located in the equatorial Pacific at the western tip of the Cocos-Nazca ridge (Figure 1.3). The Cocos-Nazca spreading center propagates westward into East Pacific Rise crust at a rate of about 65 mm/year and is the driving force for the tectonic rifting that created the Hess Deep Rift Valley (Lonsdale, 1988). This special tectonic situation allows for the exposure of crust formed at the fast-spreading (~135 mm/year) EPR (Figure 1.3). East Pacific Rise

crustal rocks crop out in several horst blocks along the rift valley floor and the bounding escarpments (Francheteau et al., 1990). Hence, the cross-section through a young EPR ridge flank, exposed nearly perpendicular to the spreading axis, provides a unique tectonic window that makes it possible to study spatial and temporal relationships in MOR settings.

The focus of this study is the northern escarpment of the Hess Deep rift where a complete upper crustal section of ~1 Ma is well exposed. A 4-km-wide area, representing a time span of ~60,000 years (Karson et al., 2002), was investigated with the submersible during cruises *R/V Atlantis* II 125-6 and *R/V Atlantis* 32-3 in 1990 and 1999, respectively. The volcanic sequence and sheeted dike complex range in thickness from 200 to 800 m and 200 to 1000 m, respectively. The sheeted dikes (>90% basaltic dikes) generally dip east at an angle of ~60º (Karson et al., 2002). Additionally, up to 1000 m of the plutonic sequence is exposed. The transitions between these units are gradational, with dikes intruding into both the volcanic and plutonic sections (Karson et al., 2002). The plutonic section is made up of a variety of rock types including gabbros, Fe-Ti oxide gabbros, hornblende gabbros, gabbronorites and Fe-Ti oxide gabbronorites.

2.2. Analytical methods

Thirty-one gabbroic rocks representative of all rock types and their regional distribution and alteration characteristics were selected for trace element analysis. Oxidized edges were removed and macroscopic alteration haloes were avoided. Bulk rock trace element concentrations were analyzed using a Thermo X Series II inductively-coupled-plasma-mass-spectrometer (ICP-MS) at the University of Victoria following the modified procedure of Eggins et al. (1997). Rock standards BIR-1, W2-A, BVHO-2 were analyzed for calibration at the beginning and end of the analyses. A solution containing a mixture of the different standards was used to monitor the drift during an analytical session (Appendix B). The reproducibility of the standards for Sr was within 1% for all standards. For BVHO-2 all elements were reproduced within 5%. For W2-A only Cr had a difference percentage of >5% (6.1%). The largest errors were found in the reproducibility of BIR-1, where eight species have an error of >5%, three of which are >10% (maximum: Cs = 15.9% difference). Existing data for selected trace elements for a sub-set of samples analyzed by Natland and Dick (1996) are generally in good agreement with most of the species analyzed (Appendix B). Some elements (e.g. Cr, Cu and Zn) may deviate >20% in one sample, but <5% in another sample. Zr analyses from this study were found to be systematically lower than in analyses from Natland and Dick (1996) (Appendix B), suggesting that zircon was not or incompletely dissolved during rock powder digestion. Zr data was therefore excluded from the data table (Table 1).

$^{87}Sr/^{86}Sr$ was determined following the approach of Weis et al. (2006). Twenty -nine bulk rock powders, two epidote separates and two plagioclase separates were analyzed in

two separate runs. The mineral separates were leached in hot 6N HCl for 30 minutes prior to digestion. For isotopic analysis, Sr was separated using standard cation exchange techniques and then analyzed in a Triton thermal ionization mass spectrometry (TIMS) at the Pacific Centre for Isotopic and Geochemical research, University of British Columbia. Analyses of the SRM987 standard yielded values of 0.710242±0.000009 (2σ; n=11) and 0.710247±0.000018 (2σ; n=15) for two separate runs with a reference value of 0.710248. Four duplicates reproduced the analyses within ±0.00001 (average ±0.000007).

Trace element concentrations of igneous and metamorphic minerals were determined using laser ablation inductively coupled plasma mass spectrometer (LA ICP-MS) at the University of Victoria. NIST 615, NIST 613 and NIST 611 were used as external standards for calibration and as instrumental drift monitors. ^{42}Ca or ^{43}Ca were used as internal standards for the analyses. For analytical sessions focusing on Sr in plagioclase, plagioclase glass standards (An_0, An_{25}, An_{50}, An_{75} and An_{100}) were used for calibration of anorthite content and were run at the beginning and the end of each analytical session. The reproducibility of Sr and Ba contents is good for most of the analyses with less than 5% difference between average measured values and preferred values for NIST 613 and NIST 611(Appendix D). For NIST 615, average measured values deviated up to ~10% for Sr and up to 12% for Ba. However, this slightly higher deviation occurred in a run where only plagioclase was analyzed such that the precision of standards with higher Sr contents like NIST 611 and NIST 613 is more meaningful. The reproducibility of NIST standards for other elements is generally good with some average measured values deviating as much as 50% from the preferred value (Appendix D.2). Major and minor

element compositions of igneous and metamorphic minerals were determined using a Cameca SX-50 scanning electron microprobe at the University of British Columbia. The microprobe was operated at 15 kV accelerating voltage, a 20 nA beam current, and a beam diameter of 5 μm.

Secondary plagioclase was identified using Hitachi S-4800 field emission scanning electron microscope (FESEM) at the University of Victoria, and a Cambridge Cathode Luminescence Instrument (CITL 8200 mK4) at the University of British Columbia.

2.3. Results

2.3.1. Regional petrology

2.3.1.1. Igneous petrology

The primary rock types in the upper plutonics include Fe-Ti oxide and hornblende gabbro, varitextured gabbro, gabbronorite, and rare Fe-Ti oxide gabbronorite (this study; Natland and Dick 1996). Note that Fe-Ti-oxide gabbros were previously described as oxide ferrogabbros (Natland and Dick, 1996, 2009). A 150-200 m thick gabbro unit is located directly beneath the sheeted dike complex and overlays a ≥250 m-thick gabbronorite unit (Figure 2.1a). The thickness of the latter unit is a minimum value due to restricted sampling depth. Note that rare gabbros are found at greater depth within the gabbrononorite unit. Fe-Ti-oxide (±hornblende) gabbro is concentrated in a 200-300 m-wide area close to the base of the sheeted dike complex in the central region of the field area (dives 3369 and 3370) (Figure 2.1a). Isolated Fe-Ti-oxide hornblende gabbro and hornblende gabbronorite are scattered at greater depths throughout the central part of the field area (including the deepest sample at 3537 m). Two of these samples contain recrystallized hornblende and are hereinafter referred to as hornblende hornfels (Figure A.1g). Varitextured gabbros occur in the westernmost part of the study area (dive 2212) (Figure 2.1a). Texturally, the gabbros are primarily medium-grained and varitextured (intergranular to subophitic) or equigranular.

Gabbronorites are generally coarser-grained than gabbros (medium to coarse-grained) and contains rare olivine (two samples). Orthopyroxene typically forms large, anhedral grains or oikocrysts hosting clinopyroxene and plagioclase (Figure A.1d). Plagioclase and

clinopyroxene vary in size on a sample-scale ranging from fine-grained chadacrysts to coarser grains. Medium- to coarse-grained, intergranular plagioclase laths show a preferred orientation in several gabbronorite samples (this study; Coogan et al., 2002a).

Dikes are distributed throughout the upper plutonic section and were recovered from depths of up to >500 m below the base of the sheeted dike complex. These dikes are fine-grained with intersertal textures and contain hydrous secondary assemblages that are similar to the sheeted dike complex (Gillis et al., 2001).

2.3.1.2. Metamorphic petrology

The plutonic samples are characterized by three styles of interaction with hydrothermal fluids. First, most samples were altered by pervasive fluid flow along grain boundaries and microfractures (Figure 2.2a,b), henceforth these samples are referred to as pervasively altered samples. Some gabbroic samples in the western field area are cross-cut by macroscopic veins (~1 mm wide). Alteration haloes adjacent to these veins are small (≤1 mm) and were avoided for the preparation of bulk rock powders. Therefore these samples can be regarded as being altered pervasively along grain boundaries and microfractures only. Second, two samples from the far eastern part of the field area are characterized by cataclastic textures and epidote-bearing assemblages indicative of localized focused fluid flow, henceforth these samples are referred to as being from focused fluid flow zones. Third, some samples show anhydrous, granoblastic textures (Figure 2.2c) suggesting high-temperature recrystallization that post-dates pervasive alteration, henceforth these samples are referred to as pyroxene hornfels.

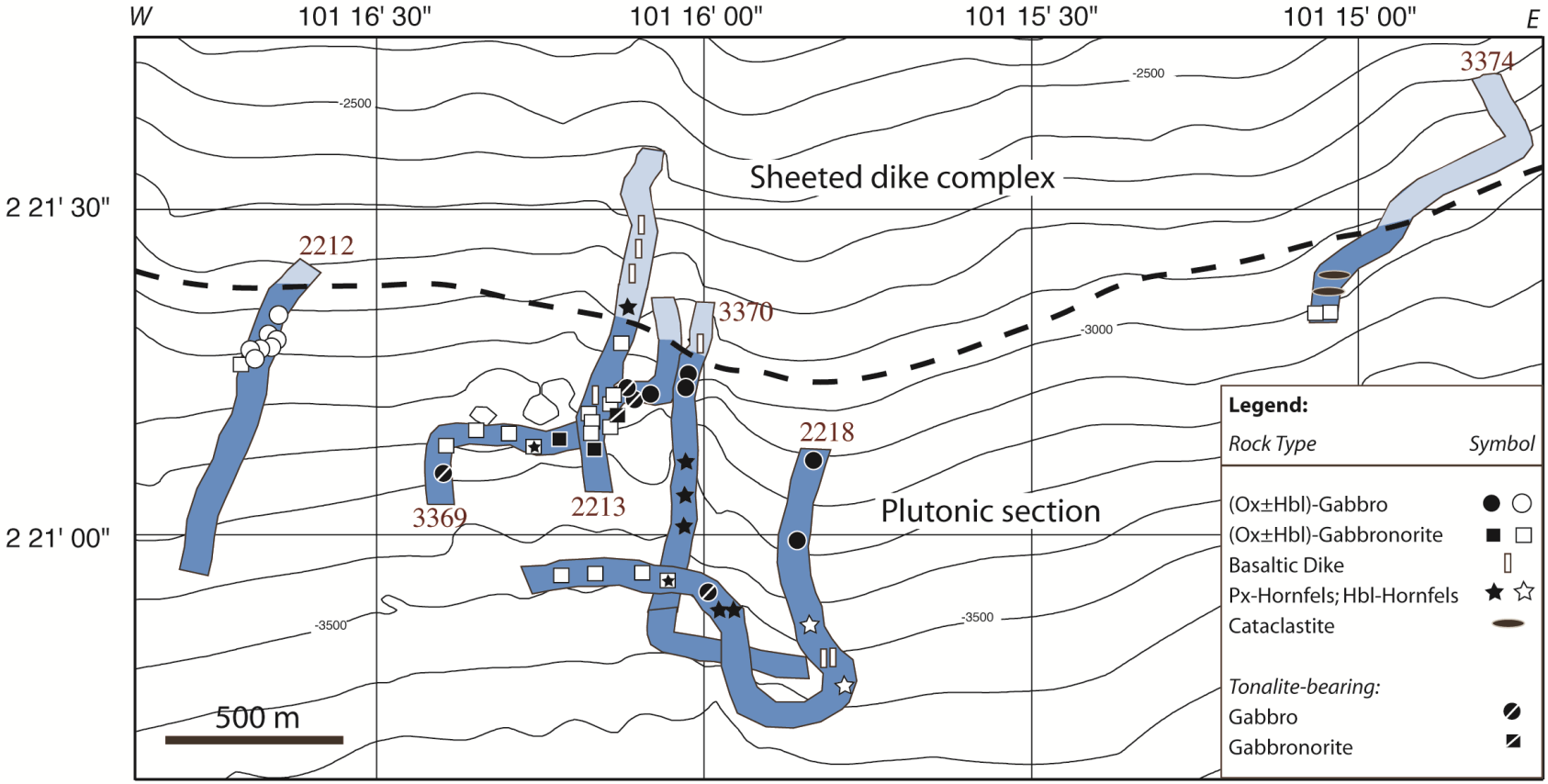

Figure 2.1a: Simplified geological map of the study area showing dive tracks and the general lithological boundary between the sheeted dike complex (light blue) and the gabbroic sequence (dark blue) (Karson et al., 2002). The symbols along each dive track indicate the location and igneous rock type of studied samples. Filled and open symbols are Fe-Ti-oxide (±hornblende) gabbro(norite) and gabbro(norite), respectively. The dashed line marks the approximate location of the sheeted dike-gabbro transition. Contour interval: 100 m.

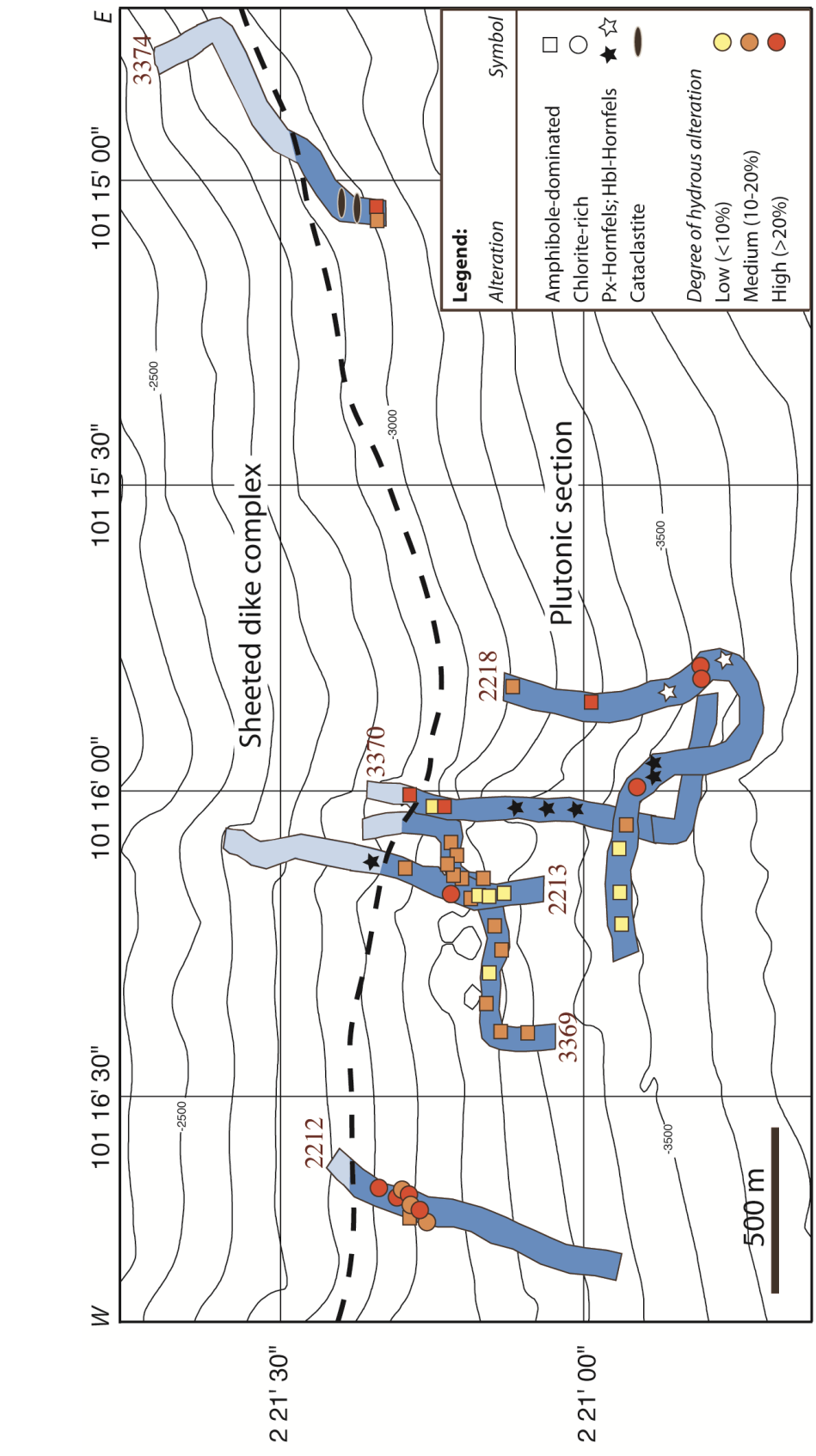

Figure 2.1b: Simplified alteration map showing key alteration characteristics. Symbols along each dive track show locations of studied samples, the style of hydrothermal alteration and an index of the degree of hydrous alteration.

The percentage of hydrous secondary phases for the pervasively altered samples was determined by point-counting thin sections (Appendix B.2). Secondary plagioclase was not included because accurate data cannot be obtained using a standard petrographic microscope. Thus, the percentage of hydrous secondary phases is indicative of the minimum value for the overall degree of alteration. For plutonic rocks, the percentage of hydrous minerals is variable, ranging from <5 to >20% (Table 1) and shows a gradual decrease with depth below the sheeted dike complex, although two strongly altered gabbroic samples from deeper levels lie off this trend. Gabbros are generally more altered than gabbronorites (Figure 2.3). One dike hosted in the plutonic section shows substantially higher hydrous alteration percentage (~55%).

The pervasively altered samples are mostly amphibole-dominated, with chlorite-rich samples (>25% of total hydrous secondary minerals) from the western part of the field area, a few of which are chlorite-dominated (>50% of total hydrous secondary minerals) (dive 2212) (Figure 2.1b). Clinopyroxene is variably replaced (<2% to ~70%) by amphibole ± chlorite ± magnetite ± minor secondary clinopyroxene. Orthopyroxene alters to randomly oriented veinlets and patches of colorless intermixed low-Ca amphibole and talc ± magnetite or green amphibole ± magnetite, and shows a wider range of replacement (<5% to 100%). Magmatic plagioclase ($An_{\sim35}$ to $An_{\sim70}$) commonly alters to secondary plagioclase ($An_{<5}$ to $An_{>80}$) with minor to rare amphibole locally filling microfractures. Secondary plagioclase identified using backscattered electron (Figure A.1k) and cathodoluminescence (Figure A.1l) images has either more albitic or more anorthitic compositions relative to the primary phase, respectively. Albitic secondary

plagioclase is relatively rare and was found in <40% of the samples where it represents up to 10-15% of the plagioclase in a given sample (Figure A.1k) with most occurrences making up <5% of plagioclase. More anorthitic secondary plagioclase, observed in one sample only, makes up 30-40% of the plagioclase (Figure A.1l). Secondary plagioclase of intermediate anorthite content (~An_{30}-An_{60}) could only be identified by Fe-depletion (determined by electron microprobe), thus, accurate quantification of this phase was not possible. Therefore, reported percentage of secondary plagioclase for all samples is a minimum value.

Alteration patches filled with amphibole and/or chlorite ± magnetite ± talc are common in all rock types and range in size from 0.1 to >2 mm. In many samples, these patches are interstitial to plagioclase suggesting that they are complete replacements of pyroxene or myrmekitic areas.

Microscopic veins (<40 μm wide) along grain boundaries or cutting primary grains are ubiquitous and contain amphibole or chlorite. Macroscopic hydrothermal veins occur in <10% of the gabbroic samples. These veins are filled with quartz ± chlorite ± amphibole or amphibole only. Alteration haloes adjacent to these veins are restricted to a distance of 1-2 mm from the vein margin.

The hornfels samples are partially or completely recrystallized to either pyroxene hornfels (clinopyroxene, orthopyroxene, plagioclase, Fe-Ti-oxides) or hornblende hornfels (hornblende, clinopyroxene, orthopyroxene, plagioclase, Fe-Ti-oxides). In hornblende hornfels, hornblende is completely recrystallized, and plagioclase and pyroxenes (both orthopyroxene and clinopyroxene) are partly recrystallized or display

a)

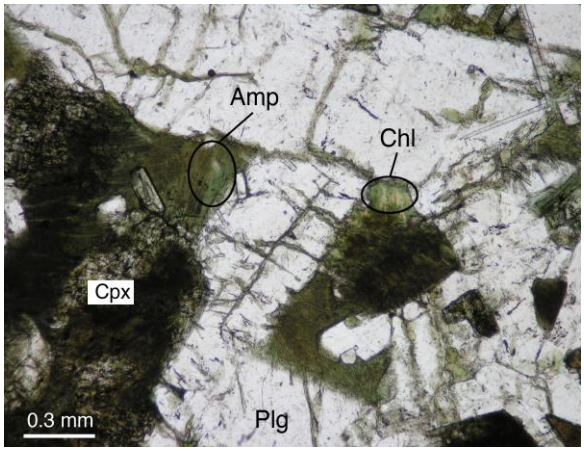

b)

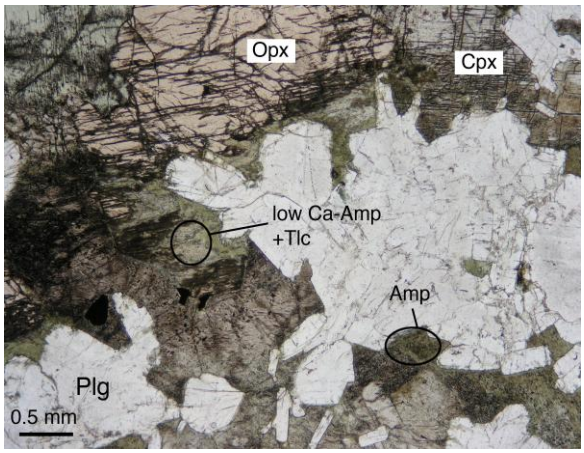

c)

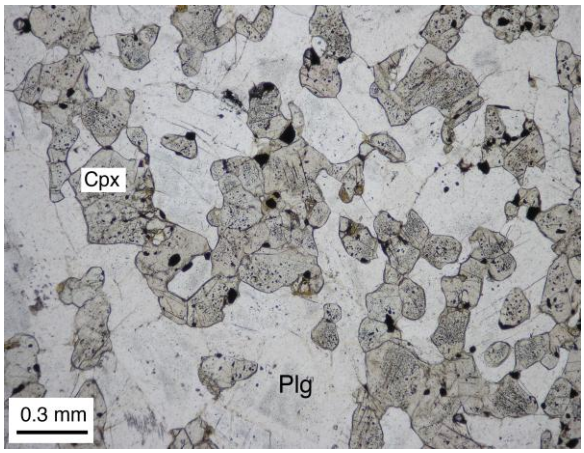

Figure 2.2: Photomicrographs of three representative rock types and alteration characteristics; a) pervasively altered (22%), varitextured gabbro partly replaced by a secondary mineral assemblage containing fibrous amphibole and chlorite (2212-1500); b) pervasively altered (10%) gabbronorite partly replaced by fibrous amphibole and low Ca-amphibole ± talc (3369-1321); c) fine-grained pyroxene hornfels with granoblastic texture and minor late-stage alteration (3370-1205). Abbreviations: Plg=plagioclase, Cpx=clinopyroxene, Opx=orthopyroxene, Chl=chlorite, Amp=amphibole, Tlc=Talc.

magmatic (i.e. subophitic to poikilitic) textures, respectively. Pyroxene hornfels, in contrast, is commonly completely recrystallized with local preservation of magmatic textures of plagioclase. The protolith of most hornfels samples is gabbro or gabbronorite, as evidenced by relict primary minerals and/or textures. One sample has a sharp transition (<2 mm) between fine and medium-grained domains, suggesting the sample represents a hornfelsed dike–gabbro (or slightly coarser dike) contact. In hornblende hornfels, secondary amphibole and talc occur as hydrous alteration products (8% and 16%). Abundant anorthitic secondary plagioclase (30-40%) was found in one of the hornblende hornfels. Pyroxene hornfels is largely anhydrous and if hydrous alteration occurs it is represented by veins and patches of low-temperature clay assemblages making up <5% of the total assemblage.

Lastly, two samples recovered from the far eastern part of the study area (dive 3374) are interpreted to have formed in a zone of focused fluid flow (Hayman and Karson, 2007), one is cataclastically deformed and the second is altered to an epidote-quartz-chlorite mineral assemblage (Figure A.1j).

2.3.1.3. Temperature constraints

The peak temperatures of hydrothermal alteration in the amphibole-bearing, pervasively altered gabbroic rocks have been constrained using the edenite + albite = richterite + anorthite exchange geothermometer developed by Holland and Blundy (1994), assuming a pressure of 0-2 kbars. For reliable results, this thermometer should be used in the temperature range of 500-900 ºC and with plagioclase between An_{10} and An_{90}

(Holland and Blundy, 1994). In rocks from the northern scarp of Hess Deep, calculated temperatures range from 665 to 858ºC (this study; Coogan et al., 2003; Manning et al., 2000; Weston, 1998). The Al^{IV} content in hydrothermal amphibole may be used to qualitatively assess temperature, as experimental studies have shown Al_2O_3, TiO_2, and Na_2O contents increase with increasing temperature (e.g., Liou et al., 1974), such that magnesio-hornblende (Al^{IV} contents > 0.5; based on 23 oxygens) is indicative of amphibolite facies conditions (>450ºC to ~700 º C), whereas actinolite (Al^{IV} contents <0.5) suggests lower temperatures (down to 250°C) (e.g., Liou et al., 1974; Schiffman and Fridleifsson, 1991). There is no systematic trend of temperature or Al^{IV} in hydrothermal amphibole with depth (Figure A.5). Mean Al^{IV} in hydrothermal amphibole is highest in the central and western part of the study area (~0.8) and lower in the far eastern parts (~0.5) suggesting lower peak alteration temperatures or more pronounced retrograde alteration in this area. Temperature conditions within the sheeted dike complex from Hess Deep were estimated using the same approach, yielding no regional trends with depth or laterally (Gillis et al., 2001). Peak temperatures for the basal dikes were calculated using the plagioclase-hornblende geothermometer (Holland and Blundy, 1994) and range from 609-733ºC (Gillis et al., 2001).

Lateral variability of secondary mineral assemblages and Al^{IV} in amphibole suggests different temperature conditions with time. Chlorite-rich assemblages are concentrated in the western part of the field area, where samples may lack amphibole completely, but are locally found throughout the field area. The presence of discrete chlorite indicates a minimum temperature of 160-270ºC and, in association with actinolitic amphibole, a

maximum temperature of ~ 450ºC (e.g., Schiffman and Staudigel, 1995; Liou et al, 1974). The far eastern part of the field area, in contrast, is largely characterized by net-veining and cataclastic deformation with mineral assemblages typical of focused fluid flow zones.

Pyroxene and hornblende hornfels were recovered from the central part of the field area. Peak temperatures calculated for the pyroxene hornfels using the two pyroxene thermometer of Andersen et al. (1993) range from 756-1024ºC (Gillis, 2008). These high temperatures are consistent with the calculated temperatures for amphibole, as well as elevated mean Al^{IV} in hydrothermal amphiboles of this area.

In summary, the observed regional variability in the temperature of peak alteration on lateral length scales of 1-2 km along the northern escarpment indicate that thermal conditions within the hydrothermal system fluctuated from <450ºC to >800ºC (pyroxene hornfels not considered) on timescales of less than 20,000 years.

Retrograde alteration occurred over a wide temperature range (>600 ºC) and encompasses upper amphibolite to greenshist facies conditions. The largest variability in temperature conditions was found in the western part of the study area, where high-temperature amphibole coexists with chlorite. In a few samples from the central area, oxidized veins containing clay minerals suggest late-stage alteration under low-temperatures, but these are interpreted to be associated with seawater-ingress during the tectonic opening of the rift valley.

2.3.2. Bulk rock chemistry

Plutonic rocks from the northern scarp of Hess Deep show a wide range of Mg# (0.76 to 0.30) with gabbronorite being the most primitive and Fe-Ti oxide gabbro being the most evolved end-members (this study; Natland and Dick, 1996, 2009; Hanna, 2004). In general, plutonic rocks from the northern escarpment are more evolved than those recovered from the rift valley floor (Hekinian et al., 1993; Pedersen, 1996; Coogan et al., 2002a). Mg# is strongly positively correlated with CaO and Al_2O_3 content, suggesting that plagioclase crystallization controls the magmatic evolution of these rocks. Interestingly, the correlation of CaO and Na_2O is relatively weak considering the solid solution behavior of these two species in plagioclase (Figure 2.5). Furthermore, Na_2O shows a weaker correlation to Al_2O_3, Mg# or P_2O_5 than CaO, suggesting that CaO follows the magmatic evolution in a more pronounced way. Strong negative correlations of Mg# with FeO and TiO_2 up to an Mg# of ~0.5, and subsequent increased scatter at lower values, suggest that Fe-Ti oxide saturation was reached at this point. Rocks with Mg# below 0.4 generally contain minor tonalitic veins.

The percentage of hydrous secondary phases is positively correlated with Na_2O, FeO, and P_2O_5 and negatively correlated with Al_2O_3, CaO and Mg# (Figure 2.3). Additionally, incompatible and largely immobile trace elements, such as Y, Nb or La, increase with increasing alteration percentage suggesting that more differentiated rocks are altered more strongly. However, it remains unclear whether regional distribution of rock types or higher susceptibility to hydrous alteration of more evolved rocks is responsible for this trend.

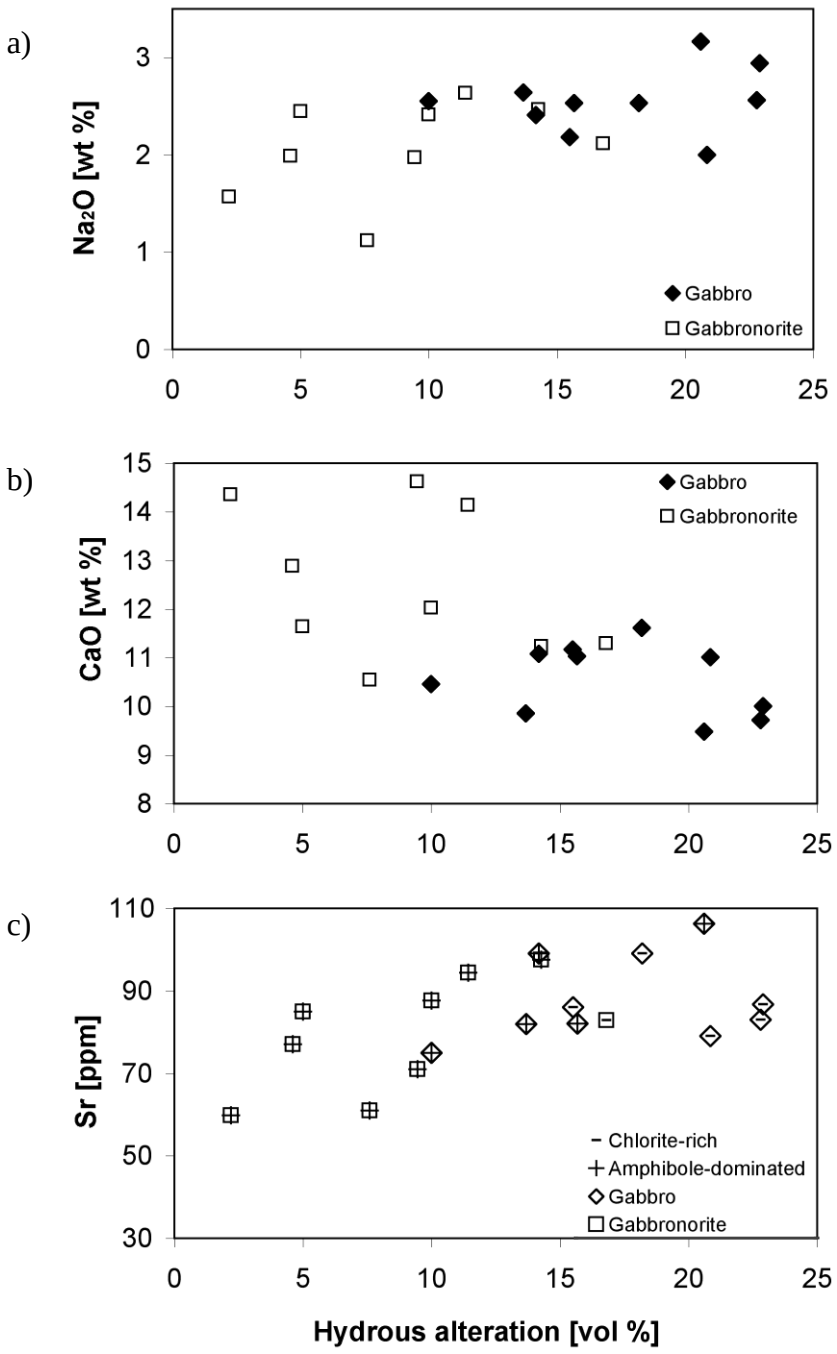

Figure 2.3: Correlation of % hydrous alteration with bulk rock Na_20, CaO, and Sr content. (a,b) Samples differentiated by rock type. More evolved rocks generally show a higher percentage of hydrous alteration. (c) Samples differentiated by rock type and hydrous alteration assemblage. Sr increases with increasing hydrous alteration for amphibole-dominated assemblages; no correlation is recognizable for chlorite-rich assemblages. Note that chlorite-rich assemblages may still contain substantial amounts of amphibole. The observed trend is interpreted to be due to a mineralogical and temperature-dependence of Sr exchange during hydrothermal alteration (see text for discussion).

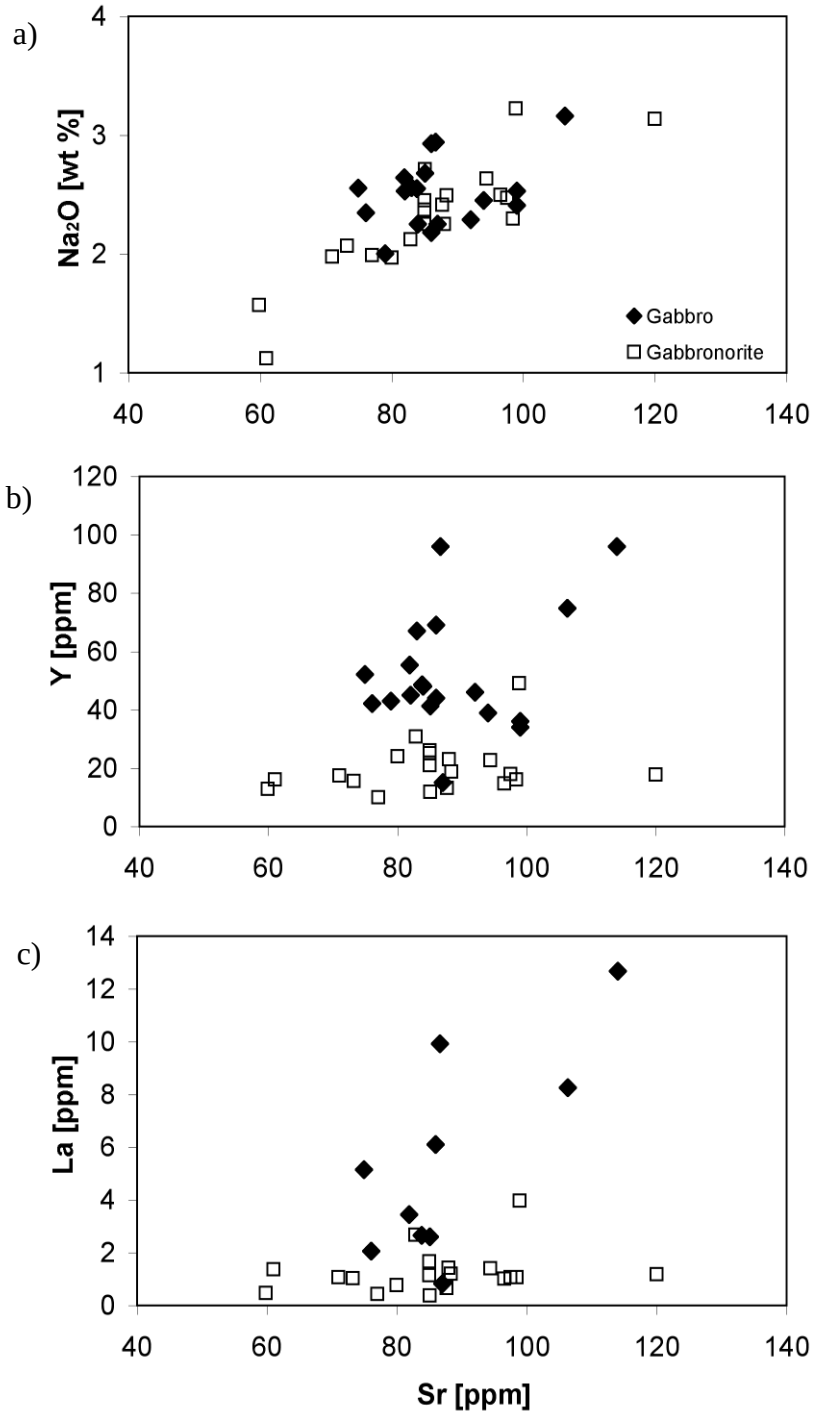

Figure 2.4: Bulk rock Sr content versus a) Na_2O, b) La and c) Y content for different rock types. Sr is well correlated with Na_2O, but not with La or Y. The higher magmatic differentiation of gabbro versus gabbronorite is identifiable in the plots showing La and Y. This suggests that the correlation of Sr and Na_2O is at least partly dependent on hydrothermal redistribution.

Strontium contents of pervasively altered gabbroic rocks range from 60 to 137 ppm. One epidote-bearing sample from a focused fluid flow zone in the eastern part of the field area has a Sr content of 227 ppm. Sr contents do not vary systematically with depth below the sheeted dike complex. There is a weak or no correlation between Sr and magmatic differentiation proxies (e.g., Mg#, Y, REE) (Figure 2.4b,c). There is a positive correlation of Sr with Na_2O (2.4a) and the percentage of hydrous alteration (Figure 2.3a). This may partly result from the aforementioned increased hydrous alteration of more evolved rocks and/or uptake of Sr during hydrothermal alteration.

A common approach to quantify Sr mobility in hydrothermally altered rocks is to compare measured Sr values to calculated magmatic trends, such that deviations from these trends reflect loss or gain (e.g., Barker et al 2008). Results for the Hess Deep sheeted dike complex show that Sr shows no change or is depleted relative to fresh rock values (Gillis et al., 2005). Application of this approach for the Hess Deep gabbroic rocks proved problematic, as the uncertainty in modelling magmatic trends for plutonic rocks is much larger than for extrusive rocks. This is mostly due to the unknown amount of trapped melt within plutonic rocks. Additionally, Sr is compatible in plagioclase (with different partition coefficients for different anorthite contents), but incompatible in other rock-forming minerals of gabbroic rocks (e.g., Blundy and Wood, 1991). Even though no clear correlation was observed between the modal abundance of plagioclase and bulk rock Sr (Figure 2.6) (potentially due to point counting uncertainties), plagioclase likely controls Sr distributions in plutonic rocks which complicates the modeling of a magmatic

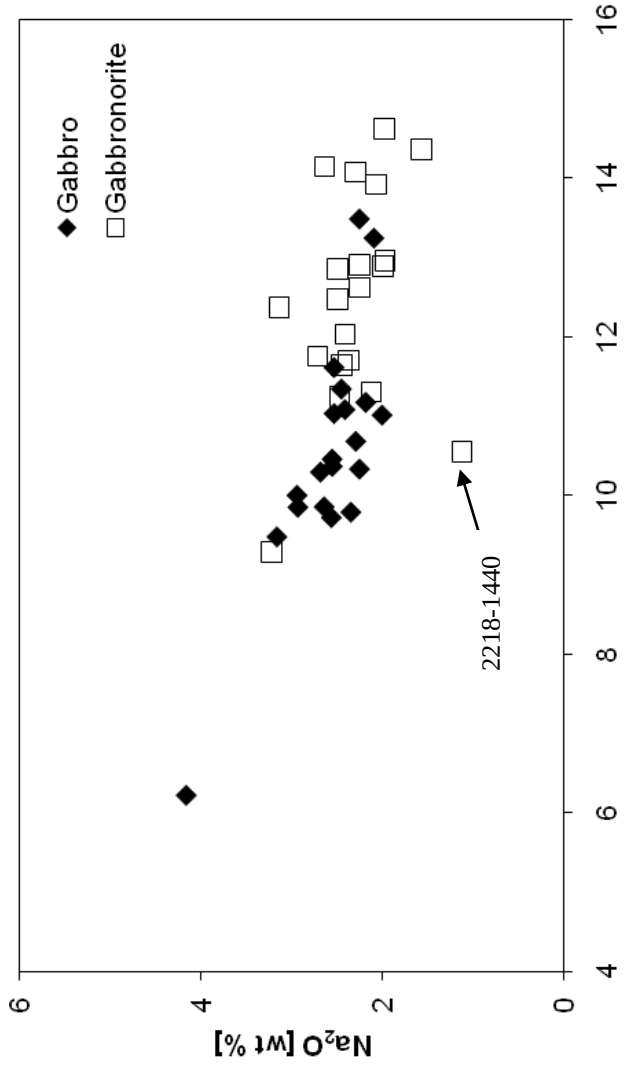

Figure 2.5: Bulk rock Na2O content versus CaO. A negative correlation is visible, but weaker than expected considering that the solid solution behaviour of these species in plagioclase controls their relative proportions. The sample with the lowest Na_2O content is the hornblende hornfels (2218-1440) with anothitized secondary plagioclase suggesting that plagioclase alteration contributes to the scatter in the observed trend.

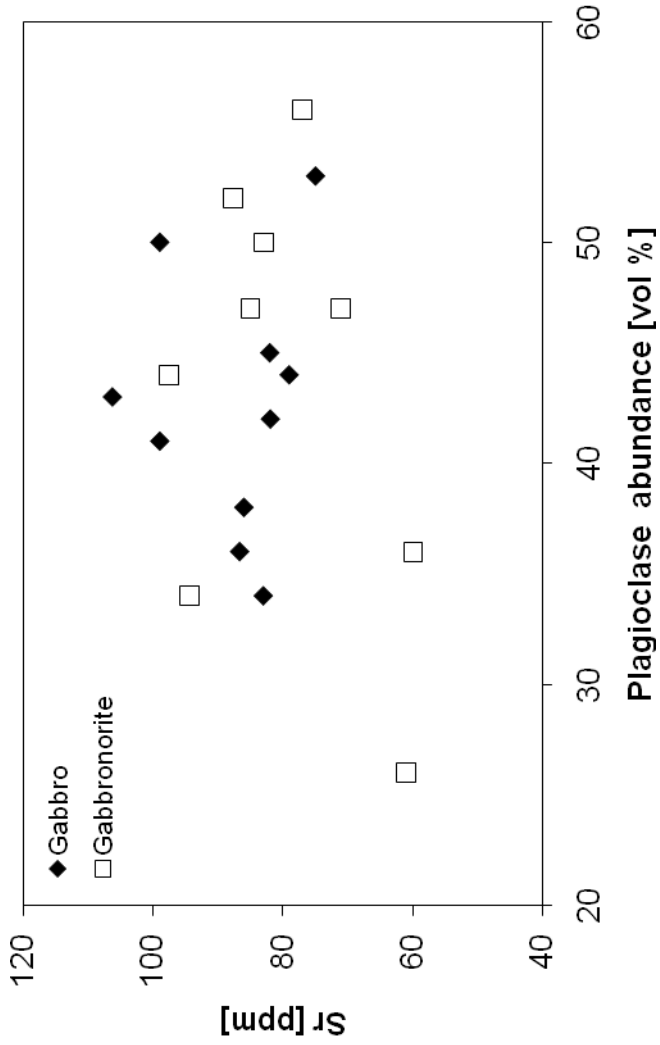

Figure 2.6: Modal abundance of plagioclase versus bulk rock Sr content. The lack of a correlation may be a result of point counting uncertainties or significant hydrothermal redistribution of Sr in the plutonic rocks.

trend. For these reasons, it was not possible to rigorously assess Sr mobility. For information on the modelling see Appendix A.2.2.

2.3.3. Sr contents of igneous and hydrothermal minerals

Strontium contents were obtained for the major primary and secondary minerals in order to constrain the distribution of Sr in the hydrothermally altered rocks and to evaluate the impact of different secondary mineral assemblages on the Sr budget and Sr isotopic shift.

Igneous plagioclase contains 115-230 ppm Sr, with up to 70 ppm variation within individual samples (Figure 2.7) (Appendix D.2). Average Sr contents for individual samples are negatively correlated with average anorthite contents and bulk rock Mg#, indicating that igneous plagioclase Sr contents increase with magmatic differentiation. Secondary plagioclase contains 66-177 ppm Sr, with <50 ppm variation within individual samples (Figure 2.7). Secondary plagioclase with more albitic and anorthitic compositions than igneous plagioclase in the same sample has lower or similar Sr contents, respectively (Figure 2.7). This means that hydrothermally altered plagioclase has similar or Sr depleted contents with respect to magmatic plagioclase. Note that the Sr contents of secondary plagioclase with intermediate anorthite contents was not measured due to the inability of reliably imaging this phase. In summary, Sr contents are positively correlated with anorthite content in albitic plagioclase and relatively constant for intermediate to anorthitic compositions (An_{30} to An_{94}) irrespective of the origin of the plagioclase. This observation is consistent with previous studies investigating the general

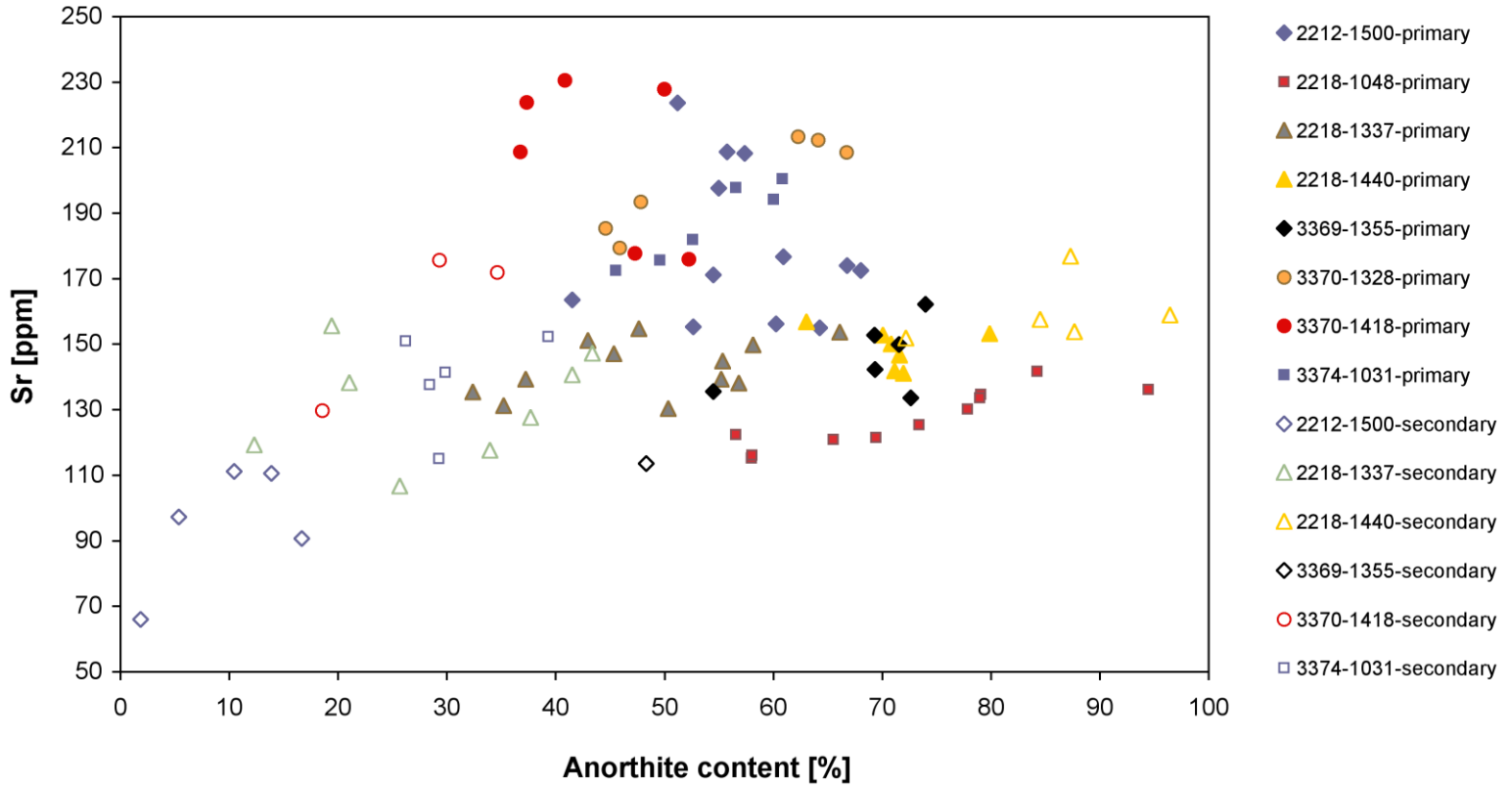

Figure 2.7: Anorthite versus Sr content in plagioclase of magmatic and hydrothermal origin. Hydrothermal plagioclase with low anorthite content generally has lower Sr contents than magmatic plagioclase in the same sample. One sample (2218-1440) with anorthitic, secondary plagioclase shows no difference in Sr content between primary and secondary plagioclase. Sr contents of magmatic plagioclase are relatively constant or decrease slightly with decreasing anorthite content within a sample. A similar trend is evident for hydrothermal plagioclase.

co-variation of Sr and anorthite contents in both igneous and hydrothermal systems (Gillis et al., 2005; Blundy and Wood, 1991; Lagache and Dujon, 1987).

Clinopyroxene and orthopyroxene have Sr contents of 4-12 ppm and <1-3 ppm, respectively (Appendix D.2). Magmatic amphibole, identified using compositional criteria outlined in Gillis et al. (2003) (primary amphibole has Nb>1, hydrothermal amphibole has Nb<1) has a wide range in Sr content, from 1.5 to >60 ppm (this study; Gillis et al., 2003). A positive correlation between Sr and Eu/Eu* (Eu*=[Sm+Gd]/2) in magmatic amphiboles indicates decreasing Sr contents with increasing differentiation, after the onset of amphibole crystallization.

Sr is compatible in apatite in basaltic rocks and has an experimentally determined partition coefficient of $D^{Sr}_{Apt} \sim 1.4$ (Watson and Green, 1981), which is comparable to plagioclase. Apatite data for gabbroic rocks recovered during Leg 147 show contents of ~160 ppm (Gillis, 1996). However, due to its accessory abundance and Sr contents that are equal to or smaller than plagioclase, apatite is unlikely to play a significant role in the Sr budget (see discussion in Section 2.4.1).

Secondary amphibole varies in Sr content (<1 to 13 ppm) both within and between samples (Figure 2.8, Appendix D.2), similar to magmatic amphibole. Ca-amphibole replacing clinopyroxene may have slightly lower to significantly higher Sr contents than its precursor, meaning clinopyroxene replacement can lead to Sr loss or gain. Low Ca-amphibole replacing orthopyroxene commonly has slightly to considerably higher Sr contents than orthopyroxene, acting to enrich the rocks in Sr. Unlike magmatic

amphibole, the Sr content of secondary amphibole does not correlate with magmatic differentiation proxies. An important finding is that the Sr content of Ca-amphibole is positively correlated with Al^{IV}, K, Na and Ti, and shows a good negative correlation with Si (Figure 2.8), suggesting that Sr uptake is temperature dependent (Spear et al., 1981).

Chlorite replacing clinopyroxene contains <1-5 ppm Sr (Appendix D.2), indicating that Sr is either immobile or depleted. Chlorite associated with myrmekitic patches has the same compositional range. Since myrmekitic intergrowths contain plagioclase, substantial loss of Sr is indicated. Talc contains ~8 ppm Sr, comparable to clinopyroxene.

Comparison of the Sr contents of the igneous minerals and their replacive hydrothermal minerals shows that the Sr budget is influenced by post-magmatic redistribution in the Hess Deep gabbroic suite. In fact, the mineral data suggest that rocks dominated by lower temperature assemblages (chlorite, actinolite, albite) loose Sr whereas rocks dominated by higher temperature assemblages (hornblende, labradorite) show no change or Sr uptake. Furthermore, gabbronorite is more likely to show Sr uptake, as the alteration assemblage of orthopyroxene is almost always enriched in Sr with respect to its precursor.

Void-filling epidote, restricted to samples recovered from zones of focused fluid flow, has Sr contents from 420 to ~1000 ppm. This explains the high bulk rock Sr content (227 ppm) of an epidote-rich sample from a fault zone in the eastern part of the field area.

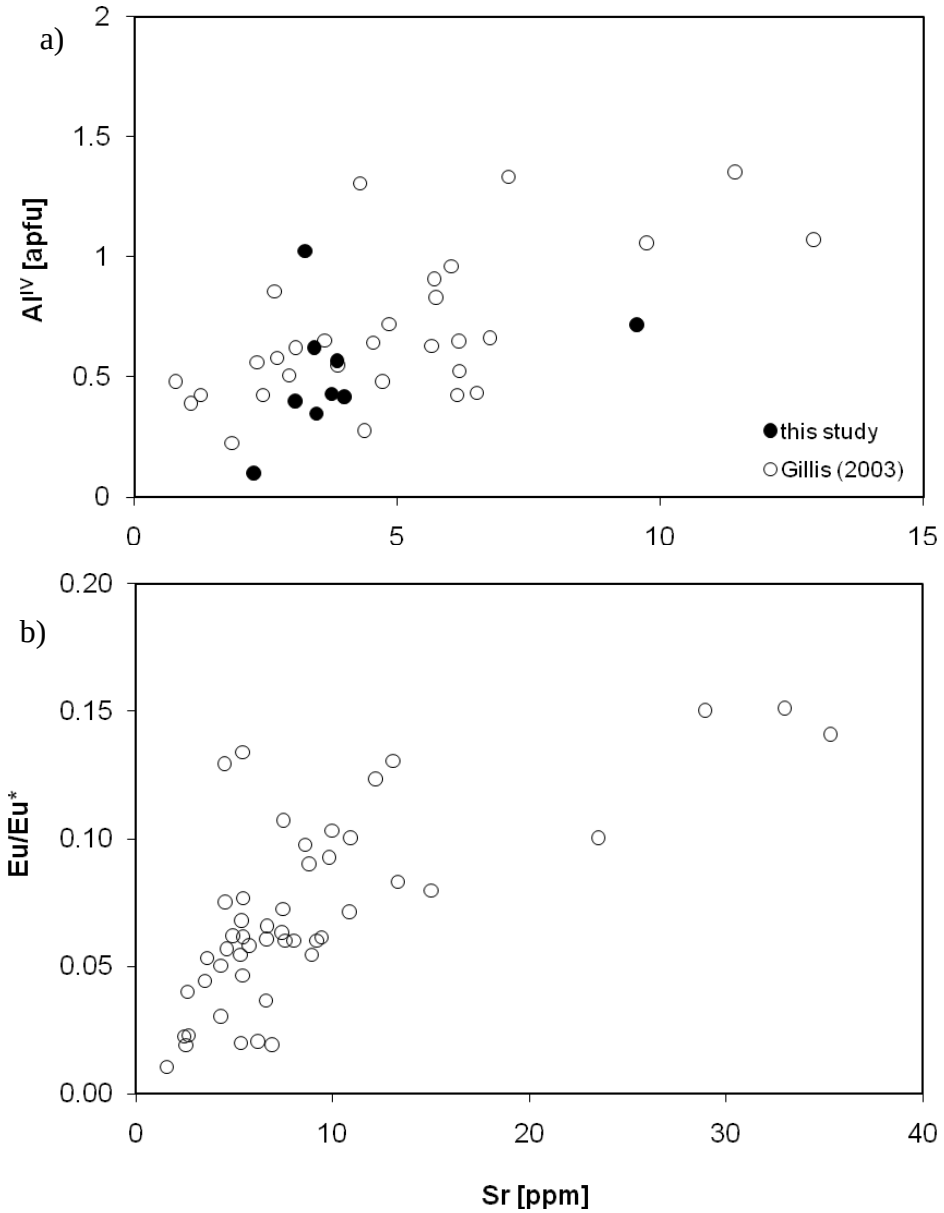

Figure 2.8: Amphibole Sr content in with a) Al^{IV} in hydrothermal amphibole (data from this study and Gillis, 2003, unpublished data) and b) Eu/Eu* in magmatic amphibole (data from Gillis, 2003, unpublished data) .

Table 1: Summary of sample characteristics

Sample #	Rock Type[1]	Depth [mbsl][2]	Depth [mbld][3]	Sr [ppm][4]	$^{87}Sr/^{86}Sr$	Error (± 2σ)	% Hydrous Minerals
2218-1404	BD	3492	1042	93	0.702827	0.000008	55.0
2212-1319	G	2996	546	99	0.702551	0.000009	14.2
2212-1409	G	2990	540	86	0.702563	0.000007	14.2
2212-1500	G	2916	466	83	0.702681	0.000008	22.8
2218-1210	G + T	3392	942	87	0.702682	0.000008	22.9[5]
2212-1338	GN	3017	567	90	0.702586	0.000007	16.8
2213-1125	GN	~3150	700	N/A	0.702445	0.000007	5.1
2218-1048	GN	3387	937	60	0.702621	0.000008	2.2
2218-1057	GN	3389	939	77	0.702519	0.000008	4.6
3369-1129	GN	3169	719	94	0.702574	0.000007	11.4
3369-1321	GN	3076	626	88	0.702569	0.000008	10.0
3369-1355	GN	3032	582	71	0.702535	0.000008	9.5
3370-1118	GN	3481	1031	85	0.702512	0.000007	0
3374-1031	GN	2997	547	98	0.702624	0.000009	14.3
3369-1042	Hbl-GN + T	3232	782	75	0.702518	0.000009	10.0[5]
2218-1337	Hbl-HF	3537	1087	82	0.702575	0.000008	15.7
2218-1440	Hbl-HF	3423	973	61	0.702562	0.000008	7.6
3370-1205	Px-HF	3362	912	99	0.702730	0.000007	0
3370-1328(c)	Px-HF	3242	792	128	0.702709	0.000008	0
3370-1328(f)	Px-HF	3242	792	86	0.702589	0.000007	0
3369-1250	Ox-G	3094	644	82	0.702553	0.000007	13.7
3370-1418	Ox-G	3096	646	106	0.702674	0.000008	20.6
2213-1053	Ox-GN	3211	761	85	0.702444	0.000008	2.7
3369-1329	T	~3060	610	68	0.703798	0.000008	N/A
3374-1057	Cat.	2899	449	226	0.703790	0.000009	N/A
Mineral Separates	***Mineral***			***average***			
2214-1127	Epidote	~2150		480	0.704292	0.000007	
3370-1408	Epidote	3106		570	0.703732	0.000006	
3369-1129	Plagioclase	3169		167	0.702461	0.000006	
3369-1355	Plagioclase	3032		146	0.702513	0.000007	

N/A = not available, - = no hydrous alteration, c = coarse, f = fine

[1] BD=basaltic dike, G=gabbro, GN=gabbronorite, Ox-=Fe-Ti-oxide, Hbl=hornblende, Px=pyroxene, T=tonalite, HF= hornfels, Cat.=cataclastite

[2] Meters below sea level

[3] Meters below the lava-dike transition

[4] See appendix for data source

[5] point counting was done for less than 600 points due to thin section geometry

2.3.4. Bulk rock $^{87}Sr/^{86}Sr$ ratios

Due to the distinct Sr isotopic signature of fresh MORB and seawater, whole rock $^{87}Sr/^{86}Sr$ can be used to quantify the degree of fluid-rock interaction in mid-ocean ridge hydrothermal systems. In order to assess the extent of isotopic exchange, it is first necessary to constrain fresh rock values. Fresh rock $^{87}Sr/^{86}Sr$ ratios of plutonic rocks from Hess Deep were constrained using acid-leached plagioclase separates from the least altered gabbronorites. The $^{87}Sr/^{86}Sr$ of plagioclase separates range from 0.70243 to 0.70251 (Table 1) (this study; Barker et al., 2008). Fresh MORB glasses from the equatorial Pacific have $^{87}Sr/^{86}Sr$ from 0.70235 to 0.70275 (average of 0.70255) (Petrological Database for the Ocean Floor; http://petdb.ldeo.columbia.edu/petdb). Based on new and published data and in order to be consistent for different samples, a range of 0.70240-0.70245 was chosen for the fresh rock $^{87}Sr/^{86}Sr$ value, considering the lowest measured bulk rock value is 0.70244 and the possibility that plagioclase separates, even though relatively fresh, likely underwent minor reaction with a hydrothermal fluid. This range is in agreement with an inferred value for gabbroic rocks recovered during Leg 147 (0.7024; Lécuyer and Gruau, 1996).

Bulk rock $^{87}Sr/^{86}Sr$ was obtained for 26 samples that are representative of the range in rock types, degree of alteration and geographic distribution. Most samples were altered by pervasive fluid flow; one sample was recovered from a focused fluid flow zone (quartz-epidote-chlorite assemblage) and another sample is strongly altered epidote-bearing tonalite with a complex alteration history. In addition, one dike with comparable

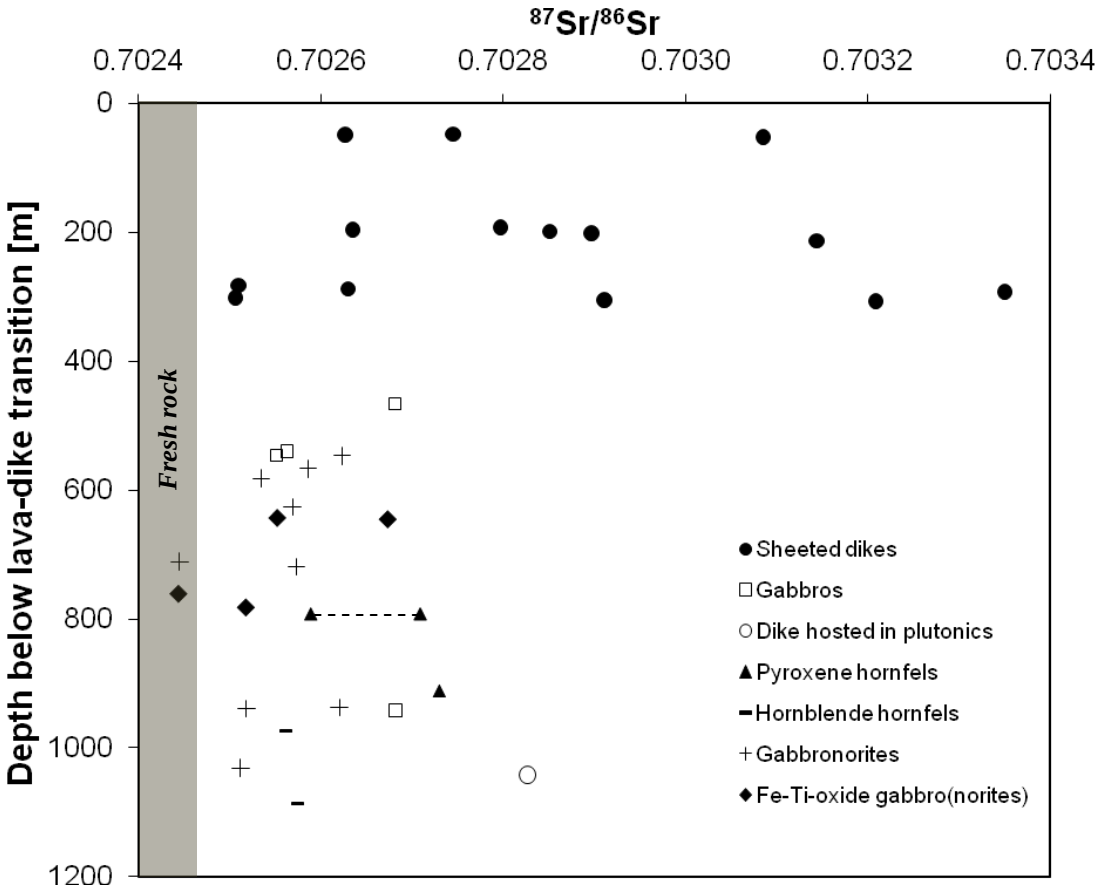

Figure 2.9: Bulk rock $^{87}Sr/^{86}Sr$ versus depth below the lava - sheeted dike transition. Dashed line joins data for the fine- and medium-grained parts of sample 3370-1328 Data for samples from the sheeted dike complex (Gillis et al., 2005) are plotted for comparison. There is no systematic trend with depth for the plutonic or sheeted dike samples.

textures and alteration to the sheeted dike complex, and four hornfelsic samples (two pyroxene and two hornblende hornfels) were analyzed. The protoliths of the analyzed hornfels are interpreted to be gabbroic rocks with one sample displaying a boundary between a hornfelsed gabbronorite and a hornfelsed dike. For the latter sample, the $^{87}Sr/^{86}Sr$ for both domains was measured.

The $^{87}Sr/^{86}Sr$ of gabbroic rocks altered by pervasive fluid flow range from 0.70244 to 0.70273 (mean = 0.70257 ± 0.00007, n=16). All except two samples are isotopically shifted towards higher than fresh values. These values are comparable to Sr isotopic ratios of plutonic rocks from ODP Holes 894G and 894F from the intrarift ridge of Hess Deep, ranging from 0.70247 to 0.70309 (average of 0.70263 ± 0.00017, n=15; outlier close to macroscopic vein not included). For plutonic rocks of both sample suites, most values fall below 0.7027 (this study; Lécuyer and Gruau, 1996). Sr isotopic values for the overlying sheeted dike complex are slightly higher than those from the plutonic section, ranging from 0.70255 to 0.70326 (mean 0.70265 ± 0.00018, n=32) (Gillis et al., 2005).

The pervasively altered gabbroic rocks show no systematic isotopic shift with depth (Figure 2.9). Bulk rock $^{87}Sr/^{86}Sr$ show a weak positive correlation with magmatic differentiation indices (e.g., Eu/Eu*, Nb, Y, but not Mg#) (Figure 2.10a). $^{87}Sr/^{86}Sr$ is weakly positively correlated to, and does not systematically change with, Sr contents of amphibole-dominated and chlorite-rich assemblages, respectively (Figure 2.10b). This highlights the effects of different alteration assemblages and temperature conditions on Sr mobility in these rocks. $^{87}Sr/^{86}Sr$ are well-correlated with the percentage of hydrous phases (Figure 2.10c). One gabbronorite sample (2218-1048) does not lie on this trend, as

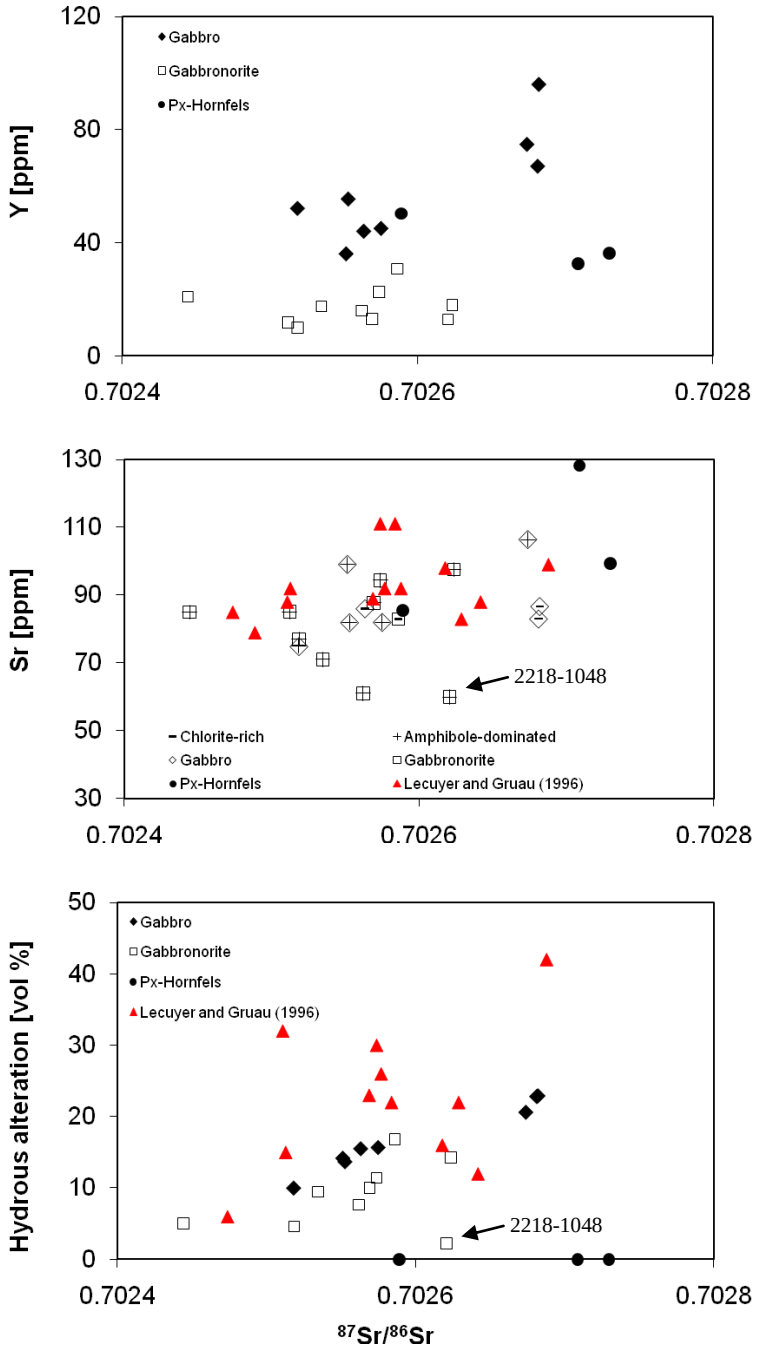

Figure 2.10: Bulk rock $^{87}Sr/^{86}Sr$ versus a) Y and b) Sr content and c) percentage of hydrous alteration. In There is a poor and no correlation between $^{87}Sr/^{86}Sr$ and Y for gabbro and gabbronorite, respectively (a). The relationship in b) is interpreted to be a result of different Sr uptake into chlorite and amphibole. The good correlation between $^{87}Sr/^{86}Sr$ and percentage of hydrous alteration suggests that hydrous alteration controls or follows Sr isotopic shift. The misfit of sample 2218-1048 in correlations b) and c) suggests that a factor other than hydrothermal alteration has shifted its $^{87}Sr/^{86}Sr$ (see section 2.4.2.4.). Data from ODP Sites 894 and 895 (Lécuyer and Gruau, 1996) are plotted in b) and c) for comparison.

it has much higher $^{87}Sr/^{86}Sr$ than indicated by its hydrous alteration percentage (<5%). As described previously, more differentiated rocks show higher hydrous alteration percentages (see Section 2.4.2.3 for discussion). However, since Sr is not well correlated with proxies for magmatic differentiation, increased Sr content with increasing alteration percentage is interpreted to be a predominantly hydrothermal feature.

The pyroxene hornfels vary in $^{87}Sr/^{86}Sr$ from 0.70251 to 0.70273. Interestingly, $^{87}Sr/^{86}Sr$ of fine- and medium-grained domains of the sample with a sharp grain size transition are 0.70259 and 0.70271, respectively. This suggests that the domain with a gabbroic protolith was more altered prior to recrystallization, perhaps due to enhanced fluid-rock interaction prior to dike intrusion in this area. Partially recrystallized hornblende hornfels have $^{87}Sr/^{86}Sr$ of 0.70256 and 0.70258. Compared to pervasively altered plutonics with preserved magmatic textures, hornfels have slightly elevated $^{87}Sr/^{86}Sr$.

Strontium was found to be depleted with increasing $^{87}Sr/^{86}Sr$ in the sheeted dikes at Hess Deep (Gillis et al., 2005). This finding, in conjunction with this study, implies different exchange mechanisms for Sr between fluids and rock in the sheeted dike complex and plutonic section. A strongly altered basaltic dike hosted in the plutonic rocks (~550 m below the base of the sheeted dikes) is slightly elevated (0.70283) with respect to the pervasively altered plutonics but falls within the range of the sheeted dike complex.

The sample from a focused fluid flow zone, as well as the strongly altered tonalite, are largely made up of hydrothermal minerals and have Sr isotopic ratios of 0.70379 and 0.70380, respectively.

Void-filling epidote separates from two samples were analyzed to constrain the $^{87}Sr/^{86}Sr$ of the hydrothermal fluid reacting with rocks at different levels within the crust. One sample was recovered from a fault gouge recovered close to the lava–sheeted dike transition in the sheeted dike complex. The second sample comes from zone of focused fluid flow hosted in the plutonic section within 200 m of the base of the sheeted dike complex. Epidote $^{87}Sr/^{86}Sr$ values are 0.70429 and 0.70373 from the sheeted dike complex and the plutonics, respectively. These results suggest that depth influences the isotopic shift and that the fluid penetrating the plutonic section is isotopically more rock-dominated.

2.4. Discussion

The results presented in the previous section document the distribution of Sr between igneous and hydrothermal phases and the association of metamorphic assemblages, degree of alteration and alteration conditions. In the following section, the controls on Sr distribution and mechanisms of exchange between igneous and metamorphic phases will be investigated. Sr behaviour is then linked to $^{87}Sr/^{86}Sr$ systematics and its role as a geochemical proxy for fluid-rock interaction is assessed. Lastly, the temporal and spatial characteristics of hydrothermal circulation and their implications for magmatic accretion of the lower oceanic crust are discussed.

2.4.1. Strontium mass balance

Interpretation of bulk rock $^{87}Sr/^{86}Sr$ requires knowledge of the distribution of Sr in igneous and hydrothermal minerals. The Sr contents of igneous and hydrothermal minerals are relatively consistent between samples suggesting that Sr has a consistent partitioning behaviour under igneous and hydrothermal conditions (Table 2). Bulk rock Sr values were calculated for six samples representative of rock type, percentage of hydrous alteration and regional distribution using the mineral modes and average mineral compositions for each sample (Table 2). All calculated samples reproduced the measured bulk rock Sr content within 20%, three samples reproduced it within 10%. There is no correlation between abundance of Fe-Ti oxides and the deviation between calculated and measured bulk rock Sr content, suggesting that Sr resides in the major minerals and bulk

Table 2: Strontium mass balance derived from modal abundances and Sr contents for magmatic and hydrothermal minerals.

Sample #	**Magmatic and hydrothermal minerals ± 1σ [vol. %][6]** *average Sr content ± 1σ [ppm]*								**Bulk rock Sr [ppm]**		
	Plg	Cpx	Opx	Hbl	Ca-Amp	low Ca-Amp	Chl	Tlc	Calculated	Measured	Difference [%]
2212-1338	52±0.30[7] *185±14.9*	22±0.70 *6.6±0.83*	3±4.74 *0.14±0.08*		2 *N/A*	8 *11.4*	7 *1.7±2.3*		99±8.5	90	10
2212-1409	38±0.40 *174±6.3*	37±0.41 *7.8±0.83*			10 *12.4*		5 *1.2±1.0*		70±4.0	86	18
2218-1048	36±0.42 *134±5.6*	50±0.30 *7.3±3.4*	12±1.2 *1.3±0..45*		2 *N/A*				52±2.9	60	13
2218-1440	26±0.58 *172±13.6*	1.5 *6.4*	9±1.8 *1.1±1.1*	54±0.28 *25.5±24.6*	1 *N/A*			6±2.59 *7.7*	54±8.8	61	11
3369-1321	52±0.29 *162±4.8*	31±0.49 *6.3±0.38*	6±2.4 *0.46*		9±1.6 *4.6±2.8*	1 *N/A*			87±3.9	88	1
3374-1031	44±0.34 *217±0.95*	34±0.44 *7.5±1.3*	4±3.9 *0.41±0.43*		10±1.5 *3.4±0.76*	1 *3.0±1.5*			100±4.2	98	2

[6] Abbreviations: Plg=plagioclase, Cpx=clinopyroxene, Opx=orthopyroxene, Hbl=primary hornblende, Amp=secondary amphibole, Chl=chlorite, Tlc=talc, N/A = not available

[7] Quantification of modal uncertainties based on Bayly (1965)

rock Sr values are not significantly impacted by the abundance of Fe-Ti-oxides and accessory phases.

General uncertainties associated with the mass balance calculations of all samples are as follows. First, the variability of mineral modes, plagioclase in particular, on a hand sample versus thin section scale may have a major effect on mass balance calculations. For example, plagioclase abundance may vary by as much as 20% in thin sections from the same sample. Second, the abundance of secondary and primary plagioclase is not accurately known (see Section 2.3.1.2.). However, it is not expected that this uncertainty impacts calculated Sr values significantly for samples with intermediate to calcic secondary plagioclase. Similarly, samples with albitic plagioclase are unlikely to be shifted significantly as albite generally makes up <5% of the plagioclase. The sample with the greatest deviation between measured and calculated Sr content has >5% chlorite which was found to be associated with albitic plagioclase. Thus, in this sample, the uncertainty of albitization on the Sr budget may play a more important role. Third, amphibole may have a wide range in Sr content on a sample scale. Samples with higher modal abundances of amphibole are therefore subject to a larger uncertainty due to the use of average values.

2.4.2. Controls on Sr mobility and Sr isotopic exchange

2.4.2.1. Replacement mechanisms

The nature of Sr exchange and transport of the Sr isotopic signal between primary and secondary minerals is influenced by the mechanisms that control primary mineral

replacement. Two primary mechanisms are known to promote chemical exchange during fluid-rock interactions, namely diffusion and dissolution–precipitation. If Sr diffusion is a viable mechanism, its role in plagioclase will control a potential shift in bulk rock Sr isotopic composition, since diffusion rates in other primary phases is too slow (Sneeringer et al., 1984) and Sr content in plagioclase makes up >90% of the bulk rock Sr content. Both, diffusion rates (Giletti and Casserly, 1994) and partition coefficients controlling equilibrium conditions between plagioclase and a hydrothermal fluid (Blundy and Wood, 1991) are dependent on the anorthite content of plagioclase. Using

$$\frac{6}{\pi^2} \cdot \sum \frac{1}{n^2} e^{-n^2 \pi^2 \frac{Dt}{a^2}} \qquad (1)$$

(with D = diffusion coefficient, t = time, and a = grain radius)

to model diffusive fluxes in a sphere (Albarède, 1995) Sr diffusion in plagioclase was modeled assuming a of 500 µm radius and an anorthite content of 0.5. To model the maximum diffusive effects on $^{87}Sr/^{86}Sr$ shift, ^{87}Sr and ^{86}Sr were treated as separate species with a fresh plagioclase $^{87}Sr/^{86}Sr$ of 0.7024, a fluid $^{87}Sr/^{86}Sr$ of 0.705, a plagioclase Sr content of 160 ppm and a fluid Sr content of 15 ppm. The fluid equilibrates with plagioclase adjacent to the fluid flow path (e.g., the rim for grain boundary flow) and creates a concentration gradient within the grain along which diffusive flux occurs. Early fluid ingress along microcracks is assumed to commence under semi-brittle conditions at 700ºC to 800ºC whereas the duration of fluid flow at amphibolite facies conditions is less well constrained. For instance, the sealing of high-

temperature fluid flow paths was estimated to lie between <100 and 6000 years (e.g., Manning et al., 1996; Coogan et al., 2007). For this model, diffusive exchange and isotopic effects, hydrothermal conditions of 750ºC and 1000 years of fluid flow were used as a first approximation. Variable fluxes of ^{87}Sr and ^{86}Sr due to different $^{87}Sr/^{86}Sr$ compositions in fluid and mineral leads to a $^{87}Sr/^{86}Sr$ shift from 0.70240 to 0.70255. Compared to the Sr isotopic compositions observed in the analyzed samples, this shift is significant. It should be noted, however, that this shift is a maximum value due to the following reasons. First, Sr content and $^{87}Sr/^{86}Sr$ of the fluid are likely at the upper end of the reasonable range (for discussion see Section 2.4.3.1.). Second, this model assumes 1000 years of fluid flow under constant temperatures. Previous studies modelling the cooling rates within the upper plutonics found that this is not a reasonable assumption (cooling rates 0.1-1ºC/year) (e.g., Coogan et al., 2002b; Maclennan et al., 2005). Lastly, equation 1 assumes an infinite Sr source with constant concentration and therefore neglecting Sr (isotopic) equilibration between plagioclase and fluid. Considering the low porosity of plutonic rocks, this scenario is unrealistic and Sr equilibration is likely to occur, leading to decreasing concentration gradients and diffusive fluxes with time. A model with less extreme input parameters (Sr_{fluid}=11 ppm; $^{87}Sr/^{86}Sr_{fluid}$=0.704; fluid flow: 100 years at 750ºC + 500 years at 700ºC) yields a reduced isotopic shift to 0.70244 still not considering the equilibration of Sr concentration. This value is within the uncertainty of the inferred fresh rock $^{87}Sr/^{86}Sr$ and thus, diffusive processes are interpreted to be negligible for plutonic rocks altered during hydrothermal alteration.

In contrast to diffusion, during dissolution-precipitation replacement, the crystal structure is completely dissolved and reprecipitated along a sharp fluid-solid interface (e.g., Hoevelmann et al., 2010). An experimental study investigating plagioclase dissolution-precipitation by secondary albite under hydrothermal conditions at 600ºC has shown that the O isotopic composition of an isotopically spiked fluid was adopted by the secondary plagioclase, suggesting complete or near-complete isotopic exchange (Hoevelmann et al., 2010). In the same study, it was also found that albitization leads to general depletion of trace elements in plagioclase including Sr.

These findings, along with the good correlation of hydrous alteration percentage and $^{87}Sr/^{86}Sr$, suggest that dissolution-precipitation dominates the replacive mechanism and Sr diffusion will henceforth not be considered.

2.4.2.2. Alteration conditions

The extent and nature of chemical exchange during fluid-rock interaction in the gabbroic rocks are controlled by the secondary mineral assemblages and metamorphic conditions, specifically alteration temperature.

The impact of metamorphic conditions on Sr isotopic exchange is considered first for samples with the simplest alteration history (i.e., with limited retrograde alteration). Consider a chlorite-rich rock that has the same $^{87}Sr/^{86}Sr$ as an amphibole-dominated rock assuming the mineral assemblages reflect peak temperatures of alteration. Chlorite-rich rocks formed under greenshist facies conditions have lost Sr to the fluid due to low Sr contents in this phase relative to its precursor. The amphibole-dominated assemblage

likely reacted under higher temperatures and has taken up more Sr from the fluid due to the relative enrichment of Sr in amphibole versus chlorite. Thus, even though $^{87}Sr/^{86}Sr$ suggests similar extents of fluid-rock interaction, the chlorite-rich samples likely interacted with a larger amount of fluid than the amphibole-dominated sample due to the loss of Sr to the fluid. This effect would be even more pronounced if an assemblage is chlorite-dominated and contains albitic secondary plagioclase and/or the higher temperature, amphibole-dominated assemblage is made up of secondary hornblende that took up Sr with respect to its precursor (Figure 2.8). Additionally, it should be noted that the replacement of igneous plagioclase by intermediate to anorthitic secondary plagioclase may not affect the bulk Sr content but would shift the Sr isotopic value towards fluid values. Hence, the positive correlations of $^{87}Sr/^{86}Sr$ with Sr content and the percentage of hydrous alteration likely reflect the combined effects of Sr uptake into secondary plagioclase and hydrous minerals.

The role of retrograde metamorphism and its impact on Sr distribution as the crust moves further off-axis is a factor that must also be considered. In the western part of the field area, amphibole with high Al^{IV} contents coexist with chlorite patches on a sample scale suggesting that these rocks underwent a larger alteration temperature interval. Thus, high incipient alteration temperatures leading to Sr uptake by the rock could be overprinted by lower temperature assemblages leading to Sr loss. These findings indicate that, where both amphibolite- and greenshist facies assemblages are present, the Sr distribution cannot be solely attributed to peak temperature alteration, but retrograde

alteration (of potentially longer time intervals) may significantly redistribute Sr in the altered rocks.

2.4.2.3. Textural controls

Magmatic differentiation indicators (e.g., CaO, Y) are positively correlated with percentage of hydrous alteration (Figure 2.3) and, to a lesser degree, with Sr isotopic ratios (Figure 2.10). This phenomenon may be explained by the generally finer grain sizes of gabbro with respect to gabbronorites, providing more pathways for grain boundary flow. Furthermore, gabbronorite has a higher average modal abundance of plagioclase, potentially biasing point counting results towards higher percentages of hydrous alteration for more evolved rocks with more mafic phases that are replaced by hydrous phases.

2.4.2.4. Assimilation

Assimilation of hydrothermally altered rocks into the AMC is a common process at intermediate- to fast-spreading ridges (e.g., Michael and Schilling, 1989) and could potentially shift the $^{87}Sr/^{86}Sr$ of the mantle-derived melt. Partially molten and recrystallized xenoliths at various depths in plutonic sections of ophiolites provided the first evidence that stoping of roof material into the AMC is an important process (e.g., Stakes et al., 1984; Gillis and Roberts, 1999). The impact of this process on melt chemistry is seen in the overenrichment of Cl in basalts from fast-spreading ridges relative to slow spreading ridges, interpreted to be the result of a assimilation of material

with a seawater-component (e.g., Michael and Schilling, 1989; Coogan et al., 2003). Significant overenrichment of Cl and B, as well as B isotopic signature, in magmatic amphiboles scattered throughout the upper plutonic section at Hess Deep lead to the conclusion that assimilation of hydrothermally altered dikes and pore fluids also affects the composition of plutonic rocks in this setting (Gillis et al., 2003). Thus, if a significant mass of hydrothermally altered roof material stopes into the AMC, the melt would be shifted towards higher $^{87}Sr/^{86}Sr$ values.

The elevated $^{87}Sr/^{86}Sr$ (0.70262) in a sample (2218-1048) with a very low percentage of hydrous alteration (<5%) (Figure 2.10) suggests that a mechanism other than hydrous alteration must be responsible the Sr isotopic shift. The presence of secondary plagioclase causing this shift cannot be ruled out but seems unlikely, since no secondary plagioclase of extreme anorthite compositions was found in this sample and the decoupling of hydrous alteration from anhydrous plagioclase alteration is not indicated in other samples.

To quantify the impact of assimilation on $^{87}Sr/^{86}Sr$, the amount of assimilated material needs to be known. Coogan et al. (2003) used Cl/Ti in basalts as a geochemical tracer to model the extent of assimilation at fast-spreading ridges. Ti was chosen as a reference species to Cl due to its relatively well-known behaviour in magmatic systems and its immobility during hydrothermal alteration. Furthermore, this model assumes a steady-state system with periodical eruption and replenishment events accompanied by crystallization and assimilation. These authors estimated that ~20% of the total mass of the oceanic crust are recycled in the AMC after hydrothermal alteration. Assuming a

contaminant $^{87}Sr/^{86}Sr$ of 0.70265 (average altered dike $^{87}Sr/^{86}Sr$; Gillis et al., 2005) and a mantle-derived melt $^{87}Sr/^{86}Sr$ of 0.7024, recycling of 20% (Coogan et al., 2003) of altered oceanic crust would lead to an apparent fresh rock $^{87}Sr/^{86}Sr$ of 0.70245, if the contaminant is homogeneously mixed in the AMC. In order to elevate the fresh rock $^{87}Sr/^{86}Sr$ to ~0.7026, assimilation of >80% hydrothermally altered material would be required. In contrast, one sample that showed Cl-overenrichment in primary amphibole (3369-1042) (Gillis et al., 2003) has a relatively low $^{87}Sr/^{86}Sr$ of 0.70251 with ~10% hydrous alteration suggesting that assimilation of hydrothermally altered material does not significantly shift bulk rock $^{87}Sr/^{86}Sr$. A number of different factors may be responsible for these contrasting patterns. First, different partitioning behaviour of Sr and Cl (e.g., Coogan et al., 2003; Blundy and Wood, 1991) into secondary phases affects the chemical signature of assimilation differently. Cl is incompatible in magmatic systems and thus will be enriched in more evolved rocks. Since primary amphibole also generally occurs in the more evolved spectrum of plutonic rocks, the effects of assimilation on Cl content will be more pronounced in amphibole-bearing rocks, whereas fluid-derived Sr will be taken up in all rock types since it is compatible in plagioclase, which crystallizes throughout the entire fractionation process. Second, assimilation may be temporally and spatially variable. If assimilation is episodic, which is conceivable as stoping is likely enhanced during upwards migration of a magma chamber (e.g., Coogan et al., 2003; Gillis, 2008), the $^{87}Sr/^{86}Sr$ shift in the AMC due to assimilation may vary temporally. Additionally, field relations from the Oman ophiolites show that xenoliths with granoblastic textures are often surrounded by coarse-grained gabbro containing

amphiboles that record temperatures of ~1020ºC, which is higher than hydrous solidus of gabbro (France et al., 2009). This indicates the release of water through dehydration and shows that effects of assimilation may be locally restricted within the magma chamber, likely dependent on the viscosity and mixing characteristics of the melt.

In conclusion, even though primary amphibole in some samples may show clear signs of assimilation of a rock altered by hydrothermal fluids, $^{87}Sr/^{86}Sr$ may not be noticeably shifted in these samples. However, $^{87}Sr/^{86}Sr$ may be strongly shifted by assimilation of altered roof material due to either local dehydration effects, or temporally enhanced assimilation events, potentially explaining the unusually high $^{87}Sr/^{86}Sr$ in sample 2218-1048. However, contamination during the preparation of the bulk rock powder by low-temperature alteration assemblages, known to have strongly elevated $^{87}Sr/^{86}Sr$, cannot be ruled out but is unlikely since elevated Cs or Rb contents, indicating low-temperature alteration assemblages, were not observed in this sample.

2.4.3. Quantification of fluid-rock interaction

Sr isotopic compositions of hydrothermally altered samples can be used to quantify the amount of fluid a rock has interacted with during hydrothermal alteration. Quantification of fluid/rock ratios (F/R) in the oceanic crust is useful to gain insight into the geometry of the hydrothermal system and the amount of heat removed from the crust advectively. Fluid/rock ratios describe the relative masses of hydrothermal fluid and rock that have reacted (e.g., Albarède et al., 1981) and are calculated using:

$$\frac{(^{87}Sr/^{86}Sr)_{AR} - (^{87}Sr/^{86}Sr)_{FR}}{(^{87}Sr/^{86}Sr)_{HF} - (^{87}Sr/^{86}Sr)_{AF}} \cdot \frac{C_{FR}^{Sr}}{C_{HF}^{Sr}} = \frac{F}{R} \qquad (2)$$

with AR=altered rock, FR=fresh rock, HF=hydrothermal fluid, AF= altered fluid, and C^{Sr}=strontium concentration.

There are two uncertainties associated with this mass balance equation. First, it ignores Sr mobility (i.e., 1:1 exchange between rock and fluid is assumed). Thus, because some sheeted dike samples have lost Sr to the fluid and some plutonic samples have taken up Sr from the fluid, calculated fluid/rock ratios would be under- and overestimates, respectively. Second, it assumes no change of fluid Sr and $^{87}Sr/^{86}Sr$ composition as it penetrates to deeper levels. Thus, in order to obtain representative results, input parameters need to be adapted to the Sr behaviour during fluid-rock reaction found in this and other studies.

2.4.3.1. Estimation of input parameters for fluid/rock calculations

Measured and constrained parameters used in equation (1) are $^{87}Sr/^{86}Sr$ of altered and fresh (0.7024, see Section 2.3.4) rocks, respectively. The remaining parameters are largely unknown and must be constrained indirectly.

In the studied plutonic rocks, bulk rock Sr contents have a large range (60-137 ppm), primarily due to magmatic differentiation resulting in variable plagioclase abundances and compositions. To account for this range, the Sr content of each sample is used for the fresh rock value (C_{FR}^{Sr}) as the extent of Sr mobility (Section 2.4.2.) is likely much smaller than the magmatic variability.

Estimation of fluid Sr contents and $^{87}Sr/^{86}Sr$ entering the gabbroic section is less straightforward due to the lack of sampling of deep hydrothermal fluids. Comparison of seawater values with hydrothermal fluids venting on the seafloor show that crustal fluids are shifted towards lower $^{87}Sr/^{86}Sr$, with some changes in Sr concentration (discussed below). Both $^{87}Sr/^{86}Sr$ and Sr systematics are influenced by the reaction pathway of the fluids and processes active in different parts of the hydrothermal system, including anhydrite precipitation, phase separation and fluid mixing. Two end-member models for Sr content and $^{87}Sr/^{86}Sr$ of deep hydrothermal fluids are considered that invoke different reaction paths.

Model 1 (hereinafter referred to as the conventional model) is based on the conventional assumption that most of the fluid-altering reactions occur in the recharge limb of the hydrothermal system, with little or no reactions occurring as fluids rise to the seafloor from the hydrothermal root zone (e.g., Alt, 1995). The fluid entering the top of the sheeted dike complex would be very similar to seawater, with 8 ppm Sr and $^{87}Sr/^{86}Sr$ of 0.7086 (assumes minor isotopic exchange in the volcanic sequence). The first reaction that bears on the Sr content of the recharging fluid is the precipitation of anhydrite at temperatures between ~150 and 250ºC (e.g., Bischoff and Seyfried, 1978) during relatively shallow heating of downwelling fluids (e.g., Sleep, 1991; Barker et al., 2010a). Models based on Sr and S isotopic data for the sheeted dike complex at Pito Deep predict that 90% of seawater sulphate precipitates as anhydrite in recharge zones (Barker et al., 2010a). Assuming a partition coefficient of 180 (Shikazono and Holland, 1983), ~ 3 ppm Sr would be removed from the fluid at this early stage. Subsequent fluid-rock interaction

leads to extensive (~10-20%, ~10 ppm) Sr leaching (Gillis et al., 2005; Barker et al., 2008), thus increasing hydrothermal fluids Sr contents to ~15 ppm by the time it enters the top of the plutonic sequence. This value is very close to the average vent fluid value of 12 ppm (see Barker et al., 2008 for data compilation).

In this model, the $^{87}Sr/^{86}Sr$ of the fluid entering the plutonic section will be relatively rock-dominated and is assumed to be 0.7045. The Sr-isotopic composition of the fluid exiting the plutonic sequence may be constrained from vent fluids compositions. The $^{87}Sr/^{86}Sr$ of Mg-normalized (i.e., corrected to zero-Mg) vent fluids fall between 0.7030 and 0.7040, with an average of 0.7038 (see data compilation in Barker et al., 2008). To allow for mixing of deep-seated fluids with more seawater-like fluids at shallower depths (e.g. Barker et al., 2010b), a fluid $^{87}Sr/^{86}Sr$ of 0.7034 was chosen. Since in this model, most of the fluid-rock interaction occurred in the downwelling limb of the hydrothermal system the fluid $^{87}Sr/^{86}Sr$ entering the plutonic section is predicted to be 0.7045.

In **model 2** (hereinafter referred to as the alternative model), a different reaction path is assumed with extensive fluid-rock interaction and heating largely occurring in the lower third of the recharge zone and in the discharge zone (e.g., Coogan, 2008). Similar to the conventional model, after early loss of ~3 ppm Sr by precipitation of anhydrite within the shallow recharge zone, fluid-rock interaction would release Sr to the fluids. As these reactions are limited to the lower third of the sheeted dike complex, it is assumed that 3 ppm (30% of total leaching in the sheeted dike complex) is added to the fluid. Thus, by the time the fluids enter the plutonics they would have a concentration of 8 ppm. The $^{87}Sr/^{86}Sr$ of the fluid entering the plutonics in this must be closer to seawater

composition than in model 1. Fitting the Hess Deep sheeted dike data, a linear kinetic model assuming reactions occurring during recharge and discharge (Barker et al., 2008), predicts that fluids at the base of the sheeted dike complex are 0.7050. Assuming that fluid-rock interaction during recharge is minimal for the most part of the recharge zone (Coogan, 2008), the fluid $^{87}Sr/^{86}Sr$ entering the gabbroic section is predicted to be 0.7060 in this model. In order to allow for significant fluid-rock reaction during upflow before mixing with shallow fluids and to be consistent with vent fluid chemistry, the $^{87}Sr/^{86}Sr$ of the fluid exiting the plutonic section is set to 0.7040.

It should be noted that both models predict a constant Sr concentration of the fluid and rock during alteration of the plutonic section. This study shows that this likely a false assumption, however, due to the lack of quantification of Sr exchange, the consideration of Sr fluxes may lead to even higher uncertainties in the calculated fluid/rock ratios.

2.4.3.2. Fluid/rock ratios

The average fluid/rock ratios are 1.0 for both models, with a range of 0.2-1.8 and 0.2-2.5 for the conventional and alternative model, respectively. As would be expected based on $^{87}Sr/^{86}Sr$ alone, fluid/rock ratios do not vary with depth. This suggests that consideration of bulk rock Sr (see equation 2) does not noticeably affect most Sr isotopic relationships. Lateral variation of fluid/rock ratios are, however, slightly more pronounced than lateral $^{87}Sr/^{86}Sr$ variation. This relationship shows clearly elevated fluid/rock ratios in the central part of the study area (around the longitude of dive 3370) where the pyroxene hornfels are clustered.

The input parameters predicting fluid composition entering and exiting the plutonic section are not well constrained, causing a large uncertainty in calculated fluid/rock ratios. For example, using input parameters of $(^{87}Sr/^{86}Sr)_{IF}$ = 0.7040, $(^{87}Sr/^{86}Sr)_{AF}$ = 0.7034 and C^{Sr}_{HF}= 8 ppm, a fluid composition that likely is an end-member but cannot be ruled out, the fluid/rock ratio changes to 3.4, considerably higher than predicted by the described models. Due to the sensitivity of fluid/rock ratios calculations on the fluid composition at depth, a more reasonable approach may be to treat the sheeted dike complex and the plutonic section as one hydrothermal system. This would lower the uncertainty of the calculated fluid/rock ratios as the composition of a fluid entering and exiting the sheeted dike complex is better constrained. Using the average (weighted by lithology thickness) and $(^{87}Sr/^{86}Sr)_{IF}$ = 0.7086, $(^{87}Sr/^{86}Sr)_{AF}$ = 0.7038 and C^{Sr}_{HF}= 8 ppm, the total fluid/rock ratio of this combined hydrothermal system is 0.5. Given a fluid/rock ratio of 0.77 calculated for the sheeted dike complex at Hess Deep (Barker et al., 2008), the fluid/rock ratio in the plutonic section is likely <0.5.

2.4.4. Regional characteristics of the base of the hydrothermal system

Hydrothermal systems at fast-spreading MORs are responsible for heat removal from one or more steady-state melt lenses leading to the accretion of the lower oceanic crust (e.g., Phipps Morgan and Chen, 1993). To date, it is known that the base of the hydrothermal system in these settings penetrates the plutonic section to considerable depths (e.g., Lécuyer and Gruau, 1996), however, the timing and nature of deep-seated hydrothermal systems remain relatively poorly-constrained. A major unknown with

respect to the nature of heat removal from the lower oceanic crust is the relative role of pervasive versus focussed fluid flow. Incipient stages of fluid flow in the plutonic section occur pervasively along grain boundaries and microfractures (this study, Manning et al., 1996, 2000) and millimeter-wide macroscopic fractures (e.g., Coogan et al., 2002a, Coogan et al., 2007). The time and temperature interval, as well as the near-axis depth of fluid flow, controls the efficiency of heat removal. Thermal modelling, as well as the composition of hydrothermal minerals, suggest that sealing of early high-temperature veins occurs over relatively small time and temperature spans, probably well within 6000 years (Manning et al., 1996; Coogan et al., 2007; Phipps Morgan and Chen, 1993). The depth of hydrothermal circulation along the periphery of the AMC and the underlying low-velocity zone additionally controls the cooling of the young lithosphere and will have implications on the nature of lower crustal accretion (e.g., Maclennan et al., 2005; Cherkaoui et al, 2003; Bosch et al., 2004; Coogan et al., 2003b). To date, the slope of the rigidus with increasing depth is not well constrained. Geochemical and thermal modelling addressing cooling rates at different levels of the lower oceanic crust showed that cooling rates decrease with increasing depth within the plutonic section, resembling a thermal pattern predicted by conductive cooling models (Coogan et al., 2003b; Maclennan et al., 2005; Cherkaoui et al., 2003). This could be either a result of negligible hydrothermal cooling with increasing depth or a constant advective enhancement factor superimposed on conductive cooling (Coogan et al., 2003b). Interestingly, in the plutonic section of Hess Deep, plagioclase-amphibole thermometry shows no systematic temperature variation with depth in the upper gabbros, suggesting that incipient fluid ingress is

dependent on a thermally-controlled cracking front penetrating downward into the plutonic section (Coogan et al., 2002a)

As spreading moves the oceanic crust away from the ridge axis plutonic rocks become brittle and fault zones propagate into the plutonic section (Figure 2.11), possibly associated with the formation of abyssal hills that is commonly initiated ~2 km from the ridge axis (e.g., Coogan et al., 2006). Even though the advance of a chemical alteration front may be restricted to a few meters into the wall rock adjacent to focused fluid flow zones, enhanced lateral conduction of heat could make these zones a more efficient heat removal mechanism than pervasive fluid flow once the system exceeds a certain distance from the ridge axis (e.g., Coogan et al., 2006; Hayman and Karson, 2007).

Gabbroic rocks recovered from Hess Deep allow insight into the hydrothermal system within the upper plutonic section and, when combined with findings from ophiolites and modern mid-ocean ridge crust, provide a better understanding of the temporal alteration characteristics in the shallow plutonics. The transition between the sheeted dike complex and upper plutonics is thought to be an interface of heat exchange between the hydrothermal system and the magmatic heat source, commonly called a conductive boundary layer (CBL) (e.g., Gillis and Roberts, 1999; Coogan et al., 2003a). The CBL is commonly represented by thin aureoles (30-45 m) of hornfels exchanging heat between the magmatic heat source and the hydrothermal system conductively, and thus controlling the rate efficiency of heat removal on-axis (e.g., Gillis, 2008). In previous hydrothermal models, the CBL was treated to be situated at a fixed depth at the base of the sheeted dike complex (e.g., Lowell and Germanovich, 1994, Wilcock and Delaney, 1996). However,

lithological relationships observed in the Oman ophiolite suggest the downward movement of a melt lens leading to dike intrusions within the plutonic section (France et al., 2009). In order to maintain high temperatures of alteration observed in microfractures of plutonic rocks (this study, Manning et al., 1996, Coogan et al., 2002a), the base of hydrothermal system will also migrate downward along a cracking front.

Hornfels were formed under temperatures of 700-1000ºC and was interpreted to represent recrystallized rock that was previously hydrated by hydrothermal alteration (Gillis, 2008). The vertical distribution of hornfels within the gabbro-sheeted dike transition of different locations suggest the upward migration of the AMC after the hydrothermal-magmatic interface was forced to deeper levels (Gillis, 2008). Note that the vertical distribution could, at least partly, also be a result of subsidence of hornfelsed xenoliths within the AMC (e.g., France et al., 2009).

The assimilation of hydrated material was inferred from the Cl-overenrichment found in basalts from intermediate- to fast-spreading ridges, interpreted to represent the geochemical signature of a seawater-component (Michael and Schilling, 1989; Coogan et al., 2003; Gillis et al., 2003). Thus, incipient hydrothermal fluid ingress must occur on-axis and is likely facilitated by permeability created through the combined effects of downward penetration of a cracking front (e.g., Lister, 1980), dike injection (e.g., Lowell and Germanovich, 1994) and pressure-induced cracking caused by magmatic volatiles (e.g., Gillis and Roberts, 1999). Furthermore, assimilation of hydrothermally altered xenoliths provides evidence for upward migration of the AMC (e.g., Coogan et al., 2003). Elevated Cl contents in primary amphiboles at different depths in the Hess Deep upper

plutonics suggest that assimilation of altered material also plays a role in this setting (Gillis et al., 2003).

The field area of this study represents a geological record of ~60,000 years (Karson et al., 2002) and allows the investigation of temporal variability of hydrothermal characteristics. An isotopic study investigating diffusion profiles adjacent to a 1-mm-wide amphibole vein formed at ~720ºC even suggested the sealing of fluid pathways within 100 years (Coogan et al., 2007). The lateral distribution of chlorite-rich and amphibole-dominated secondary assemblages is indicative of variable thermal conditions with time. However, similar maximum Al^{IV} in hydrothermal amphiboles throughout the field area suggests fluid ingress under similar temperatures. This means that either hydrothermal circulation in the youngest rocks of the field area (western part) underwent prolonged fluid flow further off-axis, or this area was subject to higher cooling rates. The latter may be explained by two scenarios. First, during hydrothermal cooling of the western part of the field area, magma supply was low, leading to freezing of the roof of the magma chamber and relatively quick downward migration of the cracking front (e.g., France et al., 2009). Efficient cooling near the base of the sheeted dike complex could then be responsible for a temperature drop of ~400ºC and the replacement of incipient high-temperature amphibole by chlorite as the dominant hydrothermal phase. By the time rocks in the central part of the field area were formed, magma supply may have been more steady-state leading to high-temperature overprint (e.g. caused by repeated diking events) until pervasive fluid flow pathways were sealed. Second, rocks from the western part of the field area are gabbros and gabbronorites, whereas in the central region Fe-Ti

oxide hornblende gabbros and underlying gabbronorites represent the dominant lithologies. Different rock types may have variable rock mechanics, which will affect the respective brittle-ductile transitions and the propagation of cracks (e.g., Hirth et al., 1998). If chlorite-rich gabbros were weaker and failed earlier and/or more strongly, the increased permeability would result in higher fluid/rock ratios, and hence, higher cooling rates at the ridge axis. Temporal variability in recorded thermal regimes was also found in the sheeted dike complex at Hess Deep, however no lateral relation with respect to temperatures between these rocks and the plutonic section was found (this study, Gillis et al., 2001).

At the Hess Deep Rift, the transitional region of the sheeted dike complex and the plutonic section shows characteristics indicative of the described vertical migration of the AMC. The presence of hornfels at various depth levels with elevated $^{87}Sr/^{86}Sr$ suggests that these rocks were hydrothermally altered and subsequently recrystallized within a conductive boundary layer. The vertical distribution of hornfelsed material in the central part of the field area can therefore be explained by substantial fluctuation of depth of a magmatic heat source over relatively short timescales (100s of meters within 10,000 years) and/or subsidence of xenoliths in the melt lens (e.g., Coogan et al., 2003; Gillis, 2008; France et al., 2009). In either case, the occurrence of hornfels within different levels of the upper plutonic section indicates two points. First, the location of the AMC was not fixed and vertical migration over relatively short timescales is indicated (Figure 2.11). This is supported by the presence of highly evolved Fe-Ti-oxide gabbro, tonalitic veins, and basaltic dikes in the lower half of the field area suggesting a melt reservoir

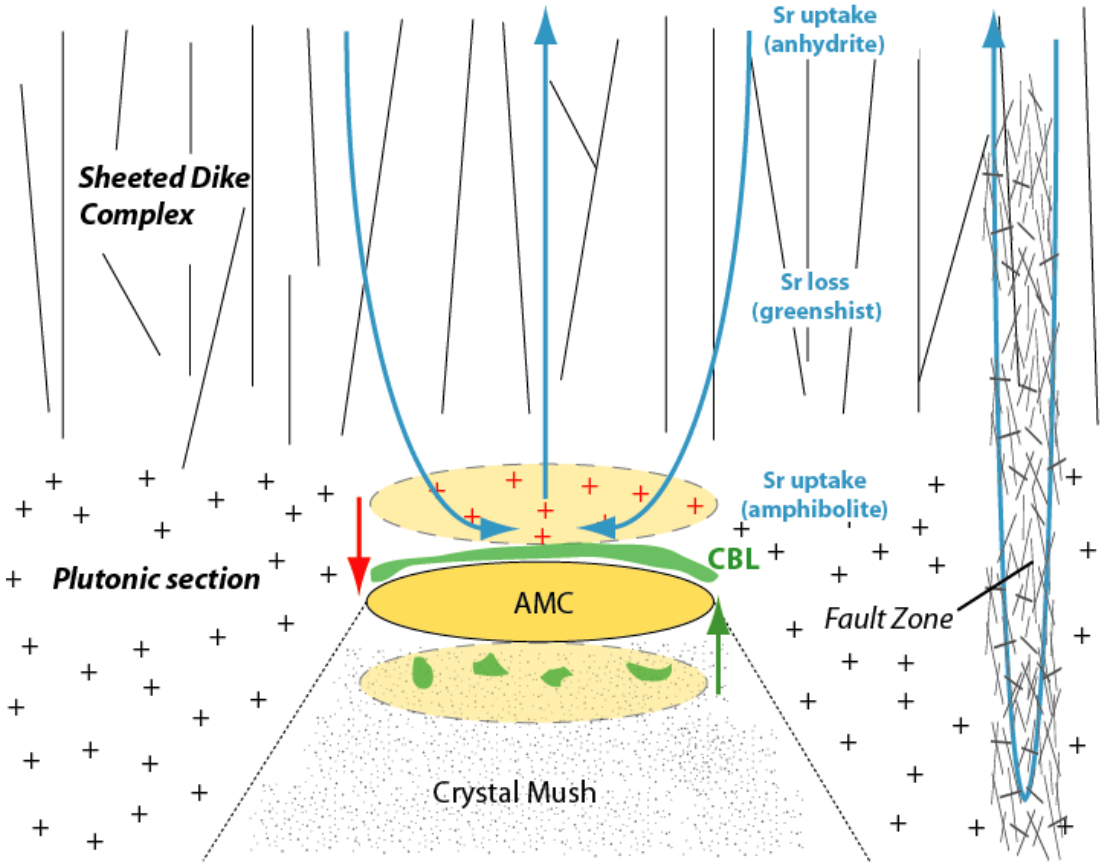

Figure 2.11: Conceptual model of hydrothermal circulation at fast-spreading ridges. The interplay of heat removal by pervasive hydrothermal circulation (blue arrows) and magma supply leads to vertical migration (red and green arrow) of the AMC. Downward migration causes crystallization of gabbroic rocks at the roof of the AMC and allows for fluid ingress into the plutonic section on-axis. Upward migration of the AMC causes recrystallization of previously altered rocks, stoping and contamination of the AMC. Variable thermal regimes at different depths within the altered crust affect Sr behaviour and the quantification of fluid/rock ratios based on $^{87}Sr/^{86}Sr$ systematics. Fault zones propagate into the plutonic section ~2-3 km from the ridge-axis promoting focuses fluid flow.

promoting magmatic differentiation at these or greater depths. Second, fluid ingress occurred on-axis and hydrothermal fluids penetrated to levels of at least 600 m below the base of the sheeted dike complex in proximity to the ridge axis or previously altered xenoliths subsided to this depth (Figure 2.11).

Both the variability of lateral temperature variations and the observed alteration characteristics with depth suggest a highly dynamic interface (Figure 2.11) of heat exchange that reaches down to at least 600 m below the base of the sheeted dike complex.

Chapter 3

CONCLUSIONS AND FUTURE WORK

3.1 Conclusions

The unique tectonic exposure of the upper oceanic crust at the Hess Deep Rift allows us for the first time to examine the temporal and spatial characteristics of a complete section of upper oceanic crust from a fast-spreading ridge setting. In this study, the metamorphic characteristics of hydrothermally altered rocks from the upper plutonic section were studied.

- Plutonic rocks from the Hess Deep rift show variable hydrous replacement (<5 to >20%) with gabbroic rocks generally more strongly altered than gabbronorites. The secondary assemblages are largely amphibole-dominated with several chlorite-rich assemblages found in the western part of the field area. Hornfels, indicative of reheating of previously hydrothermally altered rocks by a migrating magmatic heat source, were recovered from the central part of the field area.
- $^{87}Sr/^{86}Sr$ of the studied rocks are elevated with respect to fresh rock and are positively correlated to the percentage of hydrous alteration and, to a lesser degree, bulk rock Sr content. Comparable to findings from the sheeted dike complex at the Hess Deep Rift, there is no systematic change of $^{87}Sr/^{86}Sr$ with depth within the upper plutonic section, however, the mean $^{87}Sr/^{86}Sr$ is lower than in the sheeted dike complex.

- The Sr content of the studied plutonic rocks is controlled by the combined effects of magmatic differentiation and post-magmatic hydrothermal mobilization. Alteration assemblages indicative of different temperatures have different effects on the Sr budget of hydrothermally altered rocks: intermediate-temperature (chlorite, actinolite, albitic plagioclase) secondary assemblages lead to Sr loss, high-temperature secondary assemblages (hornblende, anorthitic plagioclase) lead to Sr uptake. The replacement mechanism leading to chemical fluxes between primary and secondary phases and the fluid are dominated by dissolution-precipitation versus diffusion.
- Fluid/rock ratios using two different models were calculated for the plutonic section and are ~1. However, due to the large uncertainty regarding fluid composition entering and exiting the gabbroic section, another model, combining the sheeted dike complex and the gabbroic section to one hydrothermal system, was introduced. Fluid/rock ratios using this approach are ~0.5.
- The use of $^{87}Sr/^{86}Sr$ as a geochemical proxy for water-rock interaction should be confined to rocks with little retrograde metamorphism and compare rocks metamorphosed under similar alteration temperatures.
- The plutonic section in the central part of the study area was penetrated by a hydrothermal system on-axis. The depth of fluid penetration on-axis was controlled by a vertically migrating magma chamber. Shallowing of the AMC locally recrystallized previously altered gabbros and dikes, likely within a conductive boundary layer. This upward migration also led to the assimilation of previously altered plutonic rocks.

Evidence for assimilation is present in the Cl and B enrichment of magmatic amphiboles (Gillis et al., 2003) and in one sample on the basis of $^{87}Sr/^{86}Sr$ (this study).

- Incipient fluid ingress is interpreted to occur at high temperatures (700-800°C) throughout the upper plutonics. While it is not possible to constrain where fluid flow was initiated, thermal models indicate that brittle failure occurs at or very close to the ridge axis (Phipps Morgan and Chen, 1993; Manning et al, 1996).

3.2. Future work

We are just beginning to understand the implications of specific mineral hosts and exchange reactions of Sr on the resultant $^{87}Sr/^{86}Sr$ systematics. In order to better constrain fluid/rock ratios and fluid fluxes, a more quantitative approach needs to be developed with respect to Sr behaviour on a mineral scale. Two problems with respect to technical restrictions make it difficult to link Sr content to $^{87}Sr/^{86}Sr$ in hydrothermal environments.

First, it is crucial to find methods to reliably identify secondary plagioclase with intermediate X_{An} and quantify its modal abundance. This is because plagioclase is the major sink for Sr in igneous rocks from mid-ocean ridges. This would dramatically lower the uncertainty associated with Sr mass balance calculations and give better insight into the amount of fluid derived Sr making it much easier to evaluate the relationship between secondary phases and $^{87}Sr/^{86}Sr$ shift.

Second, we need to find a way to determine the geochemistry of crustal fluids. The greatest uncertainties when calculating fluid/rock ratios are the Sr content and $^{87}Sr/^{86}Sr$ of crustal fluids. This study has used hydrothermal epidote hosted in the plutonic section to

constrain $^{87}Sr/^{86}Sr$ at depth. Even though the timing of epidote precipitation is unclear and may not be representative of axial fluid flow, it would be helpful to constrain $D^{Sr}_{epidote/fluid}$ to understand the relationship between $^{87}Sr/^{86}Sr$ and Sr content at depth. These findings should then be compared to vent fluid data.

Some of the problems associated with the regional interpretation of the $^{87}Sr/^{86}Sr$ data are due to sampling gaps between or within different dive tracks. For a more complete understanding of the temporal and spatial relationships of the upper plutonics, these gaps would need to be filled and a more detailed map showing igneous and metamorphic features would need to be generated and compared to other settings. This is, however, a challenging task, since substantial time and funding would be required to excessively explore and sample submarine tectonic windows like the Hess Deep Rift.

Lastly, it is crucial for the mid-ocean ridge community to develop a comprehensive and accessible database combining the geochemistry, primary and secondary mineralogy of hydrothermally altered rocks, as well as for vent fluid chemistry data. The large-scale exchange of data and comparison of different study sites will improve our understanding of the global implications of hydrothermal systems at mid-ocean ridges.

REFERENCES

Albarède, F., A. Michard, J.F. Minster, and G. Michard. 1981. 87Sr/86Sr ratios in hydrothermal waters and deposits from the East Pacific Rise at 21°N. *Earth and Planetary Science Letters* 55, 229–236.

Albarède, F. 1995. Introduction to geochemical modeling. Cambridge Univ. Press,. Cambridge.

Alt. J.C. 1995. Subseafloor processes in mid-ocean ridge hydrothermal systems. *In* Humphris., S.E. Zierenberg, S.A., Mullineux, L.S., and Thomson, R.E. (eds): Seafloor Hydrothermal Systems: Physical, Chemical, Biological and Geological Interaction, Geophys. Monograph *91*, 85-114

Anders, E., and N. Grevesse. 1989. Abundances of the elements: Meteoritic and solar. *Geochimica et Cosmochimica Acta* 53, 197-214.

Andersen, D.L., D.H. Lindsley, and P.M. Davidson.1993. Quilf: A Pascal program to assess equilibria among Fe-Mg-Mn-Ti oxides, pyroxenes, olivine and quartz, *Computers & Geosciences* 19, 1333–1350.

Babcock, J.M., A.J. Harding, G.M. Kent, and J.A. Orcutt. 1998. An examination of along-axis variation of magma chamber width and crustal structure on the East Pacific Rise between 1330’N and 1220'N. *Journal of geophysical research* 103, 30451–30.

Bach, W., and S.E. Humphris. 1999. Relationship between the Sr and O isotope compositions of hydrothermal fluids and the spreading and magma-supply rates at oceanic spreading centers. *Geology* 27, 1067-1070.

Barker, A.K., L.A. Coogan, K.M. Gillis, and D. Weis. 2008. Strontium isotope constraints on fluid flow in the sheeted dike complex of fast spreading crust: Pervasive fluid flow at Pito Deep. *Geochemistry Geophysics Geosystems* 9, doi: 10.1029/2007GC001901.

Barker, A.K., L.A. Coogan, and K.M. Gillis. 2010a. Insights into the behaviour of sulphur in mid-ocean ridge axial hydrothermal systems from the composition of the sheeted dyke complex at Pito Deep. *Chemical Geology* 275, 105-115.

Barker, A.K., L.A. Coogan, K.M. Gillis, N.W. Hayman, and D. Weis. 2010b. Direct observation of a fossil high-temperature, fault-hosted, hydrothermal upflow zone in crust formed at the East Pacific Rise. *Geology* 38, 379-382.

Bayly, M.B., 1965. The sampling error in modal analysis. *American Mineralogist* 50, 196-211.

Berndt, M.E., W.E. Seyfried Jr., and J.W. Beck. 1988. Hydrothermal alteration processes at mid-ocean ridges: experimental and theoretical constraints from Ca and Sr exchange reactions and Sr isotopic ratios. *Journal of Geophysical Research* 93, 4573-4583.

Bettison, L.A., and P. Schiffman. 1988. Compositional and structural variations of phyllosilicates from the Point Sal ophiolite , California. *American Mineralogist* 73, 62-76.

Bickle, M.J., and D.A.H. Teagle. 1992. Strontium alteration in the Troodos ophiolite: implications for fluid fluxes and geochemical transport in mid-ocean ridge hydrothermal systems. *Earth and Planetary Science Letters* 113, 219-237.

Bischoff, J.L., and R.J. Rosenbauer. 1985. An empirical equation of state for hydrothermal seawater (3.2% NaCl). *American Journal of Science* 285, 725-763.

Bischoff, J.L., and W.E. Seyfried Jr. 1978. Hydrothermal chemistry of seawater from 25C to 350C. *American Journal of Science* 278, 838–860.

Blundy, J.D., and B.J. Wood. 1991. Crystal-chemical controls on the partitioning of Sr and Ba between plagioclase feldspar, silicate melts, and hydrothermal solutions. *Geochimica et Cosmochimica Acta* 55, 193-209.

Cherkaoui, A.S.M., W.S.D. Wilcock, R.A. Dunn, and D.R. Toomey. 2003. A numerical model of hydrothermal cooling and crustal accretion at a fast spreading mid-ocean ridge. *Geochemistry Geophysics Geosystems* 4, doi: 10.1029/2001GC000215.

Coogan, L.A., R.N. Wilson, K.M. Gillis, and C.J. MacLeod. 2001. Near-solidus evolution of oceanic gabbros: insights from amphibole geochemistry. *Geochimica et Cosmochimica Acta* 65, 4339-435.

Coogan, L.A., K.M. Gillis, C.J. MacLeod, G.M. Thompson., and R. Hékinian. 2002a. Petrology and geochemistry of the lower ocean crust formed at the East Pacific Rise and exposed at Hess Deep: A synthesis and new results. *Geochemistry Geophysics Geosystems* 3, doi: 10.1029/2001GC000230.

Coogan, L.A., G.R.T. Jenkin, and R.N. Wilson. 2002b. Constraining the cooling rate of the lower oceanic crust: a new approach applied to the Oman ophiolite. *Earth and Planetary Science Letters* 199, 127-146.

Coogan, L.A., G. Thompson, and C.J. MacLeod. 2002c. A textural and geochemical investigation of high level gabbros from the Oman ophiolite: implications for the role of the axial magma chamber at fast-spreading ridges. *Lithos* 63, 67-82.

Coogan, L.A., N.C. Mitchell, and M.J. O'Hara. 2003. Roof assimilation at fast spreading ridges: An investigation combining geophysical, geochemical, and field evidence. *Journal of Geophysical Research* 108, 1-14.

Coogan, L.A., C.E. Manning, and R.N. Wilson. 2007. Oxygen isotope evidence for short-lived high-temperature fluid flow in the lower oceanic crust at fast-spreading ridges. *Earth and Planetary Science Letters* 260, 524-536.

Coogan, L.A. 2008. Reconciling temperatures of metamorphism, fluid fluxes, and heat transport in the upper crust at intermediate to fast spreading mid-ocean ridges. *Geochemistry Geophysics Geosystems* 9, doi: 10.1029/2007GC001787.

Coogan, L.A., 2007. The lower oceanic crust. *In*: R. Rudnick (Editor), *The Crust. Treatise on Geochemistry*.

Dick, H.J.B. 1989. Abyssal peridotites, very slow spreading ridges and ocean ridge magmatism. Geological Society, London, *Special Publications 42*, 71-105

Detrick R.S., Buhl, P., Vera E., Mutter, J., Orcutt, J., Madsen J., and T. Brochert. 1987. Multichannel seismic imaging of a crustal magma chamber along the East Pacific Rise. *Nature* 326, 35 -41.

Eggins, S.M., J.D. Woodhead, L.P.J. Kinsley, G.E. Mortimer, P. Sylvester, M.T. McCulloch, J.M. Hergt, M.R. Handler. 1997. A simple method for the precise determination of ≥40 trace elements in geological samples by ICPMS using enriched isotope internal standardization. *Chemical Geology* 134, 311-326.

Fisher, A.T. 1998. Permeability within basaltic oceanic crust. *Reviews of Geophysics* 36, 143–182.

France, L., B. Ildefonse, and J. Koepke. 2009. Interactions between magma and hydrothermal system in Oman ophiolite and in IODP Hole 1256D: Fossilization of a dynamic melt lens at fast spreading ridges. *Geochemistry Geophysics Geosystems* 10, doi: 10.1029/2009GC002652.

Francheteau, J., R. Armijo, J.L. Cheminee, R Hekinian, P. Lonsdale, and N. Blum. 1990. 1 Ma East Pacific Rise oceanic crust and uppermost mantle exposed by rifting in Hess Deep (equatorial Pacific Ocean). *Earth and Planetary Science Letters* 101, 281-295.

Früh-Green, G.L., A. Plas, and L.N. Dell'Angelo. 1996. Mineralogic and stable isotope record of polyphase alteration of upper crustal gabbros of the East Pacific Rise (Hess Deep, Site 894). In *Proceedings of the Ocean Drilling Program*, ed. C. Mével, K.M. Gillis, J.F. Allan, and P.S. Meyer, 147:235-254.

Giletti, B., and J. Casserly. 1994. Strontium diffusion kinetics in plagioclase feldspars. *Geochimica et Cosmochimica Acta* 58, 3785-3793.

Gillis, K.M. 1995. Controls on hydrothermal alteration in a section of fast-spreading oceanic crust. *Earth and Planetary Science Letters* 134, 473–489.

Gillis K.M. 2008. The roof of an axial magma chamber: A hornfelsic heat exchanger. *Geology* 36, 299-302.

Gillis, K.M., L.A. Coogan, and M. Chaussidon. 2003. Volatile element (B, Cl, F) behaviour in the roof of an axial magma chamber from the East Pacific Rise☆. *Earth and Planetary Science Letters* 213, 447-462.

Gillis, K.M., L.A. Coogan, and R.B. Pedersen. 2005. Strontium isotope constraints on fluid flow in the upper oceanic crust at the East Pacific Rise. *Earth and Planetary Science Letters* 232, 83-94.

Gillis, K.M., T. Gleeson, K. Muehlenbachs, M.A. Stewart, and J.A. Karson. 2001. Fluid flow patterns in fast spreading East Pacific Rise crust exposed at Hess Deep. *Journal of Geophysical Research* 106, 311–29.

Gillis, K.M., and M.D. Roberts. 1999. Cracking at the magma–hydrothermal transition: evidence from the Troodos Ophiolite, Cyprus. *Earth and Planetary Science Letters* 169, 227-244.

Hanna, H.D. 2004. Geochemical variations in basaltic glasses from an incipient rift and upper level gabbros from Hess Deep, eastern equatorial Pacific. *M.Sc. Dissertation Thesis.*

Hayman, N.W., and J.A. Karson. 2007. Faults and damage zones in fast-spread crust exposed on the north wall of the Hess Deep Rift: Conduits and seals in seafloor hydrothermal systems. *Geochemistry Geophysics Geosystems* 8, DOI: 10.1029/2007GC001623.

Hekinian, R., D. Bideau, J. Francheteau, J.L. Cheminee, R. Armijo, P. Lonsdale, and N. Blum. 1993. Petrology of the East Pacific Rise crust and upper mantle exposed in Hess Deep (eastern equatorial Pacific). *Journal of Geophysical Research* 98, 8069–8094.

Hess J., M.L. Bender, and J.-G. Schilling. 1986. Evolution of the ratio of strontium-87 to strontium-86 in seawater from Cretaceous to Present, *Science* 231, 979–984.

Hirth, G., J. Escartin, and J. Lin. 1998. The rheology of the lower oceanic crust: Implications for lithospheric deformation at mid-ocean ridges, in Faulting and Magmatism at Mid-Ocean Ridges, *Geophysical Monograph Series* 106, ed. W.R. Buck et al., 291-303.

Holland, T.J.B., and J.D. Blundy. 1994. Non-ideal interactions in calcic amphiboles and their bearing on amphibole-plagioclase thermometry. *Contributions to Mineralogy and Petrology* 116, 433-447.

Hooft, E.E.E., R.S. Detrick, and G.M. Kent. 1997. Seismic structure and indicators of magma budget along the Southern East Pacific Rise. *Journal of Geophysical Research* 102, 27319–27.

Hövelmann, J., A. Putnis, T. Geisler, B.C. Schmidt, and U. Golla-Schindler. 2009. The replacement of plagioclase feldspars by albite: observations from hydrothermal experiments. *Contributions to Mineralogy and Petrology* 159, 43-59.

Karson, J.A., E.M. Klein, S.D. Hurst, C.E. Lee, P.A. Rivizzigno, and D. Curewitz. 2002. Structure of uppermost fast-spread oceanic crust exposed at the Hess Deep Rift: Implications for subaxial processes at the East Pacific Rise. *Geochemistry Geophysics Geosystems* 3, doi: 10.1029/2001GC000155.

Kelemen, P.B., K. Koga, and N. Shimizu. 1997. Geochemistry of gabbro sills in the crust-mantle transition zone of the Oman ophiolite : implications for the origin of the oceanic lower crust. *Earth and Planetary Science Letters* 146, 475–488.

Lagache, M., and S.C. Dujon. 1987. Distribution of strontium between plagioclase and 1 molar aqueous chloride solutions at 600 C, 1.5 kbar and 750 C, 2 kbar. *Bulletin de minéralogie* 110, 551-561.

Leake, B., et al. 1997. Nomenclature of amphiboles: Report of the Subcommittee on Amphiboles of the International Mineralogical Association on new minerals and mineral names. *Canadian Mineralogist* 35, 219–246.

Liou, J.G., S. Kuniyoshi and K. Ito. 1974. Experimental studies of the phase relations between greenschist and amphibolite in a basaltic system. *American Journal of Science* 274, 613-632,

Lister, C.R.B. 1980. Heat flow and hydrothermal circulation. *Annual Review of Earth and Planetary Sciences* 8, 95-117.

Lonsdale, P. 1988. Structural Pattern of the Galapagos Microplate and Evolution of the Galapagos Triple Junctions. *Journal of Geophysical Research* 93, 13551-13574.

Lécuyer, C., and G. Gruau. 1996. Oxygen and strontium isotope compositions of Hess Dep gabbros (Holes 894F and 894G): high-temperature interaction of seawater with th oceanic crust layer 3. In *Proceedings of the Ocean Drilling Program*, ed. C. Mével, K.M. Gillis, J.F. Allan, and P.S. Meyer, 147:227-234.

Michael P.J., and J.G. Schilling. 1989. Chlorine in mid-ocean ridge magmas – evidence for assimilation of seawater-influenced components. *Geochimica et Cosmochimica Acta* 53, 3131-3143.

Maclennan, J., T. Hulme, and S.C. Singh. 2005. Cooling of the lower oceanic crust. *Geology* 33, 357-360.

Manning, C.E., and D.K. Bird. 1986. Hydrothermal clinopyroxenes of the Skaergaard intrusion. *Contributions to Mineralogy and Petrology* 92, 437-447.

Manning, C.E., C.J. MacLeod, and P.E. Weston. 2000. Lower-crustal cracking front at fast-spreading ridges: Evidence from the East Pacific Rise and the Oman ophiolite. *Ophiolites and Oceanic Crust: New Insights From Field Studies and the Ocean Drilling Program*, 261–272.

Manning, C.E., P.E. Weston, and K.I. Mahon. 1996. Rapid high-temperature metamorphism of East Pacific Rise gabbros from Hess Deep. *Earth and Planetary Science Letters* 144, 123-132.

Natland, J.H., and H.J.B Dick. 1996. Melt migration through high-level gabbroic cumulates of the East Pacific Rise at Hess Deep: the origin of magma lenses and the deep crustal structure of fast-spreading ridges. In *Proceedings of the Ocean Drilling Program*, ed. C. Mével, K.M. Gillis, J.F. Allan, and P.S. Meyer, 147:21–58.

Natland, J.H., and H.J.B. Dick. 2009. Paired melt lenses at the East Pacific Rise and the pattern of melt flow through the gabbroic layer at a fast-spreading ridge. *Lithos* 112, 73-86.

Nicolas, A., I. Reuber, and K. Benn. 1988. A new magma chamber model based on structural studies in the Oman ophiolite. *Tectonophysics* 151, 87–105.

Palmer, M.R. 1992. Controls over the chloride concentration of submarine hydrothermal vent fluids: evidence from Sr/Ca and87Sr/86Sr ratios. *Earth and Planetary Science Letters* 109, 37-46.

Pedersen, R.B., J. Malpas, and T. Falloon. 1996. Petrology and geochemistry of gabbroic and related rocks from Site 894, Hess Deep. In *Proceedings of the Ocean Drilling Program*, ed. C. Mével, K.M. Gillis, J.F. Allan, and P.S. Meyer, 147:3-19.

Phipps Morgan, J., and Y.J. Chen. 1993. The genesis of the oceanic crust: magma injection, hydrothermal circulation, and crustal flow. *Journal of Geophysical Research* 98, 6283–6297.

Piepgras, D.J., and G.J. Wasserburg. 1985. Strontium and neodymium isotopes in hot springs on the East Pacific Rise and Guaymas Basin. *Earth and Planetary Science Letters* 72, 341-356.

Quick, J.E., and R.P. Denlinger. 1993. Ductile Deformation and the Origin of Layered Gabbro in Ophiolites. *Journal of Geophysical Research* 98, 14015-14027.

Ravizza, G., J. Blusztajn, K.L. Von Damm, a.M. Bray, W. Bach, and S.R. Hart. 2001. Sr isotope variations in vent fluids from 9°46′-9°54′N East Pacific Rise: evidence of a non-zero-Mg fluid component. *Geochimica et Cosmochimica Acta* 65, 729-739.

Regelous, M., Y. Niu, J.I. Wendt, R. Batiza, A. Greig, and K.D. Collerson. 1999. Variations in the geochemistry of magmatism on the East Pacific Rise at 10°30′N since 800 ka. *Earth and Planetary Science Letters* 168, 45-63.

Rona, P.A. 1988 Hydrothermal mineralization at oceanic ridges. *Canadian Mineralogist* 26, 431-465.

Schiffman, P., and G.Ó. Fridleifsson. 1991. The smectite-chlorite transition in drillhole NJ-15, Nesjavellir geothermal field, Iceland: XRD, BSE and electron microprobe investigations. *Journal of Metamorphic Geology* 9, 679-696.

Seewald, J.S., and W.E. Seyfried Jr. 1990. The effect of temperature on metal mobility in subseafloor hydrothermal systems: constraints from basalt alteration experiments. *Earth and Planetary Science Letters* 101, 388-403.

Seyfried Jr., W.E., and D.R. Janecky. 1985. Heavy metal and sulfur transport during subcritical and supercritical hydrothermal alteration of basalt: Influence of fluid pressure and basalt composition and crystallinity. *Geochimica et Cosmochimica Acta* 49, 2545-2560.

Sleep, N.H. 1991. Hydrothermal Circulation, Anhydrite Precipitation, and Thermal Structure at Ridge Axes. *Journal of Geophysical Research* 96, 2375-2387.

Sneeringer, M., S.R. Hart, and N. Shimizu. 1984. Strontium and samarium diffusion in diopside. *Geochimica et Cosmochimica Acta* 48, 1589–1608.

Spear, F.S. 1981. An experimental study of hornblende stability and compositional variability in amphibolite. *American Journal of Science* 281, 697-734.

Stein, CA, and S Stein. 1992. A model for the global variation in oceanic depth and heat flow with lithospheric age. *Nature* 359, 123–129.

Stewart, M.A., E.M. Klein, and J.A. Karson. 2002. Geochemistry of dikes and lavas from the north wall of the Hess Deep Rift: Insights into the four-dimensional character of crustal construction at fast spreading mid-ocean ridges. *Journal of Geophysical Research* 107.

Teagle, D.A.H., M.J. Bickle, and J.C. Alt. 2003. Recharge flux to ocean-ridge black smoker systems: a geochemical estimate from ODP Hole 504B. *Earth and Planetary Science Letters* 210, 81-89.

Toomey, D.R., S.C. Solomon, and G.M. Purdy. 1988. Microearthquakes Beneath Median Valley of Mid-Atlantic Ridge Near 23°N: Tomography and Tectonics. *Journal of Geophysical Research* 93, 9093-9112.

Tunnicliffe, V. 1991. The biology of hydrothermal vents – ecology and evolution. *Oceanography and Marine Biology* 29, 319-407.

Von Damm, K.L. 1990. Seafloor Hydrothermal Activity: Black Smoker Chemistry and Chimneys. *Annual Review of Earth and Planetary Sciences* 18, 173-204.

Von Damm, K.L. 2000. Chemistry of hydrothermal vent fluids from 9°–10°N, East Pacific Rise: "Time zero," the immediate posteruptive period. *Journal of Geophysical Research* 105, 11203-11222.

Wilcock, W.S.D., and J.R. Delaney. 1996. Mid-ocean ridge sulfide deposits: Evidence for heat extraction from magma chambers or cracking fronts? *Earth and Planetary Science Letters* 145, 49-64.

Watson, E.B. and T.H. Green. 1981. Apatite liquid partition-coefficients for the rare-earth elements and strontium. *Earth and Planetary Science Letters* 56, 405-421.

Weis, D. et al. 2006. High-precision isotopic characterization of USGS reference materials by TIMS and MC-ICP-MS. *Geochemistry Geophysics Geosystems* 7, doi: 10.1029/ 2006GC001283.

APPENDIX

APPENDIX A: SUPPLEMENTARY INFORMATION

Appendix A.1: Igneous and metamorphic petrology

The following descriptions of mineral textures are provided to supplement the petrographic descriptions outlined in Chapter 2, Section 2.3.1:

In most plutonic rocks, plagioclase is the dominant phase making up 35-55% of the modal abundance. In only two samples the abundance of plagioclase was lower than 30%. Plagioclase commonly forms euhedral to subhedral, tabular or lath-like crystals and ranges in grain-size from 0.5 to >5mm. It shows both simple and polysynthetic twinning. In the gabbros, plagioclase is randomly oriented and commonly equigranular or subophitic to clinopyroxene. Myrmekitic intergrowths fill interstices between plagioclase and clinopyroxene crystals in the more evolved gabbros. In gabbronorites, the grain sizes of plagioclase differ more strongly within a sample. In these assemblages it can occur as fine-grained chadacrysts incorporated in orthopyroxene or as medium- to coarse-grained laths in the groundmass, similar to its appearance in the gabbroic rocks. In a few gabbronoritic samples plagioclase is locally concentrated, in which cases the laths display sub- or even euhedral.

Clinopyroxene occurs as anhedral, elongated or isometric grains and is often characterized by its mottled surface caused by sets of minute exsolution lamellae and/or incipient alteration. Clearly visible exsolution blebs of orthopyroxene are rare but

present. Grain sizes of clinopyroxene within a sample are generally more uniform than for plagioclase and typically range from 2 to 6 mm. Smaller, rounded grains can be found in gabbronorites as chadacrysts in orthopyroxene. Simple twinning is a common feature in these minerals.

Orthopyroxene usually is distinct from clinopyroxene by its larger grain size and a clearer appearance with little or no exsolution patterns. Optically continuous, anhedral orthopyroxene patches grow to a size of typically 8-15 mm but may occasionally have grain sizes of up to >20 mm in diameter. Texturally, these grains are poikilitic or ophitic. The modal abundance ranges from ≤5% to ~20%, but due to the limited scale in thin sections and the random distribution of large orthopyroxene patches might not always be representative for the whole rock.

Fe-Ti oxides are a minor (<5%) component in most samples but can make up >10% of the primary mineral assemblage in Fe-Ti oxide gabbros. They are medium- to coarse-grained with rounded grain boundaries and skeletal or isometric grain shapes. In reflected light, these oxides show exsolution of ilmenite and magnetite.

In several gabbroic samples, primary hornblende forms euhedral to subhedral brown-beige pleochroic grains with clearly visible cleavage. These grains can be up to a size of 3 mm wide and occur as separate grains in the groundmass or rim the outer margins of larger clinopyroxene grains. The abundance of this type of primary hornblende is commonly ~5% and is found in the Fe-Ti-oxide gabbros and rocks containing tonalitic veins. The abundance and grain-size of the primary crystals is elevated at the margins of tonalitic veins. In more evolved samples, small (20-50 µm) blebs of hornblende were

found in clinopyroxene grains and, based on trace element chemistry, were previously interpreted to be of magmatic origin (Coogan et al., 2001).

In at least two samples (2218-1440, 2218-1337) primary hornblende occurs as patches of fine-grained, granoblastic clusters and up to 3 mm, optically continuous grains. In these samples, primary amphibole makes up >40% of the igneous assemblage. The texture of these samples combined with the mineral chemistry of these amphiboles (e.g., Nb>1) lead to the conclusion that these rocks are hornblende hornfels (as opposed to pyroxene hornfels; see below) in which primary amphibole was at least partly recrystallized.

Accessory phases that crystallized from a melt and are commonly present in the gabbroic rocks include apatite and zircon. While zircon occurs in <5% of the samples, colorless apatite needles associated with myrmekitic interstices and embedded in plagioclase are a common feature in the more evolved gabbros. Light-brown to yellow, euhedral titanite grains were found in two samples but due to the high water/rock ratio in these samples, inferred from the presence of hydrothermal epidote, are likely to have precipitated from a fluid.

Tonalitic veins cut some of the gabbroic rocks in the central part of the escarpment and are largely composed of quartz-plagioclase assemblages with anhedral and isometric grain shapes and medium- to coarse-grained textures. Euhedral primary hornblende, that commonly occur in the margins of the tonalitic veins, and relatively long (>2 mm) apatite needles are minor and accessory phases associated with these veins, respectively. The

smallest of these intrusive veins have a width of 3-4 mm, but can reach up to a width of several centimetres.

Figure A.1: Photomicrographs showing different rock types and alteration characteristics (images a-j), as well as BSE and CL images (images k and l) showing secondary plagioclase in plutonic rocks from Hess Deep. a) ~1-mm-wide hydrothermal vein containing quartz and amphibole±chlorite cutting varitextured gabbro (2212-1319). The alteration halo is ≤1 mm . b) Almost complete replacement of orthopyroxene by low Ca-amphibole±talc and magnetite in gabbronorite (2212-1338). c) Ca-amphibole and chlorite replacing clinopyroxene and myrmekitic area, and filling microfractures in gabbronorite (2212-1338). d) Relatively fresh gabbronorite (2213-1125) with characteristic (sub-) ophitic texture of plagioclase in orthopyroxene. e) Microgabbro (2213-1226) with intersertal texture and alteration patches containing Ca-amphibole and/or chlorite. f) Fe-Ti hornblende gabbro(2218-1539) cut by 2-mm-wide vein containing myrmekitic assemblages. Small patches of clinopyroxene are still recognizable in primary amphiboles, indicating late-stage magmatic reactions. Primary amphibole is partly replaced by hydrothermal amphibole. g) Hornblende hornfels (2218-1440) with fine-grained recrystallized primary hornblende and relict coarser-grained orthopyroxene. Plagioclase shows corroded grain boundaries and contains abundant inclusions of primary hornblende. h) Fe-Ti hornblende gabbro (3370-1408) with coarse-grained primary hornblende and elongated to needle-shaped Fe-Ti oxide grains. i) Pyroxene hornfels cut by a ~1-mm-wide vein containing brown hornblende. The vein is interpreted to represent a hydrothermal vein that was metamorphosed during recrystallization of the pyroxene hornfels. j) Quartz-epidote-chlorite assemblage (3374-1057) produced during focused fluid flow in a brecciated fault zone. k) Backscattered electron image of secondary albitic plagioclase (dark patches) in a varitextured chlorite-rich gabbro (2212-1500). l) Cathodoluminescence image showing secondary anorthitic plagioclase (green shades) replacing primary plagioclase (blue) in a hornblende hornfels (2218-1440). Additional and changed abbreviations: Qtz=quartz; Myr=myrmekite; Hbl=primary hornblende; Amp=secondary Ca-amphibole; Ept=epidote.

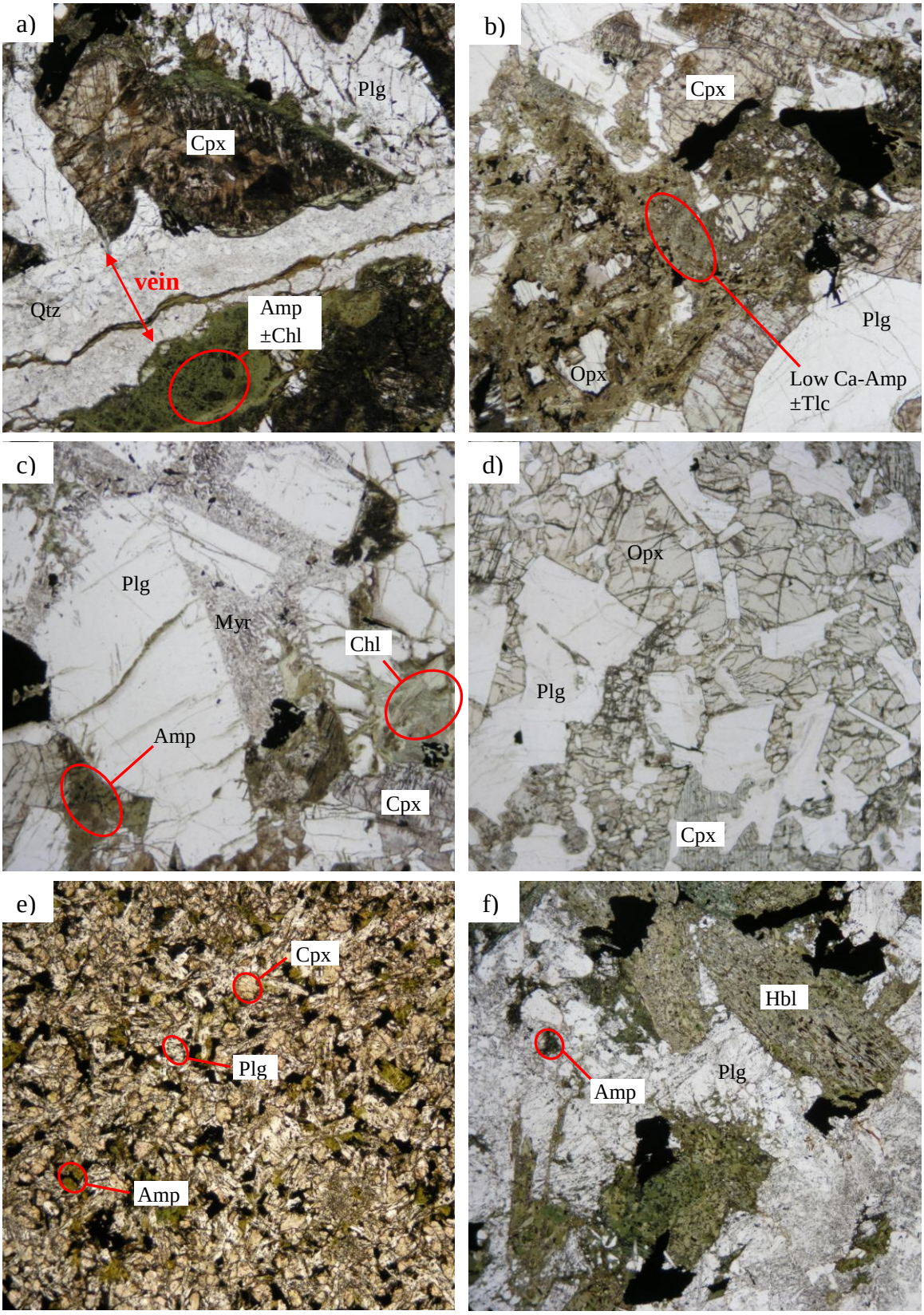
a)
Plg
Cpx
vein
Qtz
Amp
±Chl
b)
Cpx
Plg
Opx
Low Ca-Amp
±Tlc
c)
Plg
Myr
Chl
Amp
Cpx
d)
Opx
Plg
Cpx
e)
Cpx
Plg
Amp
f)
Hbl
Plg
Amp

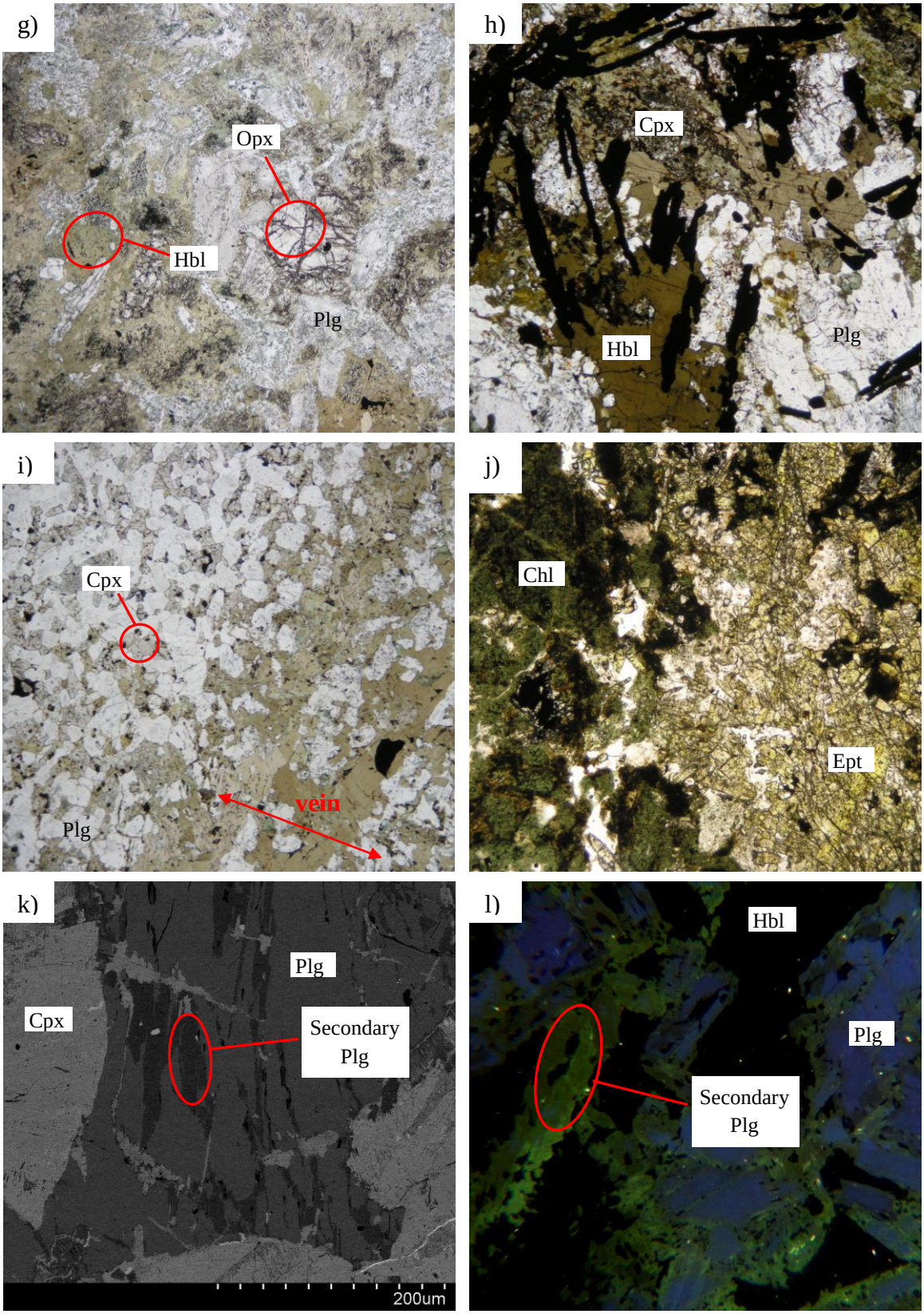
g)
Opx
Hbl
Plg
h)
Cpx
Hbl
Plg
i)
Cpx
vein
Plg
j)
Chl
Ept
k)
Plg
Cpx
Secondary
Plg
200um
l)
Hbl
Plg
Secondary
Plg

Appendix A.2: Bulk Rock Chemistry

The following additional information is provided to supplement the description of bulk rock compositions given in Chapter 2, Section 2.3.2:

A.2.1: Trace element magmatic trends

The observed differentiation trends inferred from major element chemistry are also recorded in the trace element chemistry. Chondrite-normalized REE and Sr patterns show a relatively wide range in differentiation stages ranging from cumulates with pronounced positive Sr and Eu anomalies to highly evolved rocks with strong negative Sr and Eu anomalies (Figure A.2). This pattern suggests that the formation of plagioclase cumulates occurred early on in the most primitive rocks and Sr and Eu contents decreased with more evolved rocks as these species became depleted in the melt. Other REE are well-correlated indicating a genetic relationship as these elements are considered immobile. Fine-grained basaltic dikes hosted in the plutonic section are found at the evolved spectrum of this range. Some Fe-Ti oxide hornblende gabbros are more evolved (e.g., $Eu/Eu^* < 0.8$) than the basaltic dikes ($Eu/Eu^* = 0.8$-0.9) suggesting that they have reacted with substantial amounts of interstitial melt (Coogan et al., 2002a) or represent a frozen melt lens (Natland and Dick, 1996).

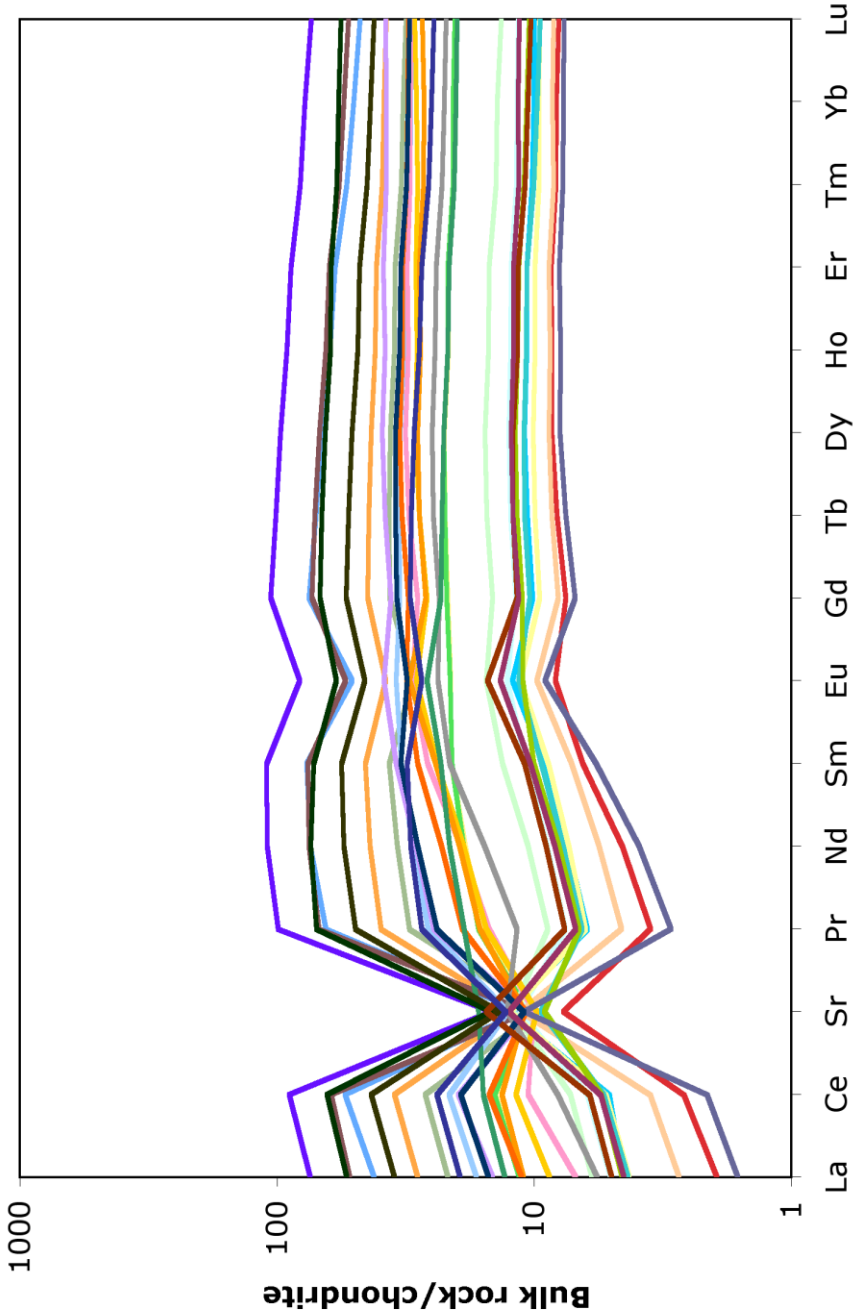

Figure A.2: Chondrite-normalized REE and Sr contents of plutonic rocks from the Hess Deep Rift.

A.2.2: Models for hydrothermal redistribution of Sr based on bulk rock chemistry

In order to determine the poorly known behaviour of Sr in hydrothermal systems, the deviation of bulk rock Sr from a magmatic trend can be used. To evaluate the Sr-redistribution this trend must involve elements that (i) have a well-constrained behaviour in magmatic systems and (ii) are immobile in post-magmatic hydrothermal systems. A problem that needs to be considered when modeling magmatic trends for plutonic rocks is the uncertainty related to the trapped melt fraction (TMF) affecting fractional crystallization models. To assess the TMF and the average mineral abundances for gabbros and gabbronorites, a fractional crystallization trend was first generated for Cr versus Y (Figure A.3a), which have contrasting compatibilities with respect to the phases crystallizing in the plutonic rocks. The magmatic trend fitting the data best was modeled with the following average modal abundances (in fractions):

1) Gabbro: clinopyroxene=0.45, plagioclase=0.25, TMF=0.3

2) Gabbronorite: clinopyroxene=0.35, orthopyroxene=0.05, plagioclase=0.4, TMF=0.2

If these modal abundances roughly represent the different plutonic rocks studied, the hydrothermal redistribution of Sr can be evaluated by the deviation of the geochemical data from a predicted magmatic trend for Sr/Cr versus Y (Figure A.3b) (partition coefficients are from Coogan, 1998 and compiled data from http://earthref.org/). This relationship suggests that Sr is neither strongly depleted nor enriched in gabbronorites, but becomes enriched in more evolved samples. This trend roughly coincides with the

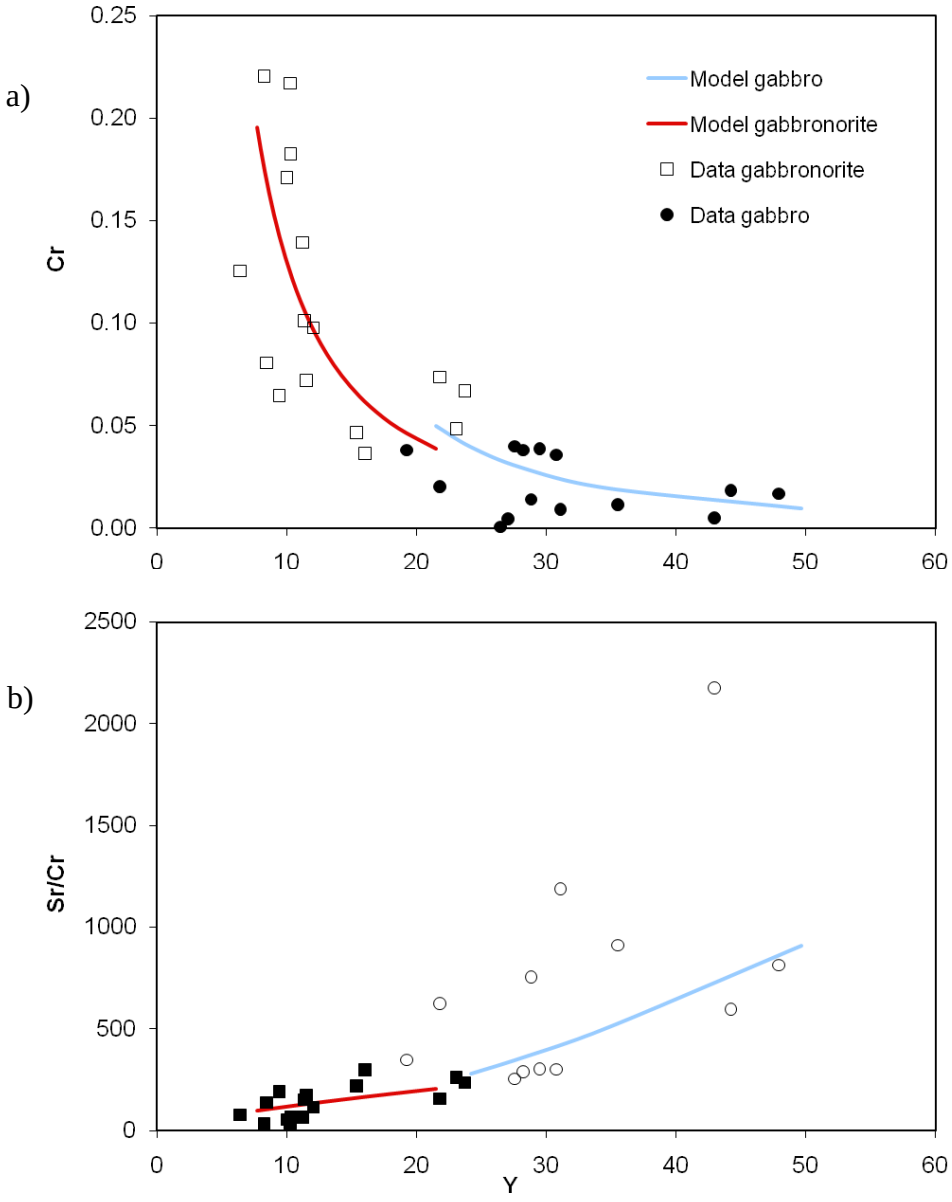

Figure A.3: Magmatic fractionation models for chondrite-normalized bulk rock a) Cr vs. Y and b) Sr/Cr vs. Y in cumulates, plotted against gabbros and gabbronorites from the Hess Deep Rift. Average modal abundances were derived by fitting the two trends in a) to the data of the according plutonic rocks. The deviation of Sr/Cr from the magmatic trend is interpreted to indicate the hydrothermal redistribution of bulk rock Sr.
The models were calculated assuming fractional crystallization. Partition coefficients are from Coogan (1998) and compiled data from http://earthref.org/), chondrite values are from Anders and Grevesse (1989), parental melt compositions are from Regelous (1999).

findings from mineral chemistry but, due to uncertainties regarding partition coefficients and TMF should be treated with caution.

A.2.3: Trace element mobility

Alkali metals like Li, K, Rb and Cs are known to be highly mobile during high-temperature alteration (e.g., Alt, 1995) and hence should be leached from the rocks. Indeed, almost all the studied samples show strong depletion in these elements independent of their magmatic evolution. Five samples however have significantly elevated contents in these elements. Interestingly, all these samples originate from a very restricted area within the location where Fe-Ti-oxide gabbros are cut by tonalitic veins. Irregular, dark cracks that reach a width of up to 3 mm stood out petrographically in some of these samples. Microprobe data suggests that these features are filled by clay minerals which would explain the high content in alkalis. Based on the size and irregularity of these cracks, these features are interpreted to represent overprints of later low-temperature alteration associated with the tectonic opening of the rift valley.

The behaviour of base metals is generally assumed to be strongly dependent on temperature and pH (e.g., Seewald and Seyfried, 1990). There is no correlation of either Cu or Zn content with depth or with each other. However, Cu content decreases with increasing hydrous alteration suggesting post-magmatic mobilization of this phase. Comparing Cu and Zn content to a range of magmatic values shows that Cu is variably depleted in the analyzed rocks whereas Zn may be depleted or enriched. Rocks with Cu content lower than 10 ppm are represented by samples that either contain tonalite, are

low-level dikes or were sampled in cataclastic zones. More representatively altered samples of the suite lie between 10 and 80 ppm. These findings are in contrast with observations from the sheeted dike complex at the Hess Deep Rift where Cu is depleted in >40% and Zn is depleted in >30% of the studied samples with higher percentages of depletion at the base of the sheeted dike complex (Gillis et al., 2001).

Appendix A.3: Mineral chemistry

Mineral data for samples from the northern escarpment of the Hess Deep Rift collected for this study and existing data from Gillis (unpublished, 2001, 2005) were combined.

Plagioclase

Primary plagioclase in the gabbroic rocks show a wide span of An%, ranging from An_{68} to An_{21} where plagioclase in gabbronorites show high anorthite contents and plagioclase from tonalitic veins are at the lower end. Disregarding the late-stage tonalitic veins, the An% of plagioclase in the main portion of the rocks is clustered between An_{42-68}. Plagioclase in one sample (2218-1440) has noticeably higher anorthite contents in excess of 80% and was interpreted to be of hydrothermal origin (see Section 2.3.3.) Anorthite contents of primary plagioclase can vary up to >10% within a sample and even within a grain suggesting extensive zoning in some of the grains. During hydrothermal alteration primary plagioclase in these rocks is most commonly replaced by recrystallized secondary plagioclase. This alteration phase is most reliably characterized by the

depletion of trace elements such as Fe an Mg compared to primary plagioclase. In general, it also shows more extreme An-contents ($An_{<5}$-$An_{>90}$) but the fact that intermediate (primary) compositions are observed does not allow conclusive interpretation based on major elements. However, plagioclase with An_{0-25} and $An_{>80}$ can be assumed to be hydrothermal.

Whole rock Mg# and averaged primary anorthite content of plagioclase are strongly positively correlated, showing a differentiation trend from gabbronorites to gabbros to Fe-Ti-oxide gabbros and hornblende gabbros

Clinopyroxene

The Mg# of clinopyroxene ranges from 0.28-0.85 with the more primitive values found in samples where orthopyroxene is present (0.6-0.8). Values greater than 0.85 are observed in one micrograbbro and low-level dikes that might not have undergone substantial magmatic differentiation yet. The wollastonite content (Ca/(Ca+Fe+Mg) ranges from Wo_{35-48} where grains with $Wo_{>45}$ and low minor element contents (e.g., TiO_2 <0.3 wt%) are considered hydrothermal (Manning and Bird, 1986).

Orthopyroxene

The presence of orthopyroxene in the mineral assemblage generally represents primitive end of the magmatic spectrum. The variability of Mg# is smaller than that in clinopyroxene ranging from 0.48 to 0.76. Systematically low Mg# are observed in hornfelsic rocks that have undergone anhydrous recrystallization and gabbronorites

adjacent to dike intrusions. Thus, enhanced post-magmatic reheating seems to affect the major element chemistry of orthopyroxenes in gabbronorites from Hess Deep. Ignoring these specific samples, in typical Hess Deep gabbronorites have a more limited range of Mg# (0.65-0.76).

Amphibole

Due to the presence of primary and secondary amphibole, with the latter having formed under a variety of hydrothermal conditions and replacing different primary phases, the compositional range of this phase in Hess Deep plutonics is very diverse. The amount of Fe^{2+} and Fe^{3+} in amphiboles was calculated as described in Schumacher (1997, Appendix 2) following the 15eNK calculation.

Primary amphiboles and secondary amphiboles show a good correlation of Al^{IV} and $(Na+K)_A$. Generally there is a good correlation between Ti and Al^{IV} or $(Na+K)_A$, with some grains being low in TiO_2. The contents of TiO_2 in the amphiboles can be as high as 4 wt% but is mostly clustered between 0 and 2 wt%. Based on the classification by Leake et al. (1997) calcic amphiboles are mostly represented by magnesio-hornblende and actinolite with a minor abundance of ferro-hornblende and ferro-actinolite (Figure A.4). Only very few grains contain higher amounts of tetrahedral aluminum and fall in the tschermakitic field of this amphibole classification.

The distinction of primary and secondary amphibole based on Cl and F contents proved to be problematic for samples from Hess Deep since at fast spreading ridge the assimilation by stoping, seawater-contaminated dikes into the AMC may lead to Cl-rich

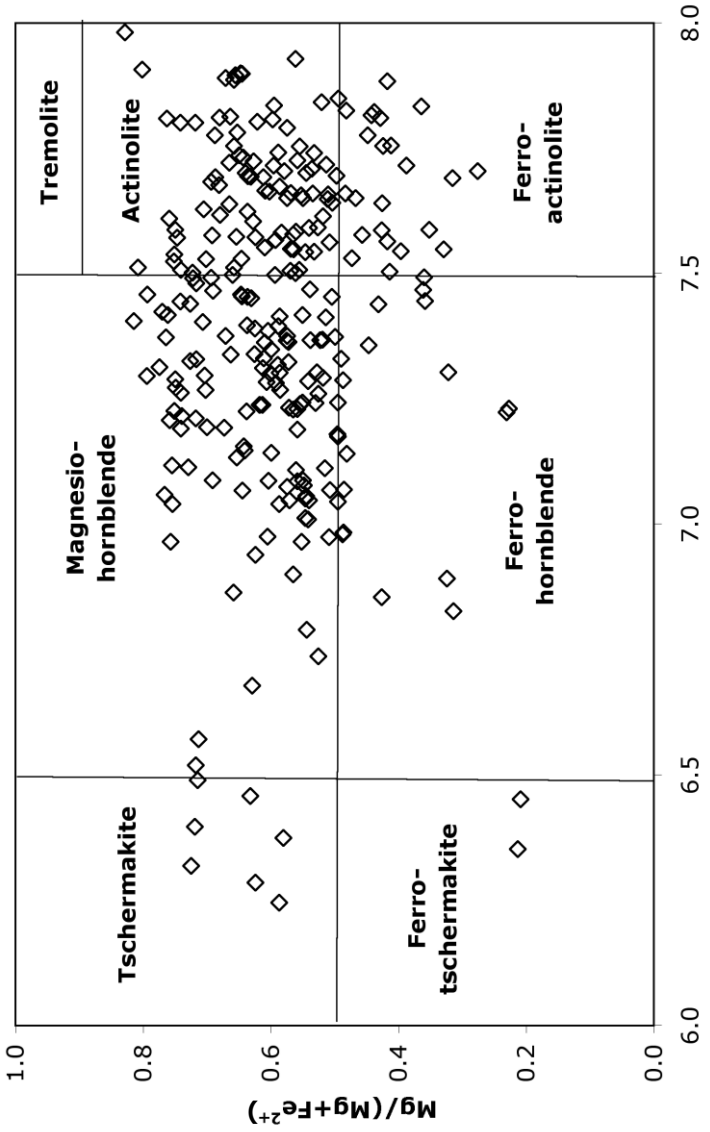

Figure A.4: Classification of hydrothermal and magmatic amphiboles from plutonic rocks exposed at Hess Deep (after Leake et al., 1997). Data comes from this study and Gillis (unpublished, 2001, 2005).

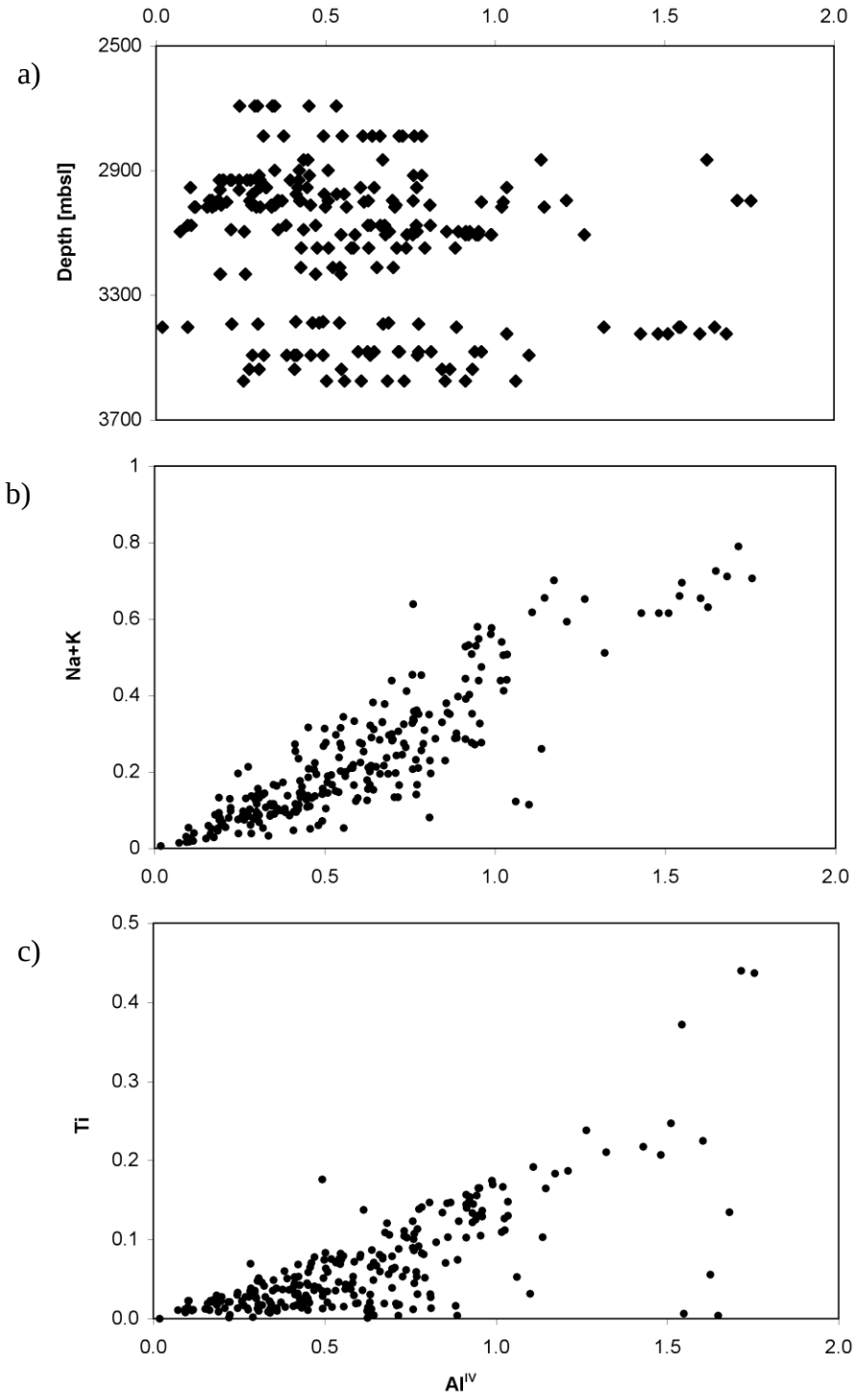

Figure A.5: Al^{IV} in hydrothermal amphibole versus a) depth below sea level, b) Na+K, and c) Ti. Increasing Al^{IV} contents with alkalis and Ti indicate increasing temperatures of formation (e.g., Spear, 1981). The lack of correlation of Al^{IV} depth suggests that hydrothermal temperatures do not increase systematically in this dimension.

primary amphiboles (Gillis et al., 2003). REE contents from gabbroic rocks at Hess Deep indicate that the transition from the crystallization out of a magma to post-magmatic hydrothermal precipitation is continuous (Gillis, 1996). In general, however, it was found that magmatic amphiboles have Nb or Nb/La > 1 (this study, Gillis et al., 2003).

In hydrothermal amphiboles, alkalis on the A-site, TiO_2, and Al^{IV} are strongly positively correlated and suggest increasing alteration temperatures with increasing contents of these species (Spear, 1981) (Figure A.5). Al^{IV} and Cl show a weak positive correlation suggesting that phase separation due to increasing temperatures affects the formation of this phase. There is a wide range from Mg-rich to Fe-rich amphiboles with more Mg-rich amphiboles being slightly more common. The incorporation of neither of these species seems to be temperature-sensitive, however, since no correlation to Al^{IV} is observable. Furthermore, none of the described compounds in amphibole is dependent on depth (Figure A.5) suggesting that neither temperature nor fluid chemistry varies systematically in this dimension.

Chlorite and Chlorite-Smectite

Pure chlorite can be distinguished from mixed-layer chlorite-smectite by its crystallographic properties with Si <6.25 apfu (based on 28 oxygens), lower Ca and higher Al (Bettison and Schiffman, 1988; Schiffmann and Fridleiffson, 1991). Based on these criteria, discrete chlorite represents the main portion of this mineral group in the Hess Deep gabbros. Depending on the nature of interlayering, mixed-layer chlorite-smectite assemblages show a much wider range in composition falling between pure

chlorite and essentially pure saponite. Both chlorite and chlorite-smectite show highly variable Al contents.

APPENDIX B: PETROGRAPHY

Appendix B.1: Sample descriptions

54 thin sections were studied and described qualitatively using a Nikon Eclipse E400 Pol microscope. These observations are documented in the following format:

Sample number

- Rock type*, predominant texture; average grain size**
- Degree of alteration*** *(% if point counted)*; replacive phases *(sorted by abundance)*
- Additional comments

* In some samples orthopyroxene was not directly identified but the characteristic secondary assemblage suggests its presence in the igneous assemblage. In this case, the rock type is referred to as gabbro(-norite).

** fine-grained: <1 mm; medium-grained; 1-5 mm; coarse-grained: >5 mm *(the indicated grain sizes are estimated average grain-sizes. Individual grains may be coarser or finer)*

** low: <10%; medium: 10-20%; high: >20% *(if not point counted, estimates were made by comparing to secondary assemblages with known mineral modes)*

2212-1319

- Gabbro(-norite), equigranular to subophitic, medium-grained
- Medium alteration (14%); amphibole, chlorite, magnetite
- Primary quartz present; contains apatite; clinopyroxene shows plastic deformation (undulose extinction); 1 mm wide hydrothermal vein containing quartz (first generation) and amphibole±chlorite (second generation) cuts sample; Orthopyroxene completely replaced, if present.

2212-1338

- Gabbronorite, intergranular to subophitic, medium- to coarse-grained
- Medium alteration (17%); chlorite, low Ca-amphibole±talc, Ca-amphibole, magnetite, quartz
- Myrmekitic intergrowths; apatite present; replacement patchs of orthopyroxene partly oxidized (red colour); blebby quartz grains part of pyroxene-replacement

2212-1352

- Gabbro, equigranular, medium-grained
- High alteration (30%); chlorite, Ca-amphibole, magnetite
- Apatite present; abundant myrmekitic patches

2212-1358

- Gabbro, equigranular to subophitic, medium-grained

- Medium alteration; chlorite, Ca-amphibole, magnetite
- Contains primary quartz; apatite present

2212-1400

- Gabbro, equigranular to subophitic, medium-grained
- High alteration (21%); chlorite, Ca-amphibole, magnetite
- More abundant apatite than in other samples; myrmekitic intergrowths; plagioclase shows corroded grain boundaries

2212-1409

- Gabbro, equigranular to ophitic, fine- to medium-grained
- Medium alteration (16%); Ca-amphibole, chlorite, magnetite
- Contains primary quartz; contains apatite; ~1 mm wide quartz-vein cuts sample; clinopyroxene locally almost completely replaced; characteristic criss-cross pattern of green amphibole in alteration patches

2212-1416

- Gabbro, equigranular, medium-grained
- Medium alteration; Ca-amphibole, chlorite, magnetite
- Myrmekitic intergrowths; apatite present;

2212-1428

- Gabbro, intergranular to subophitic, fine- to medium-grained
- High alteration; amphibole, chlorite, magnetite
- Contains primary quartz; contains apatite; clinopyroxene very mottled

2212-1500

- Gabbro, equigranular to ophitic, fine- to medium-grained
- High alteration; Ca-amphibole, chlorite, magnetite
- Abundant myrmekitic intergrowths; contains apatite; plagioclase displays partly corroded grain boundaries and commonly cut by microfractures

2213-1053

- Fe-Ti-oxide gabbronorite, equigranular to poikilitic, fine- to medium-grained
- Low alteration (3%); low Ca-amphibole, Ca-amphibole, magnetite
- Anhedral grain shapes with round grain boundaries; mineral alignment; interstices filled with Fe-Ti-oxides; primary hornblende present as blebs in clinopyroxene and discrete grains; reddish alteration mineral fills microcracks and locally alters clinopyroxene

2213-1110

- Gabbronorite, equigranular to poikilitc, medium-grained
- Low alteration; low Ca-amphibole±talc, Ca-amphibole

- Plagioclase chadacrysts in orthopyroxene commonly rounded; green amphibole rimming pyroxene is only hydrous alteration.

2213-1125

- Gabbronorite, intergranular to poikilitic, medium-grained
- Low alteration (5%); Ca-amphibole, low Ca-amphibole±talc
- Prominent exsolution lamellae in clinopyroxene

2213-1206

- Gabbronorite, intergranular to poikilitic, medium-grained
- Medium alteration; Ca-amphibole, low Ca-amphibole±talc
- Orthopyroxene locally rounded

2213-1226

- Microgabbro, intergranular, fine-grained
- High alteration; chlorite, Ca-amphibole
- ~50 µm wide amphibole-vein cutting sample

2213-1333

- Gabbronorite, intergranular to ophitic, medium- to coarse-grained
- Medium alteration; Ca-amphibole, low Ca-amphibole±talc, magnetite

- Grain-size variability stronger than in other samples, contains primary quartz, primary amphibole present associated with clinopyroxene

2213-1351

- Pyroxene hornfels, recrystallized, fine-grained
- Anhydrous
- Narrow (~20 µm) Fe-Ti-oxide-veins and two wider veins (~500 µm) containing clinopyroxene cutting sample

2213-1408

- Microgabbro, intergranular, fine-grained
- High alteration; Ca-amphibole, magnetite
- Clinopyroxene almost entirely replaced whereas plagioclase appears fresh

2213-1439

- Microgabbro, intergranular, fine-grained
- High alteration; chlorite, Ca-amphibole, magnetite
- Elongate plagioclase and/or clinopyroxene grains locally radially oriented and may be associated with finer fragments of clinoyroxene

2213-1504

- Dolerite, intersertal, fine-grained

- Medium alteration; chlorite, Ca-amphibole
- Only very fine plagioclase laths as primary phase recognizable (if not albitized); several parallel amphibole±quartz-veins (~100 µm) cut sample; rare plagioclase phenocrysts embedded in groundmass

2218-1048

- Gabbronorite, equigranular, medium- to coarse-grained
- Low alteration (2%); Ca-amphibole
- Freshest observed sample

2218-1057

- Gabbronorite, equigranular to poikilitic, medium- to coarse-grained
- Low alteration (5%); low Ca-amphibole±talc, chlorite
- Plagioclase oriented; fine oxide blebs occur in interstices; unusually thick exsolution lamellae and blebs in clinopyroxene

2218-1132

- Gabbro(-norite), intergranular to poikilitic, fine- to medium-grained
- Low alteration; unidentified
- Pieces of thin section were broken off and adjacent pyroxene were altered by an assemblage that could not be identified → possibly low-temperature clay minerals

2218-1210

- Gabbro(-norite)/pyroxene hornfels, equigranular/recrystallized, medium- to coarse-grained/fine-grained
- Medium alteration of gabbro(-norite); Ca-amphibole, chlorite
- Thin section with three rock types: 1) Gabbro(-norite), 2) 2-cm-wide tonalite-vein, 3) fine-grained hornfels; the spatial relationships of the different are 1-2-1-3 with a sharp transition between the gabbro(-norite) and the hornfels; euhedral grains of primary amphibole is associated with the tonalite-vein

2218-1221

- Pyroxene hornfels, recrystallized, medium-grained
- Anhydrous/low alteration; unidentified material, talc, chlorite
- Contains olivine; unidentified alteration assemblages occur as reddish-brown as veins and patches and are likely formed during retrograde low-temperature alteration

2218-1229

- Pyroxene hornfels, recrystallized, medium-grained
- Anhydrous/low alteration; unidentified material
- Similar texture as 2218-1221, but less retrograde alteration

2218-1337

- Hornblende gabbro (hornblende hornfels), intergranular, medium-grained

- Medium alteration (16%); Ca-amphibole, talc, magnetite
- Primary quartz present; apatite present; primary amphibole present as optically continuous medium-sized grains or fine-grained, recrystallized blebs in clinopyroxene; plagioclase display corroded grain boundaries and contains abundant inclusions

2218-1404

- Dolerite, intersertal, fine-grained
- High alteration (55%); Ca-amphibole, chlorite, magnetite
- Only very fine plagioclase laths as primary phase recognizable (if not albitized)

2218-1415

- Dolerite, intersertal, fine-grained
- High alteration; chlorite, Ca-amphibole, magnetite
- Plagioclase turbid with clear inclusions (comparable to 2213-1226); cut by ~1 mm wide quartz-vein and smaller amphibole-veins

2218-1440

- Hornblende gabbronorite (hornblende hornfels), intergranular to ophitic, medium-grained
- Low alteration (8%); low Ca-amphibole±talc, Ca-amphibole, magnetite

- Primary amphibole present as optically continuous medium-sized grains or fine-grained, recrystallized blebs; relicts of clinopyroxene locally visible but make up <10% of assemblage; where relict clinopyroxene is visible, clusters of fine-grained opaques are characteristic; plagioclase displays strongly corroded grain boundaries and contains abundant inclusions.

2218-1514

- Hornblende gabbro, equigranular to ophitic, fine- to medium-grained
- High alteration; Ca-amphibole, talc, magnetite
- Primary amphibole present as optically continuous medium-sized grains or fine-grained, recrystallized blebs in clinopyroxene

2218-1539

- Hornblende gabbro, intergranular to subophitic, medium-grained
- Medium alteration; Ca-amphibole, talc, magnetite
- Primary amphibole present as optically continuous medium-sized grains`; cut by 2 mm wide vein containing quartz and myrmekitic intergrowths, primary quartz also abundant in groundmass

3369-1042

- Fe-Ti-oxide hornblende gabbro, equigranular to subophitic, fine- to medium-grained
- Medium alteration (10%); Ca-amphibole, talc, magnetite

- Cut by tonalite-vein; Primary hornblende present as blebs in clinopyroxene and discrete grains

3369-1110

- Gabbronorite, equigranular to subophitic, medium-grained
- Medium alteration; Ca-amphibole, Low Ca-amphibole±talc

3369-1129

- Gabbronorite, equigranular to subophitic, medium-grained
- Medium alteration (11%); unidentified, Ca-amphibole, Low Ca-amphibole±talc
- Grain-size and texture more variable than in other samples; orthopyroxene occurs in clusters of fine- to medium grained equant grains, untypical of its appearance in other gabbronorites, reddish-brown veins cutting pyroxenes and plagioclase represent most of the alteration assemblage.

3369-1156

- Gabbronorite, intergranular, medium- to coarse-grained
- Low alteration; Ca-amphibole, Low Ca-amphibole±talc

3369-1221

- Gabbronorite/pyroxene hornfels, intergranular/recrystallized, medium-grained/fine-grained

- Medium alteration/anhydrous; Ca-amphibole, Low Ca-amphibole±talc
- Two domains: 1) medium-grained gabbronorites 2) fine grained- hornfels; the transition between the two domains is relatively sharp (< 10 mm)

3369-1250

- Fe-Ti oxide gabbronorite, intergranular to subophitic, medium- to coarse-grained
- Medium alteration (14%); Ca-amphibole, Low Ca-amphibole±talc, magnetite
- Orthopyroxene replaced by grass-green, fibrous amphibole; Fe-Ti-oxides are commonly euhedral

3369-1321

- Gabbronorite, equigranular to subophitic, medium-grained
- Medium alteration (10%); Ca-amphibole, Low Ca-amphibole±talc, magnetite

3369-1329

- Quartz-Epidote assemblage; equigranular, fine- to medium-grained
- Likely precipitated from a hydrothermal fluid
- Strongly mottled quartz grains; clusters of fine-grained epidote

3369-1349

- Gabbronorite, equigranular to subophitic, medium- to coarse-grained
- Medium alteration; Ca-amphibole, Low Ca-amphibole±talc, magnetite

- Plagioclase locally clustered with rounded or sutured grain boundaries; plagioclase shows larger grain sizes in these areas

3369-1355

- Olivine gabbronorite, (sub-)ophitic, medium- to coarse-grained
- Medium alteration (11%); Ca-amphibole, Low Ca-amphibole±talc, magnetite
- Plagioclase shows variable grain-sizes from fine- to coarse grained; clino- and orthopyroxene commonly coarse-grained and intergrown

3369-1418

- Fe-Ti-oxide hornblende gabbro, equigranular, medium-grained
- Medium alteration; unidentified
- Cut by tonalite-vein; dark reddish-brown alteration patches replacing clinopyroxene (clay?); contains discrete grains of primary hornblende

3369-1422

- Fe-Ti-oxide hornblende gabbro, equigranular, medium-grained
- Medium alteration; unidentified
- Cut by tonalite-vein; primary hornblende present as blebs in clinopyroxene and discrete grains; clear orange-brown alteration material fills microfractures and alteration patches

3369-1431

- Hornblende gabbro, equigranular, medium-grained
- Medium alteration; unidentified, Ca-amphibole
- Primary hornblende present as blebs in clinopyroxene and discrete grains

3370-1118

- Gabbronorite/pyroxene hornfels, equigranular/recrystallized, medium- and fine-grained
- Low alteration/anhydrous; low Ca-amphibole±talc, Ca-amphibole
- Two domains: medium-grained gabbronorite and fine-grained hornfelsic area; transition between two domains is more gradual than in other samples showing this sort of boundary; primary hornblende present as blebs in clinopyroxene and discrete grains

3370-1205

- Pyroxene hornfels, recrystallized, medium-grained
- Mostly anhydrous; veins/patches of fine-grained orange material
- Cut by vein (~ 2.5 mm) of anhedral brown hornblende that locally encloses small patches of fibrous amphibole; alteration material likely retrograde metamorphism

3370-1311

- Pyroxene hornfels, recrystallized, fine-grained

- Anhydrous
- ~30 µm wide amphibole vein cutting sample; alteration area around this vein <1 mm; high percentage of isometric oxide-grains (~10-20%)

3370-1328

- Pyroxene hornfels, recrystallized, fine- and medium-grained
- Mostly anhydrous; orange and red material filling cracks in medium-grained domain
- Two domains: fine-grained hornfelsic area and medium-grained hornfelsic area; transition between two domains is very sharp (~1 mm); hydrous alteration phases occur >2 cm away from transition zone in medium-grained domain; alteration material likely retrograde metamorphism

3370-1408

- Fe-Ti-oxide hornblende gabbro, intergranular, medium- to coarse-grained
- Medium alteration; Ca-amphibole, chlorite, unidentified
- Primary quartz present; primary hornblende present as blebs in clinopyroxene and discrete grains, reddish inclusions visible; Corroded grain boundaries; Fe-Ti-oxides are needle-shaped

3370-1418

- Fe-Ti-oxide gabbro, intergranular to subophitic, medium-grained
- Medium alteration; Ca-amphibole±talc, magnetite

- Highly corroded grain boundaries with interfingering texture; cut by vein (up to 1.5 mm wide) containing fine-grained brown hornblende and/or clinopyroxene of recrystallized texture

3370-1447

- Fe-Ti-oxide microgabbro, intergranular, fine- to medium-grained
- High alteration; Ca-amphibole, chlorite, magnetite
- Cut by vein containing chlorite+amphibole+quartz; Fe-Ti-ocides needle-shaped and clustered

3374-1012

- Gabbronorite, intergranular to subophitic, medium-grained
- High alteration; low Ca-amphibole±talc, Ca-amphibole, magnetite
- Cut by hydrothermal amphibole-vein (~150 μm); Orthopyroxene entirely replaced by fibrous, green to brown amphibole; primary hornblende present and commonly occurs at the edges and corners of clinopyroxene grains

3374-1031

- Gabbronorite, intergranular to subophitic, medium-grained
- Medium alteration (14%); low Ca-amphibole±talc, Ca-amphibole, magnetite
- Orthopyroxene replaced by fibrous, green to amphibole

3374-1049

- Cataclastite/Fe-Ti-oxide gabbro(-norite), intergranular/cataclastic, medium- to coarse-grained
- Medium alteration in gabbro(-norite) area; Ca-amphibole, chlorite
- Two domains: 1) medium- to coarse grained area with abundant (80%) and oriented plagioclase laths 2) mechanically deformed and highly altered cataclastic area with relict, mottled plagioclase and clinopyroxene; alteration minerals in this area are amphibole+ chlorite+accessory apatite and titanite

3374-1057

- Cataclastite; equigranular, fine- to medium-grained
- Likely precipitated from a hydrothermal fluid
- Relict plagioclase grains recognizeable; subhedral to euhedral brown hornblende present; chlorite present

Appendix B.2: Modal Analysis[8]

The abundance of igneous and metamorphic minerals in 24 samples was quantified by manual point counting using a Prior automatic point counter (Model G) with 5x and 40x magnification. Secondary plagioclase and clinopyroxene were not included in the mineral modes since the distinction between igneous and metamorphic phases with a petrographic microscope is not straightforward. Some samples contain secondary assemblages that could not be identified and are indicated as such. Where applicable, ~1000 counts were made per thin section, following a grid of near-square cells. In samples cut by tonalite-veins, only the modes of the wall rock were point counted. In these samples, and broken thin sections of smaller size, fewer counts may have been made, lowering the representivity of the point counting results.

[8] Abbreviations:
G=gabbro, GN=gabbronorite, Ox-=Fe-Ti-oxide, Hbl-=hornblende, T=tonalite, BD=basaltic dike, HF=Hornfels, Cat.=Cataclastite

Appendix B.2.1: Modal abundances of primary and secondary mineral

Sample #	**2212-1319**	**2212-1338**	**2212-1352**	**2212-1400**	**2212-1409**	**2212-1500**	**2213-1053**	**2213-1125**
Rock type	**G**	**GN**	**G**	**G**	**G**	**G**	**Ox-GN**	**GN**
Primary								
Plagioclase	50	50	41	44	38	34	47	56
Clinopyroxene	25	22	30	24	37	25	32	35
Orthopyroxene		3.2					9.5	3.3
Fe-Ti-oxide	6.9	3.9	2.9	3.9	5.5	9.1	8.8	0.6
Primary hornblende			0.3		0.2	1.1		0.2
Myrmekitic zones		4.7	7.0	6.4		7.8		
Quartz	2.1				3.5			
Apatite	0.2		0.7	0.5	0.2	1.1		
Secondary								
Green amphibole	14	2.5	4.9	5.7	10	7.3	1.9	4.9
Low-Ca amphibole		7.5						0.2
Chlorite	1.8	6.8	13	15	5.4	3.5		
Talc							0.8	
Unidentified secondary			0.1			12.0		
Hydrous alteration %	15	17	18	21	15	23	2.7	5.07

Appendix B.2.1: Modal abundances of primary and secondary minerals [%]

Sample #	**2218-1048**	**2218-1057**	**2218-1210***	**2218-1337**	**2218-1404**	**2218-1440**	**3369-1042***	**3369-1129**
Rock type	**GN**	**GN**	**G**	**Hbl-HF**	**D**	**Hbl-HF**	**Ox-G**	**GN**
Primary								
Plagioclase	36	56	36	45	34	26	53	34
Clinopyroxene	50	29	26	10		2	19	40
Orthopyroxene	12	9.3				8.6		10.8
Fe-Ti-oxide		0.8	4.5	4.1	11	2.1	6.1	4.6
Primary hornblende			11.1	22.7		53.9	12.0	
Myrmekitic zones								
Quartz				2.4				
Apatite				0.3				
Secondary								
Green amphibole	2.2	2.0	14	16	55	1.1	3.9	0.3
Low-Ca amphibole		2.4				0.8		3.3
Chlorite			4.6					
Talc		0.3	0.2			5.8		
Unidentified secondary			3.8				6.1	7.8
Hydrous alteration %	2.2	4.6	23	16	55	7.6	10	11

*Less than 600 counts were made due to thin section size and/or tonalite veins

Appendix B.2.1: Modal abundances of primary and secondary minerals [%]

Sample #	**3369-1250**	**3369-1321**	**3369-1349**	**3369-1355**	**3370-1418**	**3374-1031**	**3369-1355**	**3374-1031**
Rock type	**Ox-G**	**GN**	**GN**	**GN**	**Hbl-Ox-G**	**GN**	**GN**	**GN**
Primary								
Plagioclase	42	52	65	47	43	44	47	44
Clinopyroxene	27	31	19	38	14	34	38	34
Orthopyroxene	1.8	6.2	0.3	3.7		3.9	3.7	3.9
Fe-Ti-oxide	12	1.0	1.1	0.7	10	2.8	0.7	2.8
Primary hornblende	2.6				11.5	0.2		0.2
Myrmekitic zones								
Quartz								
Apatite					0.8			
Secondary								
Green amphibole	13.7	9.5	9.2	3.7	21	10	3.7	10
Low-Ca amphibole		0.6	0.6	3.4		1.2	3.4	1.2
Chlorite			0.5					
Talc								
Unidentified secondary			4.3	2.3		2.9	2.3	2.9
Hydrous alteration %	14	10	14	9.45	21	14	9.45	14

APPENDIX C: BULK ROCK TRACE ELEMENT DATA AND $^{87}SR/^{86}SR$ COMPOSITIONS[9]

Appendix C.1: Trace element compositions

Thirty-one gabbroic rocks representative of rock types, regional distributions and alteration characteristics were selected for trace element analysis. Oxidized edges were removed and macroscopic alteration haloes were avoided. Bulk rock trace elements were analyzed using a Thermo X Series II inductively coupled plasma mass spectrometry (ICP-MS) at the University of Victoria following the modified procedure of Eggins et al. (1997). For this, 100 mg of powder was digested in HF-HNO_3 and 8N HNO_3, and subsequently diluted by a factor of 1:1000 in a 2% HNO_3 solution. Rock standards BIR-1, W2-A, BHVO-2 were analyzed for calibration at the beginning and end of the analyses. Accuracy of the bulk rock analyses were determined by the reproducibility of reported standard values and the comparison of a duplicate analysis. A total of five blanks were analyzed during the analytical session. Data reduction was carried out manually (Microsoft Excel) using In as an internal standard. The comparison of measured bulk rock trace element contents to data from Natland and Dick (1996) shows that Zr values from this study are systematically, and in some samples, significantly lower. This is interpreted to be a result of incomplete zircon dissolution during rock powder digestion.

[9] Appendix C.3 is attached electronically

Appendix C.1.1: Data accuracy

1. Standards BIR-1, W2-A, BHVO-2 were analyzed at the beginning and end of the analyses and were compared to the according reported values (GeoRem) after drift-correction. The error was calculated as follows:

Accuracy % error = ((|Measured average – Reported value|)/(Reported value)*100

2. One duplicate (sample 2212-1338) was analyzed and trace element contents were compared after drift-correction. The % difference was calculated as follows:

% difference = ((|sample – duplicate|)/(average))*100

3. The detection limits of ICP-MS analyses were calculated as three times the standard deviation of blanks.

Appendix C.1.1: Reproducibility of standards compared to reported values

Element [ppm]	BIR-1 measured	BIR-1 measured	Average	BIR-1 reported	Accuracy % error
Li	3.5	3.5	3.5	3.2	10.5
Sc	45	44	44	43	3.1
Ti	5834	5990	5912	5600	5.6
V	326	326	326	319	2.2
Cr	401	394	398	391	1.7
Co	55	54	54	52	4.4
Ni	174	171	172	166	3.9
Cu	122	120	121	119	1.5
Zn	72	71	71	72	0.8
Rb	0.20	0.21	0.21	0.20	2.9
Sr	110	109	110	109	0.8
Y	16	16	16	16	2.3
Zr	15	15	15	14	5.1
Nb	0.55	0.55	0.55	0.55	0.1
Cs	0.01	0.01	0.01	0.01	15.9
Ba	6.81	6.72	6.76	7.14	5.3
La	0.62	0.62	0.62	0.62	1.1
Ce	1.96	1.94	1.95	1.92	1.4
Pr	0.38	0.38	0.38	0.37	3.0
Nd	2.44	2.42	2.43	2.38	2.2
Sm	1.11	1.10	1.11	1.12	1.3
Eu	0.53	0.53	0.53	0.53	0.3
Gd	1.82	1.81	1.81	1.87	3.1
Tb	0.36	0.36	0.36	0.36	0.5
Dy	2.58	2.55	2.57	2.51	2.3
Ho	0.57	0.57	0.57	0.56	1.9
Er	1.71	1.70	1.70	1.66	2.6
Tm	0.25	0.25	0.25	0.25	1.1
Yb	1.67	1.64	1.65	1.65	0.2
Lu	0.25	0.25	0.25	0.25	0.6
Hf	0.59	0.59	0.59	0.58	0.7
Ta	0.04	0.04	0.04	0.04	15.1
Pb	2.90	2.87	2.89	3.10	6.8
Th	0.03	0.03	0.03	0.03	3.9
U	0.01	0.01	0.01	0.01	9.9

Appendix C.1.1: Cont'd

Element [ppm]	BVHO-2 measured	BVHO-2 measured	Average	BVHO-2 reported	Accuracy % error
Li	4.8	4.8	4.8	4.8	0.7
Sc	32	31	31	32	2.1
Ti	16187	16500	16343	16300	0.3
V	312	308	310	317	2.1
Cr	284	278	281	280	0.4
Co	45	44	45	45	0.3
Ni	118	116	117	119	1.9
Cu	129	126	128	127	0.5
Zn	105	104	104	103	1.3
Rb	9.51	9.46	9.49	9.11	4.1
Sr	396	395	396	396	0.1
Y	26	26	26	26	1.0
Zr	174	174	174	172	1.0
Nb	18.52	18.31	18.41	18.10	1.7
Cs	0.10	0.10	0.10	0.10	1.3
Ba	131.16	131.28	131.22	131.00	0.2
La	15.42	15.27	15.35	15.20	1.0
Ce	37.80	37.57	37.68	37.50	0.5
Pr	5.32	5.28	5.30	5.35	0.9
Nd	24.46	24.49	24.48	24.50	0.1
Sm	6.04	6.04	6.04	6.07	0.5
Eu	2.05	2.05	2.05	2.07	0.9
Gd	6.22	6.25	6.23	6.24	0.1
Tb	0.93	0.93	0.93	0.92	0.6
Dy	5.25	5.25	5.25	5.31	1.1
Ho	0.97	0.97	0.97	0.98	1.0
Er	2.51	2.50	2.50	2.54	1.4
Tm	0.33	0.33	0.33	0.33	0.0
Yb	1.97	1.97	1.97	2.00	1.4
Lu	0.28	0.28	0.28	0.27	1.1
Hf	4.35	4.37	4.36	4.36	0.1
Ta	1.15	1.16	1.16	1.14	1.5
Pb	1.65	1.64	1.64	1.60	2.6
Th	1.22	1.23	1.23	1.22	0.5
U	0.41	0.41	0.41	0.40	1.9

Appendix C.1.1: Cont'd

Element [ppm]	W2-a measured	W2-a measured	Average	W2-a reported	Accuracy % error
Li	9.5	9.6	9.6	9.3	3.2
Sc	36	35	36	36	0.8
Ti	6386	6489	6438	6355	1.3
V	263	261	262	268	2.3
Cr	87	87	87	93	6.1
Co	45	45	45	45	0.3
Ni	70	70	70	72	2.6
Cu	105	104	104	105	0.8
Zn	79	80	79	77	3.2
Rb	20.91	20.75	20.83	21.00	0.8
Sr	196	195	195	196	0.4
Y	22	22	22	22	1.4
Zr	94	93	93	92	1.5
Nb	7.38	7.32	7.35	7.50	2.0
Cs	0.92	0.93	0.93	0.92	0.6
Ba	172.27	173.21	172.74	172.00	0.4
La	10.75	10.67	10.71	10.80	0.8
Ce	23.35	23.12	23.24	23.40	0.7
Pr	3.01	3.01	3.01	3.00	0.3
Nd	13.10	13.05	13.08	13.00	0.6
Sm	3.28	3.29	3.29	3.30	0.4
Eu	1.11	1.11	1.11	1.08	2.9
Gd	3.74	3.74	3.74	3.66	2.1
Tb	0.61	0.61	0.61	0.62	1.9
Dy	3.84	3.83	3.83	3.79	1.1
Ho	0.78	0.78	0.78	0.79	0.9
Er	2.22	2.22	2.22	2.22	0.1
Tm	0.32	0.32	0.32	0.33	2.4
Yb	2.05	2.04	2.04	2.05	0.3
Lu	0.30	0.31	0.31	0.31	1.3
Hf	2.45	2.46	2.46	2.45	0.3
Ta	0.46	0.46	0.46	0.47	1.8
Pb	7.72	7.77	7.75	7.70	0.6
Th	2.18	2.20	2.19	2.17	0.8
U	0.50	0.50	0.50	0.51	2.1

Appendix C.1.1: Accuracy of duplicate analyses [ppm]

Sample	2212-1338	Duplicate	Average	% difference
Li	1.83	1.84	1.84	0.48
Sc	32	32	32	0.55
Ti	10310	10327	10319	0.17
V	325	325	325	0.14
Cr	234	235	234	0.45
Co	40	40	40	0.38
Ni	87	88	88	0.51
Cu	60	60	60	0.38
Zn	88	88	88	0.39
Rb	0.24	0.24	0.24	0.79
Sr	83	83	83	0.11
Y	31	31	31	0.22
Zr	74	75	74	0.26
Nb	2.41	2.41	2.41	0.11
Cs	0.01	0.01	0.01	3.53
Ba	6.37	6.37	6.37	0.10
La	2.67	2.70	2.69	1.23
Ce	8.66	8.73	8.70	0.76
Pr	1.50	1.52	1.51	1.07
Nd	8.48	8.58	8.53	1.18
Sm	3.10	3.09	3.09	0.21
Eu	1.19	1.19	1.19	0.48
Gd	4.31	4.35	4.33	0.92
Tb	0.80	0.80	0.80	0.42
Dy	5.48	5.51	5.50	0.50
Ho	1.17	1.18	1.18	0.36
Er	3.44	3.46	3.45	0.60
Tm	0.51	0.51	0.51	0.48
Yb	3.29	3.32	3.31	0.78
Lu	0.49	0.50	0.50	1.26
Hf	2.11	2.13	2.12	1.06
Ta	0.16	0.16	0.16	0.47
Pb	0.27	0.27	0.27	0.03
Th	0.10	0.10	0.10	0.04
U	0.28	0.28	0.28	0.89

Appendix C.1.1: Detection limits [ppm] (3x standard deviation of blank analyses)

Sample	Blank 1	Blank 2	Blank 3	Blank 4	Blank 5	Blank 6	Standard deviation	Detection Limit
Li	0.3582	0.3501	0.3418	0.3309	0.3033	0.3745	0.0245	0.0734
Sc	0.0274	0.0336	0.0377	0.0359	0.0511	0.0317	0.0081	0.0244
Ti	1.2997	3.7835	5.5810	1.2487	1.3329	2.5852	1.7550	5.2651
V	0.0570	0.1170	0.1760	0.0848	0.0961	0.0988	0.0400	0.1201
Cr	0.6578	0.6655	0.2032	0.2175	0.2543	0.2232	0.2264	0.6791
Co	0.0049	0.0114	0.0153	0.0086	0.0084	0.0116	0.0035	0.0106
Ni	0.0121	0.0220	0.0276	0.0258	0.0272	0.0320	0.0069	0.0206
Cu	0.1725	0.1963	0.1195	0.0907	0.1291	0.1250	0.0385	0.1154
Zn	1.2056	1.1928	1.0867	0.5460	1.6959	1.0835	0.3674	1.1021
Rb	0.0009	0.0013	0.0028	0.0016	0.0008	0.0032	0.0010	0.0030
Sr	0.0611	0.1447	0.1828	0.1752	0.1626	0.1789	0.0461	0.1383
Y	0.0024	0.0087	0.0251	0.0043	0.0066	0.0107	0.0081	0.0244
Zr	0.0200	0.0283	0.0282	0.0157	0.0214	0.0261	0.0051	0.0152
Nb	0.0007	0.0016	0.0029	0.0008	0.0009	0.0017	0.0008	0.0025
Cs	0.0002	0.0003	0.0006	0.0005	0.0004	0.0005	0.0001	0.0004
Ba	0.1577	0.1284	0.1126	0.1142	0.1083	0.1170	0.0183	0.0548
La	0.0004	0.0009	0.0033	0.0008	0.0011	0.0023	0.0011	0.0033
Ce	0.0044	0.0061	0.0139	0.0021	0.0030	0.0086	0.0044	0.0131
Pr	0.0001	0.0004	0.0016	0.0003	0.0004	0.0009	0.0005	0.0016
Nd	0.0008	0.0023	0.0090	0.0015	0.0025	0.0046	0.0030	0.0089
Sm	0.0002	0.0009	0.0029	0.0005	0.0005	0.0012	0.0010	0.0030
Eu	0.0002	0.0004	0.0010	0.0002	0.0002	0.0003	0.0003	0.0010
Gd	0.0004	0.0012	0.0035	0.0006	0.0011	0.0016	0.0011	0.0033
Tb	0.0001	0.0002	0.0007	0.0001	0.0002	0.0003	0.0002	0.0006
Dy	0.0005	0.0016	0.0042	0.0007	0.0013	0.0019	0.0013	0.0040
Ho	0.0001	0.0003	0.0009	0.0002	0.0003	0.0004	0.0003	0.0008
Er	0.0004	0.0008	0.0028	0.0006	0.0007	0.0011	0.0009	0.0026
Tm	0.0001	0.0002	0.0004	0.0000	0.0001	0.0001	0.0001	0.0004
Yb	0.0003	0.0009	0.0026	0.0004	0.0007	0.0010	0.0008	0.0025
Lu	0.0000	0.0001	0.0003	0.0001	0.0001	0.0001	0.0001	0.0003
Hf	0.0006	0.0008	0.0010	0.0005	0.0007	0.0007	0.0002	0.0005
Ta	0.0002	0.0002	0.0004	0.0003	0.0001	0.0002	0.0001	0.0003
Pb	0.0430	0.0420	0.0391	0.0359	0.0368	0.0396	0.0028	0.0084
Th	0.0001	0.0002	0.0003	0.0003	0.0004	0.0003	0.0001	0.0002
U	0.0002	0.0002	0.0002	0.0002	0.0002	0.0003	0.0000	0.0001

Appendix C.1.1: Comparison of data from this study and Natland and Dick, 1996 [ppm]

Sample #	2218-1404	2218-1404	% difference	3369-1355	3369-1355	% difference
Rock Type	BD	BD		GN	GN	
Data source	N & D, 1996*	this study		N & D, 1996	this study	
V	495	471	5.1	240	230	4.1
Cr	47	46	1.2	372	370	0.3
Ni	44	37	16	118	111	5.8
Cu	54	52	4.0	77	69	11
Zn	84	91	8.5			
Rb	0.40	0.28	35			
Sr	98	93	5.0	75	71	5.6
Y	67	62	7.7	20	17	13
Zr	210	180	15	43	16	91
Nb	5.4	5.2	4.5		0.6	
Ba	18.0	10.5	53.0	7.1	7.1	0.0

Sample #	2218-1048	2218-1048	% difference	3370-1418	3370-1418	% difference
Rock Type	GN	GN		Ox-G	Ox-G	
Data source	N & D, 1996	this study		N & D, 1996	this study	
V	194	208	7.2	525	538	2.3
Cr	554	587	5.7	87	45	64
Ni	122	118	3.3	51	39	27
Cu	95	80	17	10	15	35
Zn	29	43	39			
Sr	61	60	1.9	106	106	0.3
Y	14	13	8.5	61	75	20
Zr	14	13	11	208	18	169
Nb	0.4	0.2	62		6.5	
Ba	2.0	4.3	73	11.9	10.6	12

*Natland and Dick, 1996

Appendix C.1.2: Trace element data[10]

In this chapter, bulk rock trace element contents are presented for thirty-one analyzed samples.

Note: samples with Rb contents >2 ppm were likely contaminated by low-temperature alteration assemblages, probably additionally affecting other species. These samples were not included in $^{87}Sr/^{86}Sr$ relationships in Chapter 2.

[10] Abbreviations:
G=gabbro, GN=gabbronorite, Ox-=Fe-Ti-oxide, Px=Pyroxene, Hbl-=hornblende, T=tonalite, BD=basaltic dike, HF=Hornfels, Cat.=Cataclastite
mbsl = meters below sea level
Alt. assem.=alteration assemblage, C=chlorite-rich, A=amphibole-dominated

Appendix C.1.2: Bulk rock trace element contents [ppm]

Sample	2212-1338	2218-1210	2218-1048	2218-1350	2218-1404
Lithology	GN	G+T	GN	BD	BD
Depth [mbsl]	3017	3392	3387	3540	3492
Alt. assem.	C	C	A		C
Li	1.83	3.96	4.02	1.46	1.57
Sc	32	51	46	35	39
Ti	10310	32771	2646	16540	16868
V	325	950	208	183	471
Cr	234	23	587	0	46
Co	40	53	36	38	40
Ni	87	51	118	3	37
Cu	60	56	80	10	52
Zn	88	249	43	71	91
Rb	0.24	5.61	0.27	0.56	0.28
Sr	83	87	60	114	93
Y	31	96	13	141	62
Zr	74	56	13	48	180
Nb	2.41	9.25	0.21	11.94	5.16
Cs	0.01	0.42	0.01	0.04	0.01
Ba	6.37	13.28	4.28	13.94	10.46
La	2.67	9.93	0.46	17.63	6.71
Ce	8.66	33.29	1.61	54.84	21.44
Pr	1.50	5.97	0.33	9.18	3.64
Nd	8.48	33.96	2.08	49.95	19.88
Sm	3.10	11.32	0.96	16.26	6.69
Eu	1.19	2.87	0.47	4.60	2.12
Gd	4.31	14.93	1.50	21.07	8.84
Tb	0.80	2.54	0.29	3.64	1.58
Dy	5.48	16.48	2.10	23.83	10.59
Ho	1.17	3.40	0.46	4.98	2.26
Er	3.44	9.50	1.37	14.13	6.57
Tm	0.51	1.32	0.20	2.01	0.96
Yb	3.29	8.10	1.31	12.53	6.16
Lu	0.49	1.17	0.20	1.81	0.93
Hf	2.11	2.33	0.45	1.89	4.84
Ta	0.16	0.52	0.02	0.77	0.35
Pb	0.27	0.27	0.16	0.17	0.35
Th	0.10	0.13	0.02	0.57	0.29
U	0.28	0.09	0.02	0.10	0.13

Appendix C.1.2: Cont'd

Sample	2218-1415	3369-1042	3369-1050	3369-1110	3369-1129
Lithology	BD	Ox-Hbl-G+T	GN	GN	GN
Depth [mbsl]	3492	3232	3232	3161	3169
Alt. assem.	C	A	A	A	A
Li	2.77	2.25	4.36	4.77	3.44
Sc	39	40	43	45	49
Ti	18254	16973	3810	5104	3558
V	364	574	216	284	235
Cr	14	101	485	260	159
Co	41	48	31	35	30
Ni	19	85	79	78	66
Cu	12	68	71	54	30
Zn	115	80	55	53	46
Rb	0.71	0.37	0.39	0.42	0.31
Sr	82	75	98	88	94
Y	99	52	16	19	23
Zr	151	61	23	29	25
Nb	8.65	4.13	0.51	0.91	0.53
Cs	0.05	0.01	0.02	0.02	0.01
Ba	8.41	9.96	12.00	6.11	7.02
La	12.35	5.14	1.07	1.20	1.41
Ce	37.80	16.21	3.13	3.80	4.43
Pr	6.38	2.82	0.58	0.70	0.82
Nd	34.23	15.54	3.39	4.07	4.83
Sm	11.20	5.41	1.35	1.59	1.96
Eu	3.04	1.67	0.68	0.72	0.86
Gd	14.52	7.26	2.01	2.34	2.89
Tb	2.57	1.32	0.38	0.45	0.55
Dy	16.83	8.92	2.68	3.08	3.81
Ho	3.52	1.91	0.58	0.67	0.82
Er	9.99	5.55	1.70	1.97	2.39
Tm	1.41	0.81	0.25	0.29	0.35
Yb	8.85	5.21	1.61	1.88	2.23
Lu	1.29	0.78	0.25	0.28	0.33
Hf	4.56	2.14	0.71	0.91	0.84
Ta	0.57	0.28	0.04	0.06	0.04
Pb	0.19	0.31	0.46	0.19	0.19
Th	0.38	0.16	0.04	0.05	0.04
U	0.13	0.04	0.04	0.02	0.01

Appendix C.1.2: Cont'd

Sample	3369-1156	3369-1221a	3369-1221b	3369-1250	3369-1321
Lithology	GN	GN	Px-HF	Ox-GN	GN
Depth [mbsl]	3148	3158	3158	3094	3076
Alt. assem.	A	A		A	A
Li	3.93	2.29	4.22	2.80	3.47
Sc	35	37	47	44	38
Ti	3481	23270	9512	29177	2960
V	207	685	519	617	190
Cr	172	55	81	31	215
Co	35	44	39	57	34
Ni	68	43	38	40	74
Cu	78	91	43	77	47
Zn	53	85	119	91	55
Rb	0.32	1.05	0.31	0.72	0.36
Sr	97	99	78	82	88
Y	15	49	46	55	13
Zr	23	114	60	76	19
Nb	0.49	6.35	1.24	7.43	0.30
Cs	0.02	0.05	0.02	0.07	0.01
Ba	5.25	17.33	9.95	10.17	4.32
La	1.01	3.97	1.64	3.43	0.65
Ce	3.23	13.13	6.48	12.08	2.17
Pr	0.59	2.39	1.39	2.28	0.42
Nd	3.36	13.57	8.80	13.17	2.55
Sm	1.30	4.85	3.84	5.08	1.06
Eu	0.63	1.94	1.68	2.15	0.55
Gd	1.89	6.61	5.65	7.16	1.60
Tb	0.36	1.21	1.10	1.37	0.31
Dy	2.48	8.16	7.77	9.58	2.16
Ho	0.54	1.75	1.69	2.08	0.47
Er	1.59	5.09	4.99	6.16	1.40
Tm	0.24	0.75	0.75	0.93	0.21
Yb	1.54	4.86	4.88	6.06	1.36
Lu	0.23	0.73	0.73	0.93	0.21
Hf	0.72	3.39	1.89	2.83	0.60
Ta	0.04	0.41	0.09	0.51	0.02
Pb	0.22	0.35	0.25	0.37	0.20
Th	0.04	0.14	0.03	0.11	0.02
U	0.02	0.09	0.06	0.07	0.01

Appendix C.1.2: Cont'd

Sample	3369-1329	3369-1349	3369-1355	3369-1418	3369-1422
Lithology	T	GN	GN	Ox-Hbl-G+T	Ox-Hbl-G+T
Depth [mbsl]	3060	3040	3032	3000	3006
Alt. assem.	C	A	A	A	A
Li	3.95	5.34	4.73	12.00	9.09
Sc	3	41	45	57	54
Ti	532	4339	3967	43691	32283
V	9	239	230	865	809
Cr	2	455	370	12	2
Co	1	37	35	58	52
Ni	2	101	111	26	15
Cu	2	58	69	71	51
Zn	6	51	47	158	155
Rb	0.20	0.70	0.59	29.43	17.32
Sr	68	73	71	76	85
Y	238	16	17	42	41
Zr	20	11	16	107	88
Nb	14.61	0.73	0.61	7.58	5.61
Cs	0.01	0.05	0.01	2.49	1.83
Ba	28.13	8.16	7.11	7.60	9.03
La	71.86	1.02	1.07	2.06	2.60
Ce	206.93	3.29	3.36	7.22	8.17
Pr	32.16	0.60	0.62	1.42	1.51
Nd	146.47	3.53	3.66	8.57	8.92
Sm	38.32	1.39	1.48	3.53	3.57
Eu	4.86	0.65	0.62	1.61	1.72
Gd	42.33	2.07	2.21	5.20	5.26
Tb	6.92	0.39	0.42	1.01	1.01
Dy	41.61	2.70	2.91	7.12	6.98
Ho	8.05	0.59	0.63	1.56	1.51
Er	21.39	1.70	1.83	4.61	4.46
Tm	2.86	0.25	0.27	0.70	0.66
Yb	16.44	1.57	1.72	4.61	4.30
Lu	2.06	0.23	0.26	0.72	0.67
Hf	1.38	0.42	0.59	3.23	2.79
Ta	1.44	0.05	0.04	0.53	0.40
Pb	0.16	0.27	0.28	0.46	0.43
Th	5.26	0.03	0.04	0.07	0.08
U	0.84	0.02	0.06	0.06	0.06

Appendix C.1.2: Cont'd

Sample	3369-1431	3370-1118	3370-1205	3370-1328a	3370-1328b
Lithology	Hbl-G	GN/HF	Px-HF	Px-HF (dike)	Px-HF (gabbro)
Depth [mbsl]	3006	3481	3362	3242	3242
Alt. assem.	A	A			
Li	4.34	2.67	3.62	2.61	3.46
Sc	57	40	49	45	27
Ti	22314	2190	8190	15181	8252
V	1114	185	327	489	251
Cr	24	116	172	103	58
Co	74	35	35	47	26
Ni	33	65	69	55	52
Cu	74	26	6	41	8
Zn	174	46	50	76	38
Rb	17.34	0.19	0.39	0.42	0.67
Sr	84	85	99	86	128
Y	49	12	36	50	33
Zr	62	10	40	37	29
Nb	2.25	0.05	0.96	3.42	2.36
Cs	1.32	0.01	0.04	0.04	0.07
Ba	7.72	3.76	5.99	7.04	7.32
La	2.65	0.38	1.34	3.56	3.07
Ce	9.16	1.30	4.96	11.83	9.65
Pr	1.76	0.27	1.08	2.22	1.74
Nd	10.49	1.79	7.12	12.99	9.74
Sm	4.20	0.85	3.16	4.87	3.41
Eu	1.76	0.51	1.33	1.76	1.47
Gd	6.14	1.38	4.64	6.81	4.57
Tb	1.18	0.27	0.89	1.25	0.82
Dy	8.20	1.95	6.12	8.51	5.52
Ho	1.77	0.43	1.32	1.82	1.18
Er	5.20	1.27	3.84	5.27	3.43
Tm	0.77	0.19	0.56	0.77	0.50
Yb	4.99	1.24	3.60	4.96	3.24
Lu	0.76	0.19	0.54	0.75	0.49
Hf	2.16	0.39	1.55	1.54	1.18
Ta	0.16	0.01	0.08	0.23	0.17
Pb	0.30	0.11	0.16	0.08	0.14
Th	0.11	0.01	0.01	0.04	0.05
U	0.10	0.01	0.01	0.04	0.02

Appendix C.1.2: Cont'd

Sample	3370-1408	3370-1418	3374-1012	3374-1031	3374-1049	3374-1057
Lithology	Ox-Hbl-G	Ox-G	GN	GN	Cat.	Cat.
Depth [mbsl]	3106	3096	3034	2997	2913	2899
Alt. assem.	A	A	A	A	C	C
Li	2.48	1.30	2.72	3.24	4.81	10.26
Sc	30	43	39	45	39	23
Ti	20462	18930	6086	7885	12256	10252
V	397	538	239	469	436	280
Cr	8	45	269	191	374	34
Co	30	40	27	50	30	14
Ni	20	39	64	108	77	24
Cu	71	15	81	85	8	10
Zn	57	98	47	95	121	54
Rb	4.51	0.40	0.19	0.33	0.21	0.26
Sr	114	106	120	98	101	226
Y	96	75	18	18	43	74
Zr	19	18	25	27	64	74
Nb	10.34	6.48	1.06	0.65	4.51	7.80
Cs	0.52	0.01	0.00	0.02	0.01	0.00
Ba	20.85	10.61	6.95	10.41	8.42	1.89
La	12.66	8.26	1.18	1.06	4.60	12.25
Ce	39.06	26.30	3.73	3.37	14.67	37.11
Pr	6.49	4.59	0.70	0.64	2.54	5.74
Nd	33.76	25.11	4.11	3.80	13.82	27.62
Sm	10.67	8.28	1.61	1.53	4.60	7.99
Eu	3.31	2.56	0.85	0.76	1.54	2.78
Gd	13.55	10.67	2.32	2.28	6.05	9.93
Tb	2.42	1.90	0.44	0.44	1.08	1.78
Dy	15.93	12.54	2.96	3.02	7.20	11.79
Ho	3.37	2.65	0.63	0.66	1.52	2.53
Er	9.85	7.61	1.85	1.92	4.38	7.44
Tm	1.45	1.10	0.27	0.28	0.63	1.11
Yb	9.28	6.97	1.70	1.85	4.03	7.12
Lu	1.39	1.03	0.25	0.28	0.60	1.06
Hf	1.06	0.86	0.83	0.86	2.02	3.12
Ta	0.71	0.42	0.08	0.05	0.29	0.63
Pb	0.24	0.18	0.21	0.22	0.36	0.36
Th	0.74	0.30	0.03	0.03	0.20	1.25
U	0.20	0.05	0.01	0.02	0.06	0.15

Appendix C.2: $^{87}Sr/^{86}Sr$ compositions

$^{87}Sr/^{86}Sr$ was determined following the approach of Weis et al. (2006). Twenty -nine bulk rock powders, two epidote separates and two plagioclase separates were analyzed in two separate runs. The mineral separates were leached in hot 6N HCl for 30 minutes prior to digestion. For isotopic analysis, Sr was separated using standard cation exchange techniques and then analyzed in a Triton thermal ionization mass spectrometry (TIMS) at the Pacific Centre for Isotopic and Geochemical research, University of British Columbia. Standard SRM987 was used for normalization of the samples. The normalization calculation is as follows:

Normalized value = measured value*(average measured SRM987/reported SRM987)

To determine the accuracy of the measured values, four duplicates were analyzed in the two runs.

Appendix C.2.1: Comparison of duplicate analyses

	$^{87}Sr/^{86}Sr$	2σ
2218-1210	0.702682	0.000008
Duplicate	0.702691	0.000009
3369-1355	0.702535	0.000008
Duplicate	0.702544	0.000008
2218-1440	0.702562	0.000008
Duplicate	0.702552	0.000007
3369-1129	0.702574	0.000007
Duplicate	0.702573	0.000007

Appendix C.2.2: $^{87}Sr/^{86}Sr$ compositions of bulk rock powders and mineral separates

Sample #	$^{87}Sr/^{86}Sr$	Error (+/-2σ)	Rock Type	Depth [mbsl]
2212-1319	0.702551	0.000009	G	2996
2212-1338	0.702586	0.000007	GN	3017
2212-1409	0.702563	0.000007	G	2990
2212-1500	0.702681	0.000008	G	2916
2213-1053	0.702444	0.000008	Ox-GN	3211
2213-1125	0.702445	0.000007	GN	3160
2213-1516[11]	0.703008	0.000009	BD	2595
2218-1048	0.702621	0.000008	GN	3387
2218-1057	0.702519	0.000008	GN	3389
2218-1210[11]	0.702682	0.000008	G+T	3392
2218-1337	0.702575	0.000008	Hbl-HF	3537
2218-1404	0.702827	0.000008	BD	3492
2218-1440	0.702562	0.000008	Hbl-HF	3423
3369-1042	0.702518	0.000009	Ox-Hbl-G + T	3232
3369-1129	0.702574	0.000007	GN	3169
3369-1250	0.702553	0.000007	Ox-G	3094
3369-1321	0.702569	0.000008	GN	3076
3369-1329	0.703798	0.000008	T	3060
3369-1355	0.702535	0.000008	GN	3032
3369-1418[12]	0.702875	0.000009	Ox-Hbl-G + T	3000
3369-1431[11]	0.702524	0.000008	Hbl-G	3006
3370-1118	0.702512	0.000007	GN/HF	3481
3370-1205	0.702730	0.000007	HF	3362
3370-1328 (dolerite)	0.702589	0.000007	HF	3242
3370-1328 (gabbro)	0.702709	0.000008	HF	3242
3370-1408[11]	0.702751	0.000009	Ox-Hbl-G	3106
3370-1418	0.702674	0.000008	Ox-G	3096
3374-1031	0.702624	0.000009	GN	2997
3374-1057	0.703790	0.000009	Cat.	2899
			Mineral	
2214-1127	0.704292	0.000007	Epidote	2150
3369-1129	0.702461	0.000006	Plagioclase	3169
3369-1355	0.702513	0.000007	Plagioclase	3032
3370-1408	0.703732	0.000006	Epidote	3106

[11] Thin section and powder were not from the same rock

[12] High Rb contents suggest contamination by low-temperature assemblages; these samples were not considered in Chapter 2

APPENDIX D: MINERAL CHEMISTRY[13]

Major and minor element compositions of igneous and metamorphic minerals were determined using a Cameca SX-50 scanning electron microprobe at the University of British Columbia. The microprobe was operated at 15 kV accelerating voltage, a 20 nA beam current, and a beam diameter of 5 mm.

Trace element concentrations of igneous and metamorphic minerals were determined using laser ablation (LA ICP-MS) at the University of Victoria. NIST 615, NIST 613 and NIST 611 were used as external standards for calibration and as instrumental drift monitors. The reproducibility of reported values was used to determine the accuracy for each analytical session. ^{42}Ca or ^{43}Ca were used as an internal standards for the analyses. For analytical sessions focusing on Sr in plagioclase, plagioclase standards (An_0, An_{25}, An_{50}, An_{75} and An_{100}) were used for calibration of anorthite content and were run at the beginning and the end of each analytical session.

Appendix D.1: Major and minor element compositions*

Appendix D.2: Trace element compositions*

Appendix D.2.1: Data Accuracy

Appendix D.2.2: Mineral trace element contents

[13] Data is attached electronically (Appendix D1.xls, Appendix D2.xls)